MASTERARBEIT / MASTER'S THESIS

Titel der Masterarbeit / Title of the Master's Thesis

Experimental requirements for particle optomechanics

verfasst von / submitted by

Felix Donnerbauer, BSc

angestrebter akademischer Grad / in partial fulfilment of the requirements for the degree of

Master of Science (MSc)

Wien, 2020 / Vienna 2020

Contents

Acknowledgements

First and foremost, I want to thank my supervisor, Markus Arndt, for taking me in when I was a Bachelor student and for guiding me over the last three years. You gave me the chance to explore what it means to be an experimental physicist, while also helping me grow as a person.

A huge thank you also goes out to Stefan Kuhn for taking me along with him, both during and outside of work, for patiently teaching me the physics behind our experiments and for always being open to any questions I had, even long after he left. You are a true inspiration to me.

On a similar note I want to thank Stephan Troyer. I cannot hope to count the amount of times you selflessly helped me throughout the years. Moreover, thank you for proofreading my thesis and for providing valuable input. I will miss your tireless scurrying through the halls.
I also want to thank Philipp Rieser for many valuable discussions and for being an awesome and fun lab partner. I am glad we got to work together during this last year.

More generally, I want to thank the whole Quantum Nanophysics group, all of you were always open for questions and happy to help. The administrative staff, with Petra leading the way, also deserves a big thank you. Without your work we would not be able to do physics at all.

None of this would have been possible without the endless and unconditional love and support of my family. Thank you to my parents for encouraging my curious nature, for teaching me critical thinking and for making it possible for me to pursue my interests. Thank you also to my brother, Paul, for always having an open ear and for regularly disappearing with me underwater.

Last, but certainly not least, I want to thank my partner, Veronika. Thank you for always having my back and for being there for me when I need you. You kept me sane during the lockdown and helped me focus on this thesis. I love you endlessly.

Abstract

Nanoparticles have found innumerable uses in physics, biology or medicine. As a result, various fabrication methods with precise control over the size and shape of the particles have been developed. One of them is called *Laser printing of nanoparticles* and is based on local melting of a donor material by irradiation with single pulses from a femtosecond laser.

In quantum optics, experiments with optically levitated nanoparticles offer a promising opportunity to test fundamental questions of quantum mechanics on a macroscopic level. Due to the decoupling between the experiment and its environment, these systems are also suitable as precise force and torque sensors. However, the controlled introduction of the nanoparticles into the optical trap represents a considerable experimental hurdle. This work is devoted to the discussion of a novel particle source for levitated optomechanics and gives an overview of the many facets of this rapidly growing field.

In the first part of the thesis the theoretical ground work for optical cooling of nanoparticles is worked out, starting with an introduction to Gaussian beam optics. Then, optical tweezers and feedback cooling are introduced, followed by a more in-depth treatise of optical resonators. This includes techniques for stabilizing the resonator and particle detection methods. In addition, the commonly used mechanisms for loading optical traps are presented.

In the second part, laser printing of nanoparticles is discussed as a potential experimental particle source. First, the working principle of the particle generation process is explained and experimental results of printed particles are presented. Subsequently, interferometric scattering microscopy as an in-situ observation method of the experiment is explored. Finally, an experimental setup is presented that combines the previously discussed techniques with an optical resonator in a vacuum-compatible configuration.

Zusammenfassung

Nanoteilchen haben unzählige Anwendungsmöglichkeiten in Physik, Biologie oder Medizin gefunden. Aufgrund dessen wurden diverse Herstellungsmöglichkeiten mit präziser Kontrolle über Größe und Form der Teilchen entwickelt. Eine davon nennt sich *Laserdrucken von Nanoteilchen* und basiert auf dem lokalen Schmelzen eines Donormaterials durch Bestrahlung mit einzelnen Pulsen eines Femtosekundenlasers.

In der Quantenoptik bieten Experimente mit optisch levitierten Nanoteilchen eine vielversprechende Möglichkeit fundamentale Fragen der Quantenmechanik auf makroskopischer Ebene zu testen. Aufgrund der Entkopplung zwischen Experiment und dessen Umgebung eignen sich diese Systeme außerdem als präzise Kraft- und Drehmomentsensoren. Das kontrollierte Einbringen der Nanoteilchen in die optische Falle stellt jedoch eine erhebliche experimentelle Hürde dar. Diese Arbeit widmet sich der Erörterung einer neuartigen Teilchenquelle für levitierte Optomechanik und gibt einen Überblick über die vielen Facetten dieses schnell wachsenden Feldes.

Im ersten Teil der Arbeit werden die theoretischen Grundlagen für die optische Kühlung von Nanoteilchen ausgearbeitet, beginnend mit einer Einführung in die Gaußsche Strahloptik. Darauf folgend wird die optische Pinzette und das Rückkopplungskühlen vorgestellt, gefolgt von einer eingehenderen Abhandlung von optischen Resonatoren. Dies inkludiert Techniken zur Stabilisierung des Resonators und Methoden zur Detektion von Teilchen. Außerdem werden die allgemein üblichen Mechanismen zur Beladung von optischen Fallen vorgestellt.

Im zweiten Teil wird Laserdrucken von Nanoteilchen als potentielle experimentelle Teilchenquelle erörtert. Zuerst wird das Arbeitsprinzip der Teilchenerzeugung erläutert und experimentelle Ergebnisse gedruckter Teilchen präsentiert. Anschließend wird interferometrische Streumikroskopie zur direkten Observation des Experiments vorgestellt. Abschließend wird ein Versuchsaufbau präsentiert, der die vorgestellten Techniken mit einem optischen Resonator in einer vakuumkompatiblen Konfiguration kombiniert.

1 Introduction

The field of quantum optomechanics describes the interaction between a light field and the motion of a mechanical object. A fundamental phenomenon behind this interaction is radiation pressure. The idea of radiation pressure was first formulated by Johannes Kepler in the 17th century to explain his observation that a comet's tail always points away from the sun [1]. More than 250 years later, in 1873, James Maxwell published a formulation that attributes a momentum to light, which can be transferred to any object via illumination [2]. The experimental validation of his postulation was provided at the start of the 20th century by Pyotr Lebedew [3] and Ernest Nichols and Gordon Hull [4]. Around the same time Max Planck formulated his description of blackbody radiation, including the hypothesis that the energy of an electromagnetic system is quantized, $E = h\nu$ [5]. Albert Einstein extended this idea to explain the photoelectric effect [6], for which he received the Nobel Prize in physics in 1921. In 1909 Einstein reasoned, that as a consequence of light pressure there would have to exist radiation friction [7].

In the early 1970s Arthur Ashkin used the radiation pressure force to optically levitate and control micrometer-sized particles [8, 9]. Levitation of silicon oil drops and silica microspheres in vacuum [10] soon followed. Moreover, a proposal to use the non-conservative nature of the scattering force to cool atoms was published in 1975 [11]. Experimental validation was provided in 1978 [12, 13] and laser cooling has since become an important technique in various different fields of physics [14].

Momentum transfer via radiation pressure alone, however, cannot optically trap a particle, as the net force always points in the direction of beam propagation. Ashkin formulated this fact in an optical Earnshaw theorem [15] in 1983. What enables stable trapping, is the second part of the optical force – a conservative gradient force which always points toward the region of highest intensity. Therefore, one way to achieve a stable trap is to minimize the net radiation pressure force. This can be accomplished by two counterpropagating beams [8], back-reflection of a single beam at a mirror [16, 17], or can even be compensated gravity [9]. The other way is to strengthen the electric field gradient by highly focusing the laser beam until it drowns the scattering force. Again, Arthur Ashkin first demonstrated such a single-beam gradient force trap for dielectric particles [18]. This technique was soon adapted to trap and manipulate viruses [19], bacteria [19, 20], proteins [21] or single cells [22] and has become an important application in biology [23] and is now better known as optical tweezers.

Another break-through technology in the field of optomechanics was the development of optical cavities. As first reported by Charles Fabry and Alfred Pérot in 1899 [24] the optical cavity in its simplest form consists of two opposing mirrors with the ability to trap light between them. Today, optical resonators are an important part of many practical applications, including laser resonators [25], mode cleaning [26] or cavity ring-down spectroscopy [27]. More recently, optical cavities have been implemented as gravitational wave detectors [28–30].

A cavity-based cooling scheme for atoms was first proposed by Helmut Ritsch and his group in 1997 [31] and shortly after extended to molecules by Steven Chu and Vladan Vuletic [32]. When in 2010 three separate groups proposed coupling of optically levitated nanoparticles to optical cavities [33–35] the field of levitated optomechanics really took off [14, 36]. First successful cavity cooling of silica [37] and silicon [38] nanoparticles was reported in 2013, whereas ground state cooling of a levitated nanoparticle via cavity cooling was demonstrated just recently [39].

Optically levitated systems have many unique properties. Due to their decoupling from the environment, they can exhibit incredibly high mechanical quality factors compared to their size. The Q-factor indicates how often a particle can oscillate until half of its energy is dissipated, and is thus a measure for how underdamped the system is [40]. Explored as early as 1976 [10], so far Q-factors for levitated nanoparticles up to 10^8 have been measured [41], but are predicted to be able to reach as high as 10^{12} [33]. Furthermore, levitated nanoparticles can be incredibly precise force [42] or torque sensors [43, 44].

This thesis aims to provide an overview of the many facets of this rapidly growing field. In chapter 2 several different optical cooling schemes are presented, as well as a theoretical treatise of light-matter interaction and cavity optomechanics.

Chapter 3 is dedicated to the exploration of the currently used particle loading mechanisms for levitated optomechanics. Various different techniques are examined for their advantages and drawbacks. Further on, in chapter 4, the potential of a new source based on femtosecond laser-induced transfer (LIT) is investigated.

Interferometric scattering microscopy (iSCAT) is a useful detection tool much used in biology and biophysics over the last two decades. Chapter 5 illustrates the basic idea of this technique and how it allows us to in-situ observe the nanoparticle creation process.

Finally, in chapter 6 we present an experimental setup to test the validity of LIT as a particle source.

2 Optical cooling of nanoparticles

In this chapter, we review the principle of optical trapping of particles. To start off, a general introduction in fundamental Gaussian beam optics is given. Then, we use ray optics and the Rayleigh approximation to elucidate the concept of optical tweezers. Following this, parametric feedback cooling and cold damping of nanoparticles will be discussed. Later on, we establish a fundamental description of cavity optomechanics, including light-matter interaction, Sisyphus cooling, coherent scattering cooling, cavity locking mechanisms and detection methods for particles inside an optical cavity.

2.1 Gaussian beam optics

In order to understand the optomechanical interaction between a laser beam and an arbitrary particle, we first need to establish the properties of the light field. The most commonly used fundamental laser mode is a Gaussian beam (TEM_{00} mode). In principle, it is a cylindrically symmetric wave with a Gaussian intensity distribution. In the following we will work out a brief mathematical derivation based on [45], [46] and [47].

We know that Maxwell's equations are solved by a wave function:

$$\vec{E}(\vec{r}, t) = \vec{E}(\vec{r})e^{-i\omega t} \tag{2.1}$$

with $\vec{r} = \vec{n_x}x + \vec{n_y}y + \vec{n_z}z$, $\vec{E}(\vec{r})$ the purely spatial part of the wave function and ω given by the dispersion relation $c = \frac{\omega}{k}$ where k is the wave vector. Entering this into the wave equation

$$\left(\frac{1}{c^2}\partial_t^2 - \Delta\right)\vec{E}(\vec{r}, t) = \Box\vec{E}(\vec{r}, t) = 0 \tag{2.2}$$

we end up with the Helmholtz equation:

$$\left(\frac{\omega^2}{c^2} + \Delta\right)\vec{E}(\vec{r}) = \left(k^2 + \Delta\right)\vec{E}(\vec{r}) = 0. \tag{2.3}$$

The solutions to the Helmholtz equation are independent for each polarization direction, therefore we will drop the vectorial nature of $\vec{E}$ in the following discussion. We now restrict ourselves to the paraxial wave approximation, were we consider only small corrections to the properties of a plane wave propagating along z:

$$E(\vec{r}) = A(\vec{r})e^{-ikz} \tag{2.4}$$

with $A \, \epsilon \, \mathbb{C}$ a position-dependent amplitude and phase deformation and, within a distance $\Delta z = \lambda$,

$$\frac{\Delta A}{A} \ll 1 \qquad\qquad \text{and} \qquad\qquad \frac{\Delta \frac{\partial A}{\partial z}}{\left| \frac{\partial A}{\partial z} \right|} \ll 1,$$

i.e. the change of amplitude and phase as well as the rate of change is small. We can then write:

$$\Delta A = \frac{\partial A}{\partial z}\Delta z = \frac{\partial A}{\partial z}\lambda = \frac{\partial A}{\partial z}\frac{2\pi}{k} \ll A \qquad\qquad \Rightarrow \qquad \frac{\partial A}{\partial z} \ll k \cdot A$$

$$\frac{\partial}{\partial z}\left(\frac{\partial A}{\partial z}\right) \ll \frac{\partial}{\partial z}\left(k \cdot A\right) = k \cdot \frac{\partial A}{\partial z} \ll k^2 \cdot A \qquad \Rightarrow \qquad \frac{\partial^2 A}{\partial z^2} \ll k^2 \cdot A$$

We insert equation 2.4 into the Helmholtz equation:

$$\Delta \left(A(\vec{r})e^{-ikz} \right) + k^2 A(\vec{r})e^{-ikz} = 0$$

$$\Delta_T A(\vec{r})e^{-ikz} + \partial_z^2 A(\vec{r})e^{-ikz} + k^2 A(\vec{r})e^{-ikz} = 0 \tag{2.5}$$

where we have used $\Delta_T = \partial_x^2 + \partial_y^2$ to separate the transverse from the longitudinal component of the field. Let us take a deeper look at the longitudinal part:

$$\partial_z^2 A(\vec{r})e^{-ikz} = \partial_z \left(\left(\partial_z A(\vec{r})\right)e^{-ikz} - ikA(\vec{r})e^{-ikz} \right)$$

$$= \left(\partial_z^2 A(\vec{r})\right)e^{-ikz} - 2ik\left(\partial_z A(\vec{r})\right)e^{-ikz} - k^2 A(\vec{r})e^{-ikz}$$

$$= \left(\underbrace{\partial_z^2 A(\vec{r})}_{\ll k^2 A(\vec{r})} - 2ik\left(\partial_z A(\vec{r})\right) - k^2 A(\vec{r}) \right)e^{-ikz} \tag{2.6}$$

$$\approx \left(-2ik\partial_z A(\vec{r}) - k^2 A(\vec{r}) \right)e^{-ikz}$$

Now we insert that back into equation 2.5 and end up with the paraxial Helmholtz equation:

$$\Delta_T A(\vec{r}) - 2ik\partial_z A(\vec{r}) = 0. \tag{2.7}$$

One solution to this equation is given by

$$A(\vec{r}) = A_0 \, e^{-ik\rho^2/2q(z)} \, e^{-ip(z)} \tag{2.8}$$

where $\rho^2 = x^2 + y^2$ and $q(z)$ and $p(z)$ are unknown functions. Inserting this Ansatz into the paraxial Helmholtz equation yields

$$\left\{ \left[\frac{k^2}{q(z)} \left(q'(z) - 1 \right) \right] \rho^2 - 2k \left[p'(z) + \frac{i}{q(z)} \right] \right\} A(\vec{r}) = 0. \tag{2.9}$$

The nontrivial solution to this equation is given by two ordinary differential equations

$$\frac{dq}{dz} = q'(z) = 1 \tag{2.10}$$

$$\frac{dp}{dz} = p'(z) = -\frac{i}{q(z)} \tag{2.11}$$

Let us solve equation 2.10 first, as it is decoupled from the other. The solution is trivial, $q(z) = z + \xi$, with some offset ξ. Now, if we look again at equation 2.8 we see that if $q(z)$ were always real, $|\exp[-ik\rho^2/2q(z)]| = 1$ for all ρ. This would mean that the phase would change faster with increasing ρ, while the amplitude stays constant. This clearly does not resemble a beam, therefore $q(z)$ has to be imaginary. A Gaussian beam is now defined as $\xi = -iz_R$ where z_R is called the *Rayleigh length*. Now we look at $z = 0$:

$$A(\rho, z = 0) = A_0 \, e^{-k\rho^2/2z_R} \, e^{-ip(z=0)}. \tag{2.12}$$

Here we can define the *beam waist* w_0

$$w_0^2 = \frac{2z_R}{k} = \frac{\lambda z_R}{\pi} \qquad \text{or} \qquad z_R = \frac{\pi w_0^2}{\lambda}.$$

This means, that the field varies as $\exp(-\rho^2/w_0^2)$ in the XY-plane at $z = 0$. We now also have an explicit form for the Rayleigh length. Furthermore, for arbitrary z

$$\frac{1}{q(z)} = \frac{1}{z + iz_R} = \frac{(z - iz_R)}{(z + iz_R)(z - iz_R)} = \frac{z}{z^2 + z_R^2} - i\frac{z_R}{z^2 + z_R^2} =: \frac{1}{R(z)} + i\frac{\lambda}{\pi w^2(z)} \tag{2.13}$$

where we have defined the wavefront curvature $R(z)$ and the beam width $w(z)$. These can be expressed in terms of z_R:

$$w(z) = w_0 \sqrt{1 + \left(\frac{z}{z_R}\right)^2} \qquad \text{and} \qquad R(z) = \left[1 + \left(\frac{z_R}{z}\right)^2\right].$$

This leaves us with

$$A(\vec{r}) = A_0 \, e^{-\rho^2/w^2(z)} \, e^{-ik\rho^2/2R(z)} \, e^{-ip(z)}. \tag{2.14}$$

Now, all that is left to do, is find an expression for $p(z)$. We recall equation 2.11

$$p'(z) = -\frac{i}{q(z)} = -\frac{i}{z + iz_R}.$$

Integration from $dz' = 0$ to z gives us

$$ip(z) = \ln\left[1 - i\left(\frac{z}{z_R}\right)\right]. \tag{2.15}$$

Next, we use the identity

$$1 - i\left(\frac{z}{z_R}\right) = \ln\left[1 + \left(\frac{z}{z_R}\right)^2\right]^{1/2} - i \, \tan^{-1}\left(\frac{z}{z_R}\right)$$

to obtain:

$$e^{-ip(z)} = \frac{w_0}{w(z)} \, e^{i\zeta(z)} \tag{2.16}$$

where $\zeta(z) = \tan^{-1}(z/z_R)$ is called the *Gouy phase*. Finally, we assemble everything and end up with an expression for the electric field of a Gaussian beam:

$$
\begin{aligned}
E(\vec{r}) &= A(\vec{r})e^{-ikz} \\
&= A_0 \underbrace{\frac{w_0}{w(z)} \exp\left\{-\frac{\rho^2}{w^2(z)}\right\}}_{Radial\,amplitude} \times \underbrace{\exp\left\{-ikz - i\zeta(z)\right\}}_{Longitudinal\,phase} \times \underbrace{\exp\left\{-ik\frac{\rho^2}{2R(z)}\right\}}_{Radial\,phase}.
\end{aligned}
$$
$$\tag{2.17}$$

We have already identified the different contributions to this formula and are now going to further discuss the physical interpretation of what was established. A depiction of a Gaussian beam is given in Figure 1.

7
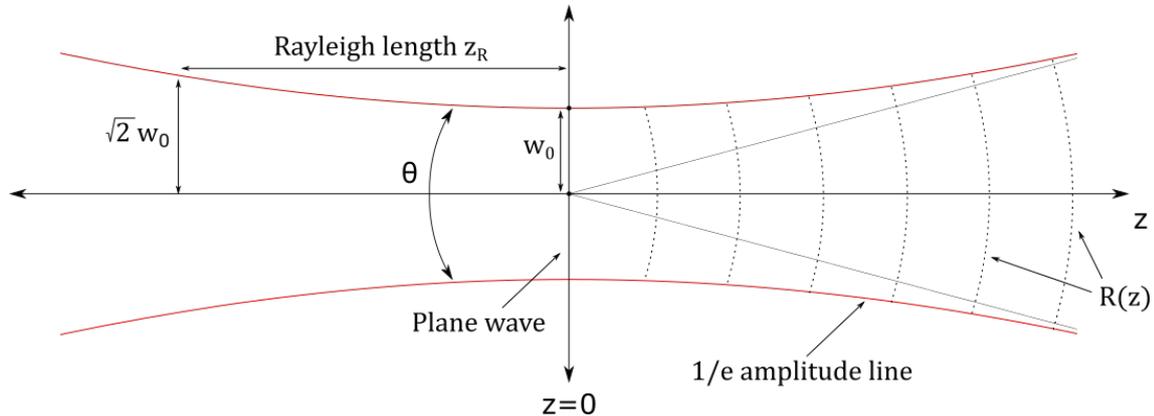
Figure 1: Spreading of a Gaussian beam. At $z = 0$ the beam has its minimal width, called the beam waist w_0, and the radius of curvature is infinite, therefore the beam resembles a plane wave. A distance z_R away from the waist, called the Rayleigh length, the spot size has increased by a factor of $\sqrt{2}$. For any given z, at a distance $\rho = w(z)$ the amplitude has dropped to $1/e$ of its maximum at $\rho = 0$. Θ: angular spread, $R(z)$: radius of curvature.

Gaussian beam properties

1. Amplitude

In equation 2.17 A_0 is the amplitude normalization factor. The first two terms after A_0, on the other hand, describe the radial dependence of the amplitude, as well as the change along z. For any given z, at a distance $\rho = w(z)$ the amplitude has dropped to $1/e$ of its maximum at $\rho = 0$:

$$\left| \frac{E(\vec{r})}{A_0} \right| = \frac{w_0}{w(z)} \exp\left[-\left(\frac{\rho}{w(z)} \right)^2 \right]. \tag{2.18}$$

As $w(z)$ increases with z the $1/e$ values move further out, as can be seen in Figure 1 as the outline of the beam. Since the flux has to stay constant along z, the factor $w_0/w(z)$ scales the peak amplitude of the field due to the spreading of the beam.

2. Beam Divergence

The beam has its minimum spot size of $2w_0$ at $z = 0$ and from there increases symmetrically in both directions:

$$w(z) = w_0 \sqrt{1 + \left(\frac{z}{z_R} \right)^2}.$$

From this equation it is clear, that at a distance $z = z_R$ (Rayleigh length) the beam spot size has increased by a factor of $\sqrt{2}$. For distances much larger
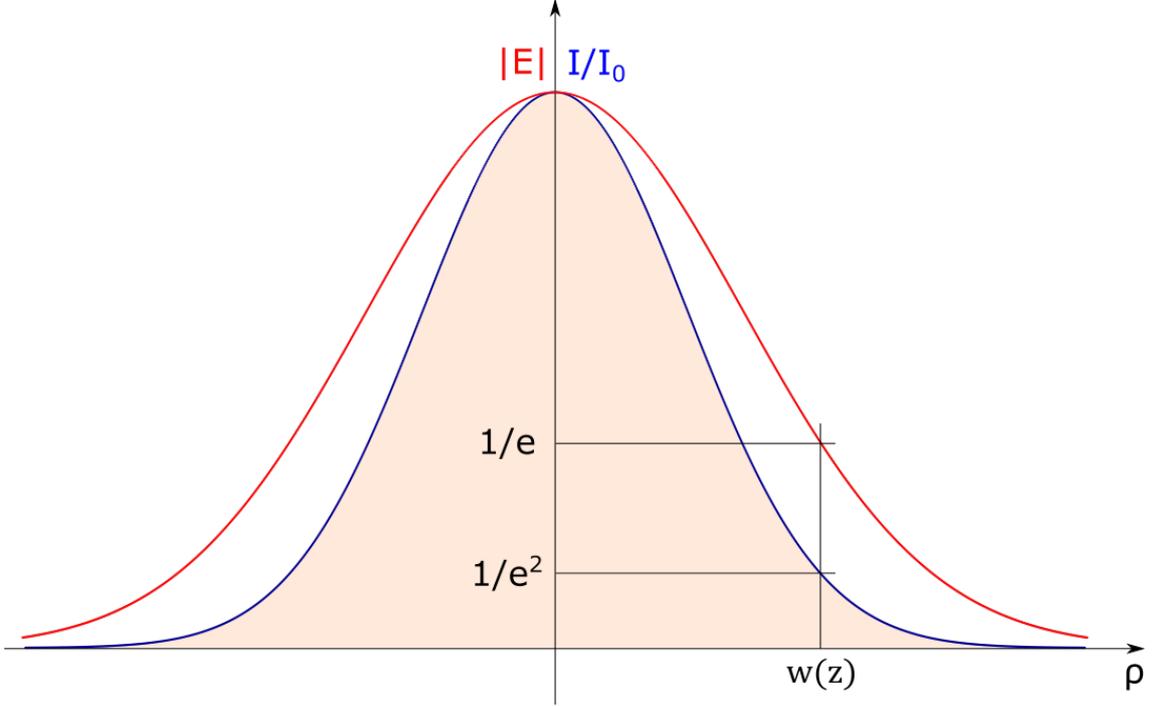
Figure 2: Transverse Gaussian beam profile. Plotted is the normalized intensity (blue) and the absolute value of the electric field (red) against the transverse position ρ. At $\rho = w(z)$ the values drop to $1/e$ and $1/e^2$ respectively, of their maximum value at $\rho = 0$.

than the Rayleigh length, i.e. $z \gg z_R$, the beam width is asymptotic to the solid black line in Figure 1, i.e. it grows approximately linear:

$$w(z \gg z_R) \to \frac{w_0 z}{z_R}. \tag{2.19}$$

In this regime we can define a beam divergence angle Θ:

$$\frac{\Theta}{2} = \frac{dw(z)}{dz} = \frac{w_0}{z_R}, \tag{2.20}$$

which is the minimum angular spread for a beam of spot size $2w_0$.

3. Intensity and Power

The time averaged intensity of the beam is given by

$$I(\vec{r}) = \frac{1}{2\eta}|E(\vec{r})|^2 = I_0 \frac{w_0^2}{w^2(z)} e^{-2\rho^2/w^2(z)}. \tag{2.21}$$

where $\eta = \sqrt{\mu_0/\varepsilon_0} = \frac{1}{\varepsilon_0 c}$ (μ_0 vacuum permeability, ε_0 vacuum permittivity and c speed of light) and $I_0 = A_0^2/2\eta$.

Figure 2 shows the normalized intensity and the absolute value of the electric field as a function of ρ. We can also see, that indeed the electric field value,

as well as the intensity, drop to $1/e$ and $1/e^2$ respectively, of their maximum value at $\rho = 0$, at a distance $\rho = w(z)$.

The total power transmitted by a Gaussian beam is

$$P_0 = \int_0^\infty d\rho \left(I(\rho, z) \cdot 2\pi\rho \right) = \frac{1}{2} I_0 \pi w_0^2. \tag{2.22}$$

Therefore, we can also express the intensity in terms of total power:

$$I(\rho, z) = \frac{2P_0}{\pi w^2(z)} e^{-2\rho^2/w^2(z)} \tag{2.23}$$

The power passing through a circle of radius r in the XY-plane, at position z, and centered at $x = y = 0$ is then given by

$$P(r, z) = P_0 \left[1 - e^{-2r^2/w^2(z)} \right]. \tag{2.24}$$

Therefore, the power transmitted through a circle of radius $r = w(z)$ is

$$\frac{P(z)}{P_0} = 1 - e^{-2}. \tag{2.25}$$

4. Phase

In equation 2.17 we distinguished between a longitudinal (axial) and a radial phase. Let's first look at the axial phase

$$\varphi(0, z) = -kz - \zeta(z) \tag{2.26}$$

The first part is the phase of a plane wave, $-kz$, followed by the so-called Gouy phase $\zeta(z) = \arctan(z/z_R)$. This factor provides a phase shift with respect to the plane wave, as can be seen in Figure 3. An easy way to visualize the Gouy phase is to imagine a simple Mach-Zehnder type interferometer to create an interference pattern. For $z \gg z_R$ the arctan function approaches $-\pi/2$, therefore $\zeta(-z) - \zeta(z) = \pi$. For our interferometer this means, that any on axis bright spot on one side will be conversed into a dark side on the opposite side and vice versa.

Now we recall the radial phase factor

$$\exp\left[-i \frac{k\rho^2}{2R(z)} \right].$$

The expression indicates that for $z \neq 0$ the XY-plane is not an equiphase surface, but we have curved wavefronts with radius of curvature
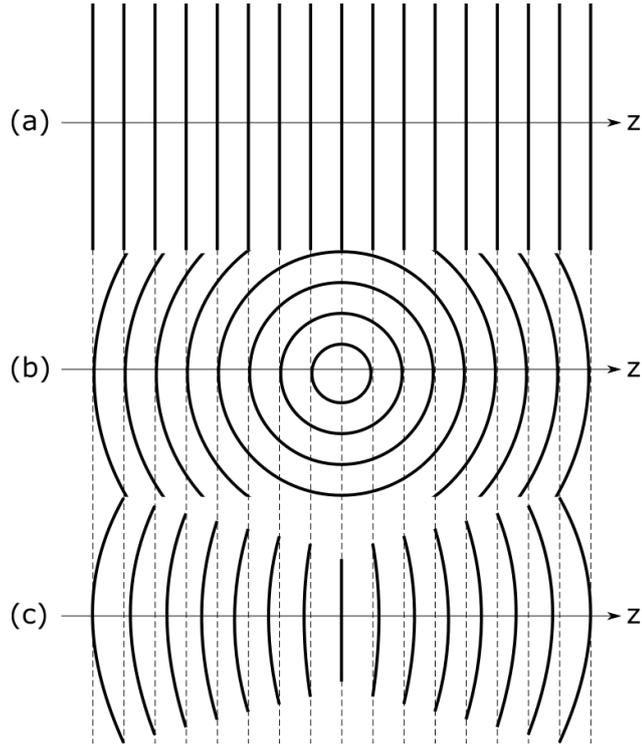
Figure 3: Visualization of the effect of the Gouy phase. **(a)** Plane wave pattern. **(b)** Spherical wave pattern **(c)** Gaussian beam pattern. Near the beam center, the Gaussian beam can be approximated by a plane wave, far away from it the beam resembles a spherical wave, phase retarded by $\pi/4$. Reproduced and adapted from [46].

$$R(z) = z \left[1 + \left(\frac{z_R}{z} \right)^2 \right].$$

Additionally, there is still the $z-$dependent longitudinal phase factor to consider. The total phase then accumulates to

$$\varphi = -k \left(z + \frac{\rho^2}{2R(z)} \right) - \zeta(z), \tag{2.27}$$

Surfaces of constant phase, i.e. $\varphi = 2\pi l, l \in \mathbb{Z}$ are located at points within the beam radius on each wavefront, as $R(z)$ and $\zeta(z)$ only vary slowly. This condition defines a parabolic surface with radius of curvature $R(z)$. We can now make approximations when looking close to the beam center or far away from it:

For $z \ll z_R$ and $\rho \ll w_0$ we get $R(z) \approx \frac{z_R^2}{z}$ and $\zeta(z) \approx 0$. Therefore

$$\varphi \approx -kz - k\frac{\rho^2}{2z_R^2}z = -kz\left[1 + \underbrace{\frac{\rho^2}{2z_R^2}}_{\ll 1}\right] \approx -kz$$

we get a plane wave approximation near the beam center.

Now consider $z \gg z_0$, ρw_0, i.e. the paraxial case. We get $R(z) \approx z$ and $\zeta(z) \approx \frac{\pi}{2}$.

$$\Rightarrow \varphi \approx -kz - \frac{k\rho^2}{2z} - \frac{\pi}{2} = -\frac{\pi}{2} + k\left(z + \frac{\rho^2}{2z}\right)$$

and we get a parabolic wave. The result of this is that if we look at the beam from $z \gg z_0$ it appears to originate at $z = 0$. However, if we move closer and closer towards that point, the center of appearance retreats until at $z = 0$ it is at infinity, i.e. we have a plane wave.

Tightly focused beam

The paraxial approximation we used to derive the electric field breaks down for a strongly focused beam. The exact solution is now generally obtained by a numerical fit, where the Rayleigh length becomes a free parameters that has to be obtained by the fit. Furthermore, we have to account for asymmetries along the $x-$ and $y-$direction of the beam, arising from the polarization of the beam. We dropped the vectorial character of the electric field earlier because up until now, the results were independent of the polarization direction. We now reintroduce the polarization vector $\vec{p}$. Furthermore, we implement the possibility of asymmetry by splitting $w(z)$ into its $w_x(z)$ and $w_y(z)$ components. The electric field then reads

$$\vec{E}(x,y,z) = A_0 \frac{1}{\sqrt{1 + (z/z_R)^2}} \cdot e^{-x^2/w_{xx}^2(z)} \cdot e^{-y^2/w_{yy}^2(z)} \cdot e^{i\varphi(\rho,z)} \cdot \vec{p} \qquad (2.28)$$

where $w_{ij}^2(z) = w_i w_j (1 + (z/z_R)^2)$ and w_x and w_y are the beam waists along the $x-$ and $y-$direction, respectively. The intensity of the beam can now be expressed as

$$I(x,\vec{y},z) = \frac{2P_0}{\pi w_{xy}^2(z)} e^{-x^2/w_{xx}^2(z)} e^{-y^2/w_{yy}^2(z)}. \qquad (2.29)$$

2.2 Optical tweezers

Optical tweezers were first presented in 1986 by Arthur Ashkin [18]. The single beam optical gradient trap demonstrated trapping of dielectric particles with sizes between $\sim 25\,\text{nm}$ and $10\,\mu\text{m}$. An exact analytical solution for the forces acting on a dielectric sphere in a focused laser beam is given by Mie theory [48] or an extended two-component model [49]. However, when restricting the particle size, approximations can give a good working intuition. On the one hand, for dielectric microparticles much larger than the tweezers wavelength λ (diameter $d \gg \lambda$) ray optics can be used to describe the forces acting on the particle [50]. On the other hand, nanoparticles much smaller than the wavelength ($d \ll \lambda$) can be approached with the Rayleigh approximation.
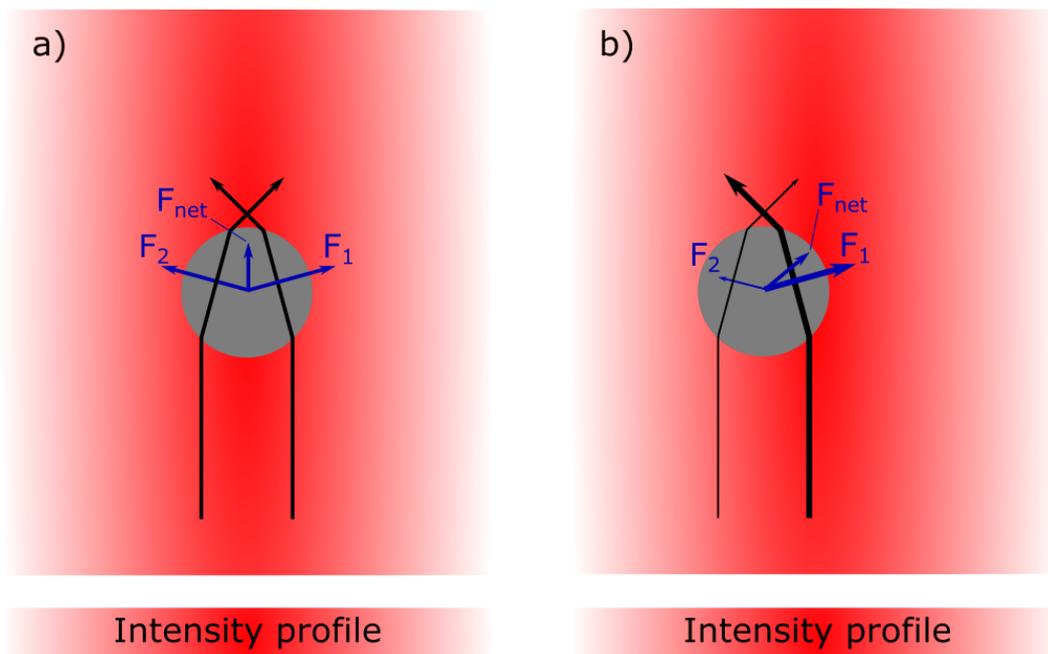
Ray optics

Let us first consider a transparent, spherical microparticle sitting in an unfocused tweezers beam (Figure 4). Furthermore, we assume a Gaussian intensity profile, as described before. A particle inside the beam is subject to forces arising from refraction at its surface, as the light rays change direction when entering and exiting the particle. This momentum change induced on a light ray is imparted on the particle. The net force thus acting on the particle depends on the position in the beam profile. If located perfectly on the beam axis (Figure 4a), the intensity profile around the particle is radially symmetric. Therefore, the net force only points in the direction of beam propagation. Contrary to that, if the particle is displaced from the beam center (Figure 4b), a lateral component to that force is added, as the more intense rays will impart a larger momentum on the particle. The result is a radial restoring force towards the beam axis. Axial stability, however, is only possible if the net force in beam direction is compensated, e.g. by gravity.

For a strongly focused Gaussian beam (Figure 5) the particle now also experiences a force that is dependent on the axial position, in addition to the radial restoring force.

In addition to the radial restoring force, a particle in a strongly focused Gaussian beam (Figure 5) also experiences a force that is dependent on the axial position. Again, refraction of the light rays imparts a momentum on the particle. This time, however, the net force points to the laser focus instead of being parallel to the direction of beam propagation, regardless of whether the particle is front of (Figure 5a) or behind the focal point (Figure 5b).

In reality, there exist no perfectly transparent particles, thus surface reflection,

Figure 4: Ray optics for a microparticle in an unfocused tweezers beam. **(a)** A particle perfectly centered on the beam axis only experiences a net force in the direction of beam propagation. **(b)** Due to the intensity gradient of the beam and the resulting imbalance of momentum impartation along the sphere, a particle displaced form the center is subject to a lateral net force that points towards the beam axis. Reproduced and adapted from [51].
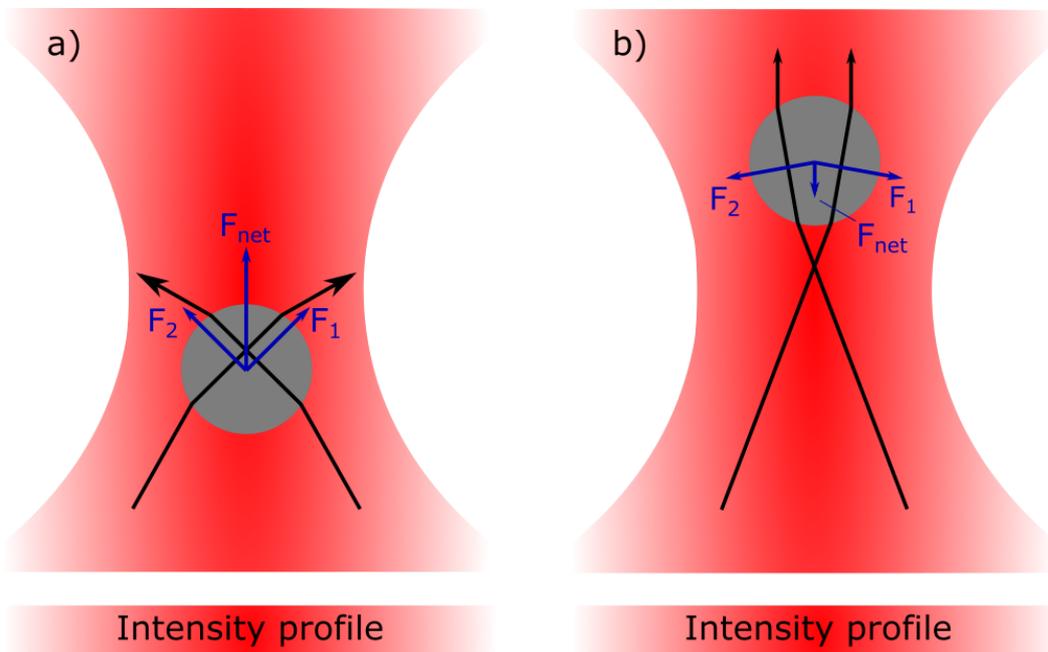
Figure 5: Ray optics for a microparticle in a focused tweezers beam. In addition to the forces in an unfocused beam the particle is subject to an axial force. Due to the momentum change of the refracted rays a spherical particle experiences a net force towards the laser focus, regardless of whether it is front of **(a)** or behind the focal point **(b)**. The position of the microparticle in equilibrium with the scattering force depends on other impacting forces, e.g. gravity. Reproduced and adapted from [51].

absorption and scattering has to be taken into account. All these effects will push the particle in the direction of beam propagation. Therefore, in order to be able to trap the particle, the axial restoring force has to be greater than the push-off. Surface reflection depends on the relative index of refraction of the particle and the surrounding medium $m = n_p/n_m$ [52], where n_p is the refractive index of the particle and n_m that of the medium. The larger m, the more surface reflection occurs. Consequently, it is easier to trap particles in a surrounding medium with higher refractive index, e.g. water compared to air [53].

Rayleigh approximation

Now let's consider a nanosphere with radius R and dielectric constant ε sitting in a Gaussian beam with waist $w_0 \gg R$, propagating along z. Without loss of generality, we assume a linearly polarized beam in the x-direction $\vec{p} = \vec{e}_x$. While a beam with circular polarization can provide full rotational control [54], it would unnecessarily complicate the following calculations without providing a better understanding.

The subsequent calculations follow the general approach presented in [55]. In the Rayleigh approximation the particle can be treated as a point-like dipole and we divide the optical force acting on the particle into two terms, the non-conservative scattering force F_{scatt} and the conservative gradient force F_{grad}. In general, the polarizability of a particle of arbitrary shape and size is given by a tensor of rank two, α_{ij}. For our simplified case of a spherical particle, this tensor reduces to a scalar α and is given by the Clausius-Mosotti relation:

$$\alpha = 4\pi\varepsilon_0 \cdot R^3 \frac{\varepsilon - 1}{\varepsilon + 2}, \tag{2.30}$$

where ε_0 is the vacuum permeability.
The scattering force can be explained as follows: the point dipole induced by the electric field follows the field's harmonic oscillation and acts as an oscillating electric dipole which scatters waves in all directions. The momentum thus imparted on the particle exerts a force proportional to the scattering cross section σ_{scatt} of the particle:

$$\vec{F}_{scatt}(\vec{r}) = \frac{\sigma_{scatt}}{c} I(\vec{r}) \vec{e}_z, \tag{2.31}$$

where c is the speed of light, $I(\vec{r})$ the intensity of the Gaussian beam as defined in 2.1 and $\vec{e}_z$ the unit vector along the beam propagation axis. A spherical particle in the Rayleigh approximation scatters light isotropically and σ_{scatt} is equal to

$$\sigma_{scatt} = \frac{8}{3}\pi k^4 R^6 \left(\frac{\varepsilon - 1}{\varepsilon + 2}\right)^2.$$

Substituting this, as well as the intensity from equation 2.23^1, we end up with

$$\vec{F}_{scatt}(\vec{r}) = \frac{16}{3}\frac{Pk^4R^6}{cw^2(z)}\left(\frac{\varepsilon - 1}{\varepsilon + 2}\right)^2 \cdot \exp\left(-2\frac{\rho^2}{w^2(z)}\right)\vec{e}_z. \qquad (2.32)$$

Therefore, the scattering force scales linearly with the power of the laser and as R^6 with the particle radius and is oriented in beam propagation direction.

The second component is the gradient force arising from the Lorentz force acting on the induced dipole. The instantaneous (time dependent) gradient force is given by

$$\vec{F}_{grad}(\vec{r},t) = \frac{\alpha}{2}\vec{\nabla}\vec{E}^2(\vec{r},t). \qquad (2.33)$$

For a steady state particle, the gradient force is the time-averaged version of equation 2.33:

$$\begin{aligned}
\vec{F}_{grad}(\vec{r}) &= \langle\vec{F}_{grad}(\vec{r},t)\rangle \\[2mm]
&= \frac{\alpha}{2}\vec{\nabla}\langle\vec{E}^2(\vec{r},t)\rangle \\[2mm]
&= \frac{\alpha}{4}\vec{\nabla}|\vec{E}(\vec{r})|^2 \\[2mm]
&= \frac{\alpha}{2\varepsilon_0 c}\vec{\nabla}I(\vec{r})
\end{aligned} \qquad (2.34)$$

It is easy to see from this formula that the gradient force is a conservative force (as the name already suggests) - contrary to the scattering force. The gradient force scales as R^3 and always points along the intensity gradient, i.e. towards the beam waist, and thus acts as a restoring force. Consequently, the gradient force acts as a particle trap, whereas the scattering force pushes particles away. A particle will be trapped where the total force $\vec{F}(\vec{r}) = \vec{F}_{scatt}(\vec{r}) + \vec{F}_{grad}(\vec{r}) = 0$. In order to achieve a stable trap, the gradient force should be larger than the scattering force. Since the scattering force scales as R^6 compared to the R^3 scaling of the gradient force, the former will weaken much faster when reducing the particle size. In fact, in

---

[1] In the paraxial approximation. For a strongly focused beam we would have to insert the modified Gaussian intensity as defined in 2.29. Furthermore, the scattering force then also has components along the x- and $y-$direction that cannot be neglected.

$z-$direction, the ratio between maximal gradient force and scattering force is given by [40]

$$\beta = \frac{\vec{F}_{grad} \cdot \vec{e}_z}{\vec{F}_{scatt}} \propto \frac{1}{R^3} \frac{\varepsilon + 2}{\varepsilon - 1} \tag{2.35}$$

and is independent of the laser power P but only depends on particle size and dielectric constant. However, if the particle size is too small, the overall optical forces become so weak, that the system becomes susceptible to any external disturbances, e.g. collisions with surrounding gas molecules.

So far, we have only considered a single beam. When implementing a second beam, identical in power, wavelength and focus but counterpropagating, the scattering force of the two beams cancels out. Alternatively, one can use other force, e.g. gravity, to counteract the scattering force to stabilize the trap.

Harmonic approximation

The motion of a trapped particle can be described by a thermally driven, damped, three-dimensional harmonic oscillator [40]. The time averaged gradient force gives rise to the conservative potential

$$U_{opt} = \frac{\alpha}{2\varepsilon_0 c} I(\vec{r}) = \frac{\alpha P}{\pi \varepsilon_0 c w^2(z)} e^{-2\rho/w^2(z)}, \tag{2.36}$$

which has its minimum at the point of origin, i.e. $\rho = z = 0$. If the particle motion is small, we can expand the scattering force to first order:

$$\vec{F}_{scatt} = \frac{\sigma_{scatt}}{c} I_0 \vec{e}_z + \mathcal{O}(z^2). \tag{2.37}$$

Similarly, linearization of the optical potential yields three decoupled oscillation frequencies:

$$\Omega_{x,y}^2 = \frac{4P\alpha}{m\pi\varepsilon_0 c w_0^2} \frac{1}{w_0^2} \tag{2.38}$$

$$\Omega_z^2 = \frac{4P\alpha}{m\pi\varepsilon_0 c w_0^2} \frac{1}{z_R^2} \tag{2.39}$$

The equations of motion are those of a harmonic oscillator with a damping factor Γ_0, dominated by friction with gas particles and a thermal driving force F_{th} caused by Brownian force noise [40]. Along the $x-$direction the equation of motion reads

$$m\ddot{x} + m\Gamma_0 \dot{x} + m\Omega_x^2 x = F_{th}. \tag{2.40}$$

17

The equation in $y-$direction looks exactly the same, but in the $z-$direction we also have to account for the scattering force driving the particle motion:

$$m\ddot{z} + m\Gamma_0\dot{z} + m\Omega_z^2 z = F_{th} + F_{scatt} \tag{2.41}$$

2.2.1 Feedback cooling

As mentioned before, a trapped particle will be subject to a thermal force arising from Brownian motion. Only in a perfect vacuum would this force disappear. In the following we will assume a dielectric particle trapped in a dual beam optical tweezers system. Therefore, the scattering force along z cancels out and we can merge the equations of motion to a single equation

$$\ddot{q}(t) + \Gamma_0\dot{q}(t) + \Omega_0^2 q(t) = \frac{1}{m}F_{th}(t) \tag{2.42}$$

where $q = x, y, z$ and Ω_0 is the oscillation frequency along q. The stochastic Brownian force is a fluctuating Langevin force that can be expressed as [56]

$$\langle F_{th}(t)F_{th}(t')\rangle = 2m\Gamma_0 k_B T_0 \delta(t - t'). \tag{2.43}$$

for a particle of mass m and equilibrium temperature T_0. The Brownian stochastic force is a driving force for the motion of the particle, whereas the damping term $m\Gamma_0\dot{q}$ tends to counteract this motion. However, the damping constant Γ_0 also impacts F_{th}. This leads to two different regimes where one term will dominate over the other [53]. If the mechanical energy (kinetic + potential energy) of the particle exceeds $k_B T_0$, the damping term will outgrow the thermal driving force. On the other hand, if the mechanical energy is lower than $k_B T_0$, this turns the other way around. Therefore, at thermal equilibrium, the average mechanical energy of the particle will level off at $k_B T_0$ (neglecting other influences) in each direction.

The damping rate Γ_0 at normal pressure around $p = 1\,\mathrm{bar}$ is given by Stokes' law:

$$\Gamma_0 = \frac{6\pi\eta R}{m} \tag{2.44}$$

where η is the viscosity of the surrounding medium and m and R the mass and radius of the particle, respectively. For lower pressures, this equation has to be altered as we enter the regime of kinetic gas theory. Here we assume that the mean free path length $\bar{l} \propto 1/p$ is much larger than the particle size. Kinetic theory then tells us that Γ_0 is given by [57]

$$\Gamma_0 = \frac{6\pi\eta R}{m} \frac{0.619}{0.619 + \text{Kn}} \left(1 + \frac{0.31\,\text{Kn}}{0.785 + 1.152\,\text{Kn} + \text{Kn}^2} \right) \qquad (2.45)$$

where $\text{Kn} = \bar{l}/R$ is the Knudsen number and Γ_0 becomes proportional to p.

So, a particle driven by Brownian force noise and damped by collisions with gas molecules, will thermalize to T_0. We can, however, go below that limit by adding an additional cooling force. In the following we will discuss two active feedback cooling schemes: *parametric feedback*, where the laser power is modulated to alter the trap stiffness depending on the particle's position, and *cold damping* where an external force proportional to the velocity of the particle is applied to slow its motion. Feedback cooling is a useful tool to reach high vacuum and counteract trap instabilities that would otherwise cause a particle loss.
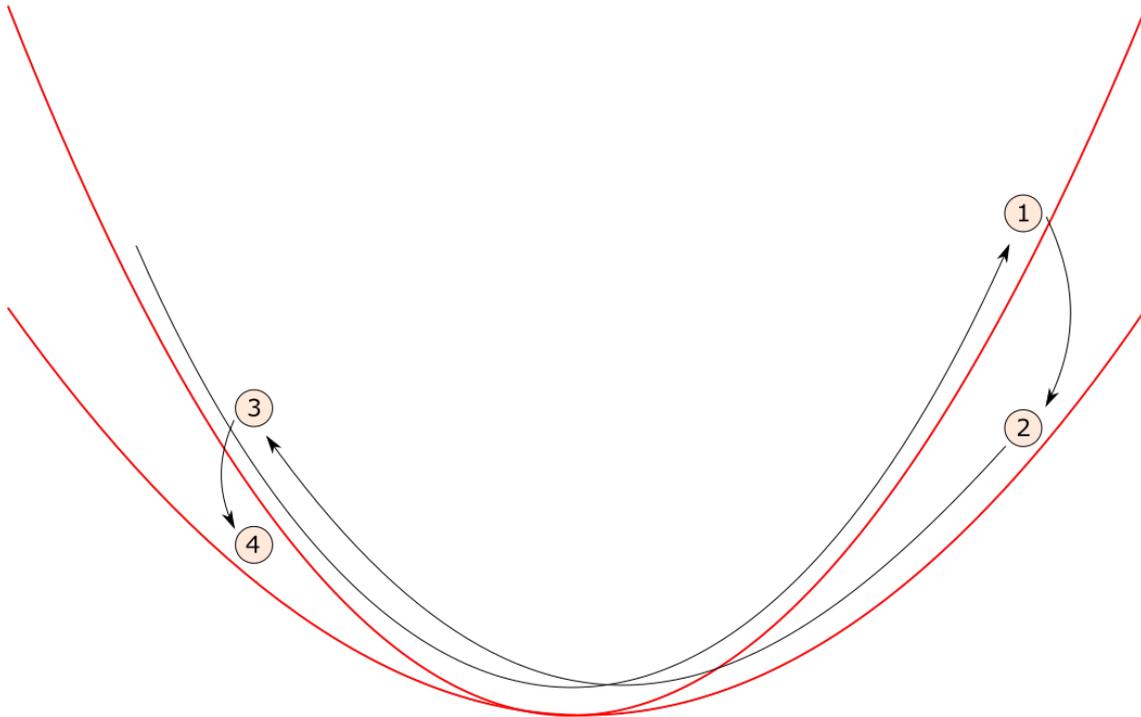
2.2.1.1 Parametric feedback

The idea behind parametric feedback cooling is to increase the trap stiffness whenever the particle moves away from the trap center and reducing it when it moves back. A schematic of this method can be seen in Figure 6. Experimentally, this is achieved by applying a modulation of the laser power at twice the mechanical frequency of the trap, phase shifted with respect to particle motion. The sign of this phase lag decides whether the particle is cooled or heated during this process. In more detail, a frequency doubled signal can be obtained by multiplying the particle's position $q(t)$ (obtained by the light scattered off the particle) with its time derivative $\dot{q}(t)$. This can be done independently for each direction. Each individual signal is phase shifted and summed to a single feedback signal to modulate the trapping laser's power. Therefore, 3D-feedback cooling can be achieved by a single beam. A detailed explanation of parametric feedback cooling can be found in [56]. We will follow their steps to get a good hold of the fundamental theoretical idea behind this scheme.

Equation 2.42 is now altered on the right-hand side by addition of a non-conservative optical feedback force F_{fb}. As can be seen in equations 2.38 and 2.39 the trapping frequencies, and therefore the trap stiffness $k = m\Omega_0^2$, scale linearly with the laser power P. Therefore, $F_{fb} = \delta k(t)q(t)$, where $\delta k(t)$ is the modulation of the trap stiffness, and

$$\ddot{q}(t) + \Gamma_0\dot{q}(t) + \Omega_0^2 q(t) = \frac{1}{m}\left[F_{th}(t) + F_{fb}(t) \right]. \qquad (2.46)$$

The feedback force leads to shifts $\delta\Gamma$ and $\delta\Omega$ in the damping Γ_0 and oscillation

19

Figure 6: Schematic representation of parametric feedback cooling. By modulation of the trapping laser's power, the trap stiffness is increased whenever the particle moves away from the trap center and decreased it when it moves back. Reproduced from [56].

frequency Ω_0 respectively. Fourier transformation of 2.46 leads to the power spectral density $S_q(\omega)$

$$
\begin{aligned}
S_q(\omega) &= \int_{-\infty}^{\infty} \langle q(t)q(t-t')\rangle \, e^{-i\omega t'} dt' \\[2mm]
&= \frac{\Gamma_0 k_B T_0}{\pi m} \frac{1}{([\Omega_0 + \delta\Omega]^2 - \omega^2)^2 + \omega^2[\Gamma_0 + \delta\Gamma]^2}
\end{aligned}
\tag{2.47}
$$

From that we can obtain the mean square displacement $\langle q^2 \rangle$ via integration of both sides over ω:

$$
\langle q^2 \rangle = \frac{k_b T_0}{m(\Omega_0 + \delta\Omega)^2} \frac{\Gamma_0}{\Gamma_0 + \delta\Gamma}
\tag{2.48}
$$

Considering the equipartition theorem, we can define an effective center of mass temperature

20

$$T_{\text{eff}} = \frac{1}{k_B} m (\Omega_0 + \delta\Omega)^2 \left\langle q^2 \right\rangle$$

$$\tag{2.49}$$

$$= T_0 \frac{\Gamma_0}{\Gamma_0 + \delta\Gamma}$$

where T_0 is the equilibrium temperature in absence of feedback. The minimal achievable effective temperature is determined by the cooling rate $\delta\Gamma$. Depending on the sign, the temperature can be either raised or lowered. Furthermore, lowering the environmental damping Γ_0, i.e. going to higher vacuum, also lowers the minimal attainable temperature.

Parametric feedback cooling down to $50\,\text{mK}$ was reported in 2012 at a residual pressure of $10^{-5}\,\text{mbar}$ [57]. But we can ask ourselves, how much further down could one go? What about the quantum ground state? We can define the ground state of a quantum harmonic oscillator as a state with mean occupation number $\langle n \rangle < 1$, where [57]

$$\langle n \rangle = \frac{k_B T_{\text{eff}}}{\hbar \Omega_0}. \tag{2.50}$$

Therefore, $T_{\text{eff}} \overset{!}{<} \hbar\Omega_0/k_B$. For example, an oscillation frequency of $\Omega_0 = 2\pi \cdot 100\,\text{kHz}$ would therefore require $T_{\text{eff}} \lesssim 5\,\mu K$.

Feedback cooling relies on the readout of the position of the particle. The particle scatters photons that now carry information about the particle's position and are recorded by a detector. A fundamental limit for this technique is therefore imposed by the measurement uncertainty induced by photon shot noise. Shot noise is defined by the photon number fluctuations $\Delta N \propto \sqrt{N}$, where N is the mean scattered photon number [57], which intrinsically depends on the scattering cross section σ of the particle. Since every photon scattered off the particle transfers a momentum $\hbar k$ onto the particle, the momentum uncertainty is given by

$$\Delta p = \hbar k \Delta N = \hbar k \sqrt{N}. \tag{2.51}$$

According to the uncertainty principle $\Delta q \Delta p \geq \hbar/2$ the minimum position uncertainty is

$$\Delta q = \frac{1}{2k\sqrt{N}}. \tag{2.52}$$

Therefore, the position measurement improves with increasing laser power, since

$N = P\Delta t/(\hbar k c)$. However, in order to determine the limits of the effective center of mass temperature, imposed intrinsically by parametric feedback cooling, we have to look at the energy uncertainty [58]

$$\Delta E = \frac{1}{2}\left(m\Omega_0^2\Delta q^2 + \frac{\Delta p^2}{m}\right)$$

$$= \frac{1}{2}\left(\frac{m\Omega_0^2}{4k^2N} + \frac{\hbar^2 k^2 N}{m}\right). \tag{2.53}$$

The minimal uncertainty, known as the standard quantum limit (SQL), is achieved for a photon number $N_{\mathrm{SQL}} = m\Omega_0/(2\hbar k^2)$. Indeed, $\Delta E_{\mathrm{SQL}} = \hbar\Omega_0/2$ would allow for quantum ground state cooling.

However, there exists another factor we have not yet accounted for. Momentum transfer by photon recoil is generally negligibly small compared to the mechanical momentum of the oscillator. But when collisions with residual gas molecules become increasingly more insignificant at low temperatures, photon recoil heating takes over as the dominating form of heating.

If the energy of a photon is given by $(\hbar k)^2/2m$ and the energy separation between oscillator states by $\hbar\Omega_0$, then the number of photons N_{recoil} it takes to excite a transition is [58]

$$N_{\mathrm{recoil}} = \frac{2m\Omega_0}{\hbar k^2}, \tag{2.54}$$

which is four times as high as N_{SQL}. However, the ability to scatter is defined by the particle's scattering cross section σ_{scatt}. Therefore, it takes a time Δt until $N_{\mathrm{scatt}} = N_{\mathrm{recoil}}$. The recoil heating rate Γ_{recoil} is given by the inverse of Δt and is proportional to $\sigma_{\mathrm{scatt}}/\Omega_0$ and therefore scales as $(R/\lambda)^3$ with the nanoparticle radius R and laser wavelength λ. Ultimately, the experimental parameters can be tweaked such that the dominant form of noise comes from shot noise.

2.2.1.2 Cold damping

Instead of modulating the trapping potential itself one can apply an external force to slow down the center of mass motion of the particle. Since the theoretical groundwork is inherently similar to that of parametric feedback cooling, we will only briefly sketch the basics and focus on the differences.

Generally, an external force proportional to the velocity of the particle but in opposite direction is applied

$$F_{cd} = -\Gamma_{cd}\dot{q}(t) \tag{2.55}$$

Therefore, the equation of motion reads

$$\ddot{q}(t) + (\Gamma_0 + \Gamma_{cd})\dot{q}(t) + \Omega_0^2 q(t) = F_{th}(T) \tag{2.56}$$

Contrary to Γ_0, Γ_{cd} only appears as a damping factor on the left-hand side, but does not enter the heating term. Hence, this technique is commonly referred to as *cold damping*. Of course, similarly to parametric feedback, the particle's motion can be amplified by change of sign of the damping constant Γ_{cd}.

Analog to equation 2.47 in parametric feedback, the power spectral density is given by

$$S_q(\omega) = \frac{\Gamma_0 k_B T_0}{\pi m} \frac{1}{(\Omega_0^2 - \omega^2)^2 + \omega^2[\Gamma_0 + \Gamma_{fb}]^2}. \tag{2.57}$$

However, contrary to parametric feedback, there is no shift in mechanical oscillation frequency Ω_0 as the trapping field is not altered. From this we can again define an effective center of mass temperature

$$T_{\text{eff}} = T_0 \frac{\Gamma_0}{\Gamma_0 + \Gamma_{cd}}. \tag{2.58}$$

The biggest difference between parametric feedback cooling and cold damping lies in the experimental realization. In parametric feedback, an already existing, but previously constant, parameter in the equation of motion is modulated over time, thus getting the name 'parametric'. In cold damping, on the other hand, an external force is applied. In reality, this can be accomplished in several ways. Recently, 1D-cooling down to $100\,\mu K$ has been achieved by cold damping via the electric field of a capacitor [59]. Previously, a purely optical 3D-cooling scheme relying on the scattering force of three orthogonal laser beams was able to cool a glass microsphere as low as $1.5\,\text{mK}$ [60]. The clear drawback of this scheme is the much more tedious experimental implementation compared to parametric feedback cooling. While it still requires a 3D detection system, it also requires a total of four beams that have to be aligned and individually controlled - compared to only a single beam in parametric feedback cooling.

2.3 Cavity optomechanics

Due to the success of atom cooling in the 1990s, the idea was quickly extended to molecules and nanoparticles. However, these more complex objects suffer from a lack of narrow energy level structure and closed cyclic transitions. Therefore, conventional direct laser cooling schemes used in atom cooling fail. A method to circumvent this limitation was proposed in 2000 [32], exploiting the off-resonant optomechanical interaction between a nanoparticle and an optical cavity. Even though still a young field of research, a multitude of different schemes have been explored: Cavity cooling of an optically trapped silica sphere [37], as well as for free silicon nanoparticles [38] was first demonstrated in 2013. Since then cooling of charged particles levitated inside a Paul trap [61] and cooling of the rotational degrees of freedom has been reported [62]. Cavity cooling can be realized by pumping of the cavity field, or by coherent scattering from a secondary beam [63].

In this chapter we will introduce the theoretical groundwork for cavity cooling. For a detailed, quantized theoretical description of this matter we recommend [64]. We will start with a brief introduction to the general concept of optical cavities, followed by a classical description of light-matter interaction of dielectric nanoparticles inside a cavity. After this, we will review cavity cooling of a strongly pumped cavity, as well as coherent scattering cooling. To conclude this chapter, an overview of cavity stabilization techniques and nanoparticle detection methods is given.

2.3.1 Optical cavities

In its simplest form, an optical cavity consists of two planar mirrors, a distance L apart[2]. Light inside the cavity is reflected multiple times at the mirror surfaces and forms standing waves for certain resonance frequencies. These resonance frequencies are discrete values separated by a constant frequency

$$\Delta\nu_{FSR} = \frac{c}{2L} \tag{2.59}$$

called the *free spectral range*, where L is the length of the cavity and c the speed of light. For perfect, lossless mirrors, the resonance frequencies resemble delta functions in frequency space. In reality mirrors have a reflectivity r smaller than 100% and the eigenmodes turn into extended peaks in the frequency domain (Figure 7) whose full width at half maximum (FWHM) $\Delta\nu$ is given by

---

[2]More generally, L denotes the optical path length between the mirrors.
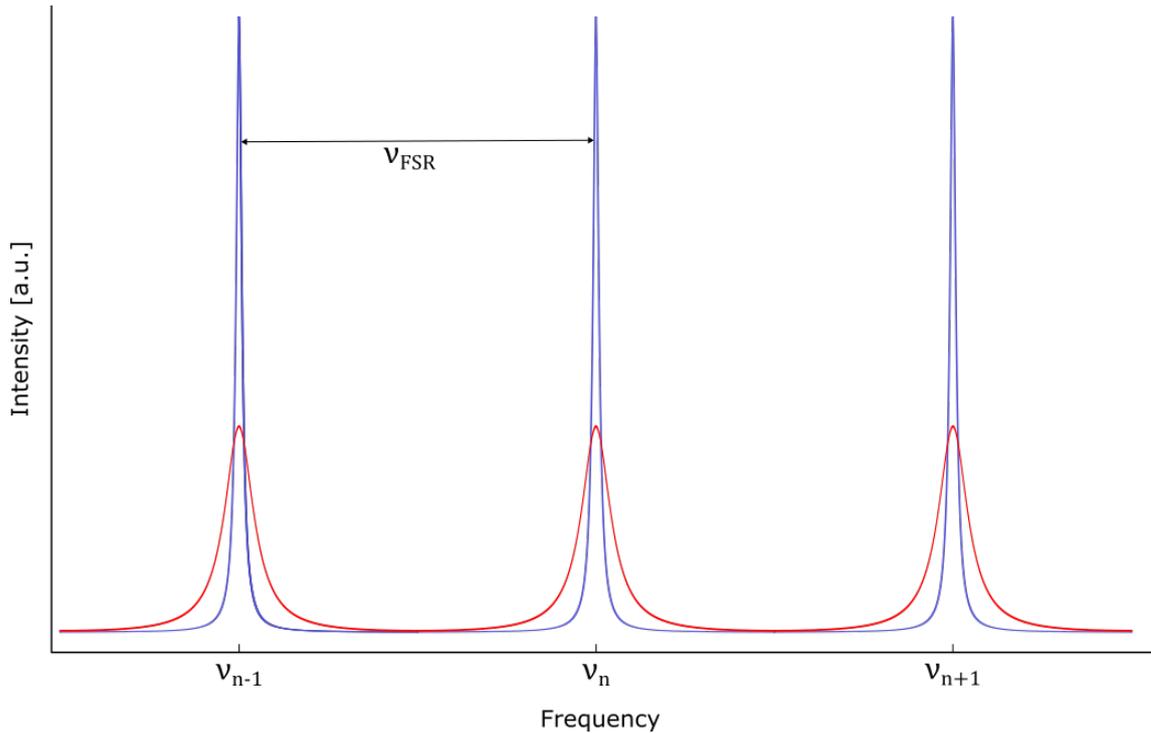
Figure 7: Frequency spectrum of transmitted intensity through a low-finesse (red curve) and high-finesse (blue curve) cavity. The cavity can only sustain standing light waves at integer multiples of the free spectral range ν_{FSR}. The spectrum of a cavity with lossless mirrors would resemble a series of delta functions. Mirrors with finite reflectivity r are represented by extended peaks whose full width at maximum (FWHM) scales inverse proportional with the cavity finesse.

$$\Delta\nu = \frac{\nu_{FSR}}{\mathcal{F}}. \tag{2.60}$$

$\mathcal{F}$ is called the *finesse* of the cavity and is a measure for the temporal confinement of the light in the cavity and depends on the mirror reflectivity r as

$$\mathcal{F} = \frac{\pi\sqrt{r}}{1-r}. \tag{2.61}$$

Furthermore, due to the limited finesse light leaks out of the cavity. This leakage is characterized by the cavity decay rate, or cavity linewidth $\kappa = c\pi/2\mathcal{F}L$.

Only the eigenmodes of the cavity are sustained while any other frequencies are suppressed by destructive interference. The fundamental transverse mode of an optical cavity consisting of spherical mirrors is a Gaussian beam.

High finesse cavities are commonly used as spectral filters, for laser stabilization [65] or even to produce a laser beam [25] when filling the cavity with an active medium.

There are many different possibilities to realize an optical cavity. Simple forms comprise of two mirrors, planar, spherical or a combination of both. But mirrors
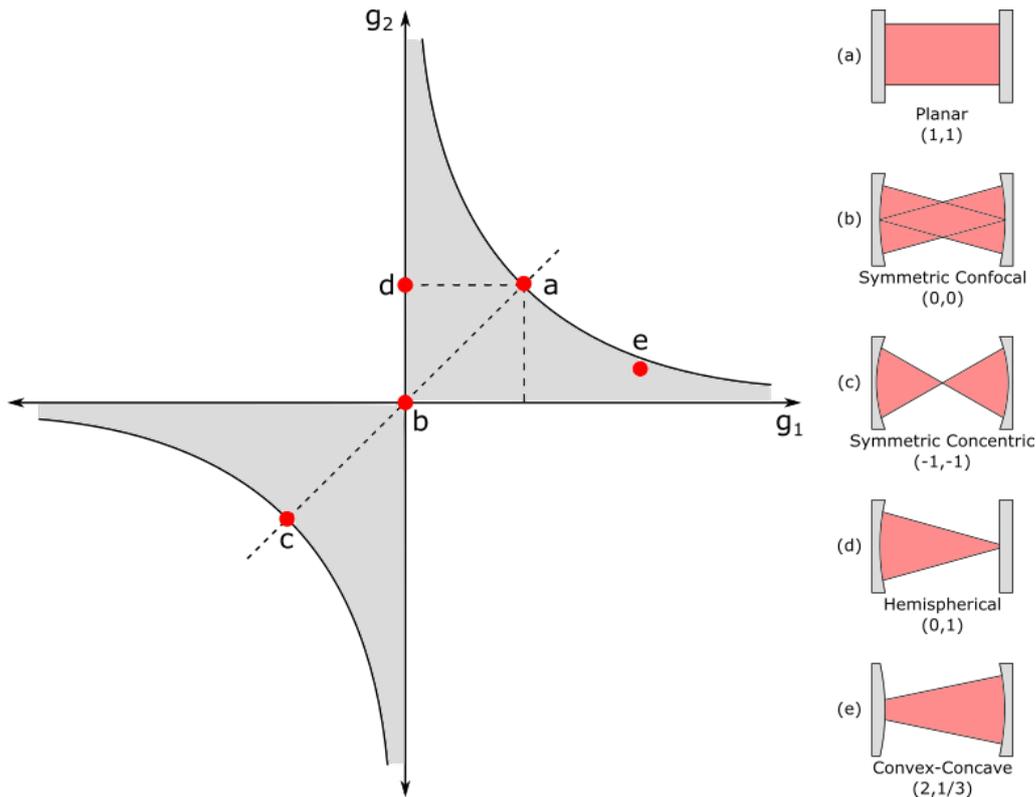
Figure 8: Visualization of the stability criterion for cavity arrangements. Common configurations are shown to the right. Arrangements that lie on the dashed line are symmetric, i.e. the mirrors have identical radii of curvature. Reproduced and adapted from [66].

can also be arranged to form 2D- or 3D cavities, for example as ring- or rectangular cavities. Less conventional arrangements make use of whispering gallery modes in microdisks, -toroids or -spheres [66]. In the following we will concentrate on cavities that consist of two mirrors facing each other. Depending on the radii of curvature of the mirrors R_1, R_2 and the length of the cavity L, we can determine if an arrangement is stable or not, i.e. whether or not light rays are confined for multiple reflections. From ray transfer matrix analysis [66] we find the stability criterion

$$0 \leq \underbrace{\left(1 - \frac{L}{R_1}\right)}_{g_1} \underbrace{\left(1 - \frac{L}{R_2}\right)}_{g_2} \leq 1. \tag{2.62}$$

A visualization of this criterion is given in Figure 8. Common configurations are indicated in the diagram and depicted to the right. Symmetric cavities have identical mirror curvatures, i.e. $g_1 = g_2$. The criterion then simplifies to $0 \leq \frac{L}{R} \leq 2$. The three cases where $L/R = 0, 1, 2$ correspond to planar, confocal and concentric cavities respectively, and are especially prominent.
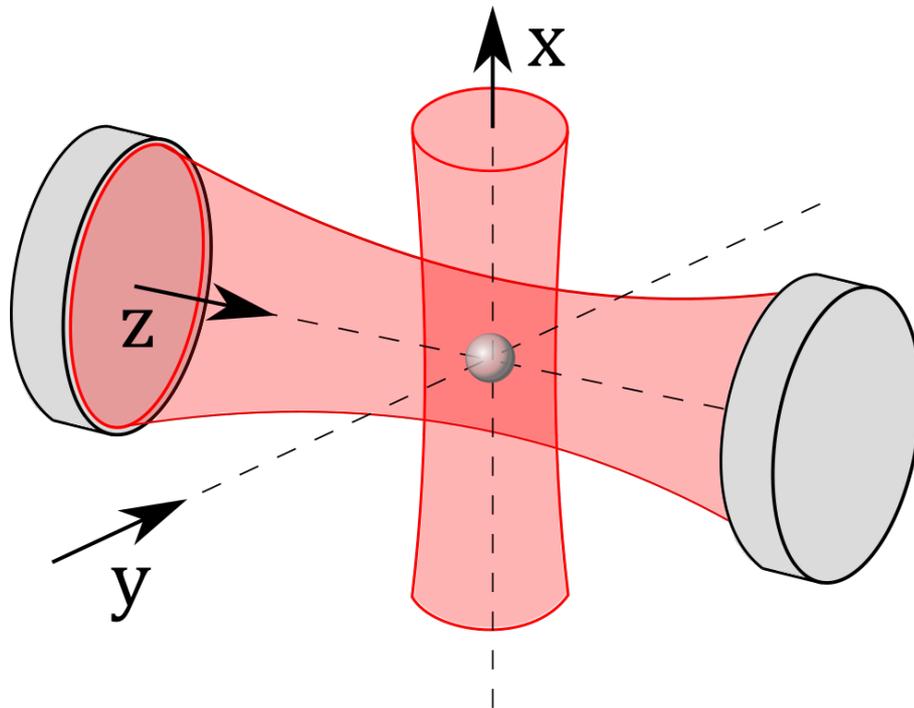
Figure 9: Reference scheme for cavity cooling. A Fabry-Pérot cavity with resonance frequency ω_C and waist w_0 is pumped by a laser with frequency ω_L, propagating along z. An additional pump beam along x with frequency ω_L crosses the cavity at its waist w_0. Reproduced and adapted from [67].

2.3.2 Cavity cooling

In this section we will establish the theory behind cavity cooling of nanoparticles. We will follow the derivation of [67] to obtain as generalized an interaction form as needed. Later we will alter these equations according to the cooling scheme presented. Figure 9 shows the basic setup idea, including the coordinate geometry that will be used throughout this chapter. To start, we assume a Fabry-Pérot cavity with resonance frequency ω_C and waist w_0, pumped by a laser with frequency ω_L, propagating along z. An additional pump beam along x, also with frequency ω_L, crosses the cavity at its waist w_0. Both beams are detuned from the cavity resonance by $\Delta = \omega_L - \omega_C$. While the theory in [67] is derived for a system of N particles, we will here restrict ourselves to the for us relevant special case of $N = 1$. We assume a spherical particle of radius R and polarizability α in the Rayleigh approximation with no internal resonances near the frequencies given.

Such a particle will be subject to dipole forces from the intracavity field $\mathcal{E}(t)$ as well as the orthogonal pumping beam $\mathcal{H}_{ext}(x(t))$. We further denote the cavity pumping field by $\mathcal{E}_{ext}$. The total optical force acting on the particle can be expressed by $F(x(t)) = -\nabla V_{opt}(x(t)) = \frac{\alpha}{4}\nabla|E_{tot}(x(t))|^2$, where $|E_{tot}(x(t))|$ is the total, time averaged electric field at the position of the particle $x(t)$. Since the dipole force is a

conservative force, the particle can only loose energy via transfer to the cavity field, which is then dissipated at the cavity decay rate κ.

For convenient handling we will define dimensionless field amplitudes, which we can interpret as the inverse fields per photon:

$$a(t) = \sqrt{\frac{2\varepsilon_0 V_m}{\hbar\omega_L}}\mathcal{E}(t) \tag{2.63}$$

$$\frac{\eta}{\kappa} = \sqrt{\frac{2\varepsilon_0 V_m}{\hbar\omega_L}}\mathcal{E}_{ext} \tag{2.64}$$

$$\frac{\zeta}{-U_0}h(x(t)) = \sqrt{\frac{2\varepsilon_0 V_m}{\hbar\omega_L}}\mathcal{H}_{ext}(x(t)) \tag{2.65}$$

where we have introduced several new parameters: The cavity mode volume $V_m = \pi w_0^2 L/4$, the cavity pumping rate η, the transverse pumping rate ζ and finally the coupling strength U_0:

$$U_0 = -\frac{\alpha\omega_L}{2\varepsilon_0 V_m}. \tag{2.66}$$

The time evolution of the intracavity field amplitude can now be expressed by

$$\dot{a}(t) = \underbrace{\left[i\left(\Delta - U_0|f(x(t))|^2\right) - \kappa\right]\cdot a(t)}_{(i)} + \underbrace{i\zeta h(x(t))f^*(x(t))}_{(ii)} + \underbrace{\eta}_{(iii)} \tag{2.67}$$

which consists of three terms: (i) the decay rate κ and the effective detuning $\Delta_{eff} = \Delta - U_0|f(x(t))|^2$ ($f(x(t))$ is the transverse mode function of the cavity) which includes the position dependent modification due to the particle's presence in the cavity field, (ii) coherent scattering from the pumping laser into the cavity mode and (iii) the cavity pumping rate. The equations of motion for a particle of mass m inside the field are given by two coupled differential equations:

$$\dot{x}(t) = v(t) \tag{2.68}$$

$$\dot{v}(t) = \underbrace{-\frac{|a(t)|^2 \hbar U_0}{m} \nabla |f(x(t))|^2}_{(1)} - \underbrace{\frac{\hbar \zeta^2}{U_0 m} \nabla |h(x(t))|^2}_{(2)}$$

$$+ \underbrace{\frac{\hbar \zeta}{m} \left[a(t) \nabla f(x(t)) h^*(x(t)) + a^*(t) \nabla f^*(x(t)) h(x(t)) \right]}_{(3)} \tag{2.69}$$

Equation 2.69 again consists of three terms which we can now attribute to a physical origin. Term (1) and (2) correspond to the dipole forces exerted upon the particle by the cavity field and the transverse pumping beam respectively. Therefore, (1) scales with the intracavity field like $|a(t)|^2$ and (2) with the pump rate ζ^2. Finally, term (3) accounts for the coupling between the dipoles induced by the two fields and thus depends on both $a(t)$ and ζ. We have now established a set of coupled differential equations for the motion of the particle and the intracavity light field, which can be solved numerically.

To conclude, we want to characterize the so-far abstract pumping rates ζ and η. We assume the transverse pumping beam to be a focused Gaussian beam with beam waist w_L and power P_L. We can then write

$$\zeta = U_0 \frac{w_0}{w_L} \sqrt{\frac{P_L}{2\hbar \omega_L \nu_{FSR}}} \tag{2.70}$$

$$\eta = \kappa \sqrt{\frac{2 P_C L}{\hbar \omega_L c}} \tag{2.71}$$

where $\nu_{FSR} = c/2L$ is the free spectral range of the cavity and $P_C = \frac{1}{4}\pi w_0^2 \varepsilon_0 c \mathcal{E}^2$ is the power of the cavity pumping beam.

2.3.2.1 Sisyphus cooling

The first cooling scheme presented only uses a strong cavity pumping beam but no external transverse pumping, i.e. we can set ζ and $h(x(t))$ to zero. This greatly simplifies our equations of motion 2.67, 2.68, 2.69. Let us first assume a cavity without particle in order to obtain a steady state solution. The time evolution of the intracavity field then simplifies to

$$\dot{a}(t) = (i\Delta - \kappa)a(t) + \eta \tag{2.72}$$

and in the steady state $\dot{a}(t) = 0$ has an amplitude

$$a_0 = \frac{\eta}{\kappa - i\Delta}. \tag{2.73}$$

For the interaction with a nanoparticle we have to account for the mode function of the cavity, which is given by:

$$|f(x, y, z)|^2 = \cos^2(kz) \cdot \exp\left(-2\frac{x^2 + y^2}{w_0^2}\right). \tag{2.74}$$

where $k = \omega_L/c$ is the wavenumber of the pumping beam. The motion of the particle along the standing light wave is subsequently given by

$$m\ddot{z}(t) = -2\hbar k U_0 |a(t)|^2 |f(x, y, z)|^2 \tan(kz). \tag{2.75}$$

We can qualitatively analyze the resulting force by considering only small fluctuations around the steady state $a_0 + \delta a, \delta a \ll a_0$. The formal solution is given by [68]

$$a(t) = -iU_0 a_0 \int_{-\infty}^{t} dt' \exp(-(\kappa - i\Delta)(t - t')) \cdot |f(x, y, z)|^2 \tag{2.76}$$

Near the cavity waist we can approximate the mode function to be a plane wave $f(z) = \cos(k(z - v(t - t')))$ that is subject to a time dependent Doppler shift kv induced by the nanoparticle motion. Equation 2.76 can then be evaluated to

$$a(t) = \frac{U_0 a_0}{4} \left(\frac{2}{\Delta + i\kappa} + \frac{e^{2ikz}}{(\Delta - 2kv) + i\kappa} + \frac{e^{-2ikz}}{(\Delta + 2kv) + i\kappa}\right). \tag{2.77}$$

We can now use this result to calculate the force acting on the particle. We find that the velocity dependent friction term $F_{\text{fric}} = \Gamma\dot{z}(t)$ of the total force reads [69]

$$F_{\text{fric}}(v) = 2\hbar k \frac{U_0^2 |a_0|^2 \kappa}{4} \frac{8kv\Delta}{[(\Delta + 2kv)^2 + \kappa^2][(\Delta - 2kv)^2 + \kappa^2]}. \tag{2.78}$$

We see that indeed the force can be interpreted as a Doppler friction force where a scattered photon reduces the particle's momentum by $2\hbar k$. A graphic evaluation of the friction force for different values of the detuning Δ can be seen in Figure 10. The strongest force is achieved for $\Delta = -\kappa/\sqrt{3}$. Around $v = 0$, i.e. for $|kv| \ll |\Delta|, \kappa$, the force scales approximately linear with the velocity of the particle. We can simplify and obtain the damping coefficient:

$$\Gamma = \frac{4\hbar k^2 U_0^2 |a_0|^2 \kappa\Delta}{(\Delta^2 + \kappa^2)^2}. \tag{2.79}$$
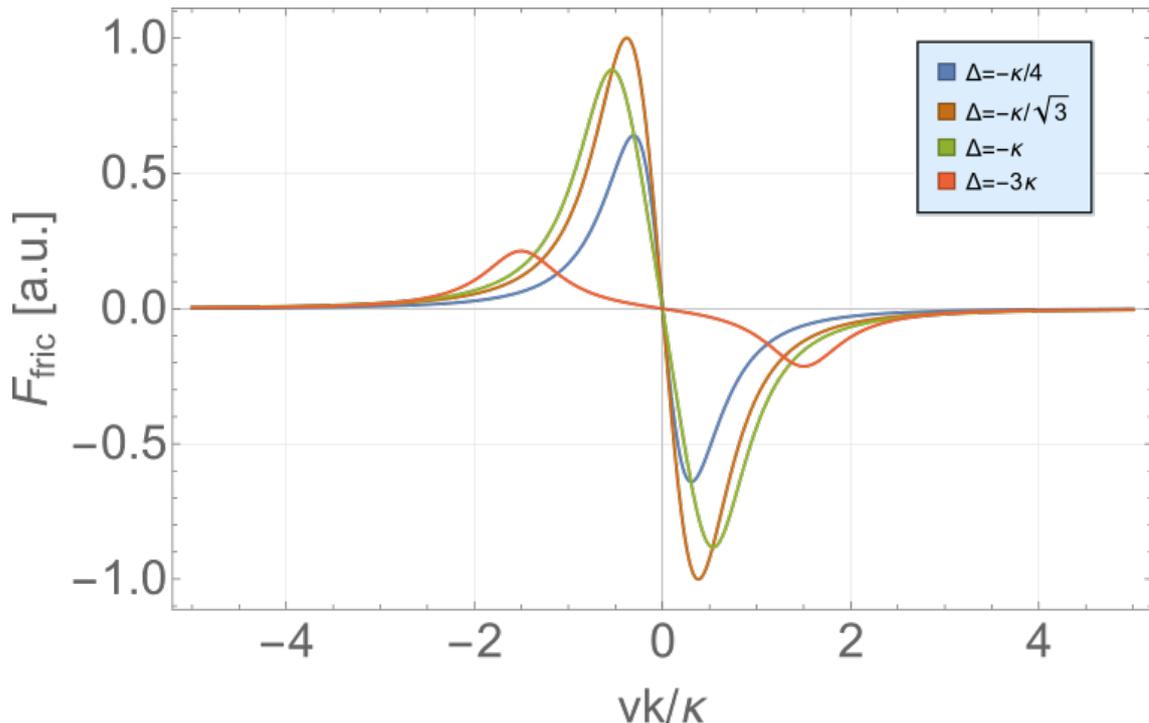
Figure 10: Cooling force for different values of the detuning Δ. The strongest force is achieved for $\Delta = -\kappa/\sqrt{3}$. Near $v = 0$ the force is linear and the damping constant can be approximated by equation 2.79. However, cooling only happens for a range of velocities defined by $|kv| \sim \Delta$.

However, the stronger the force, the more distinct is its peak and thus the narrower its full width at half maximum. We can estimate the range for cooling to happen for velocities $|kv| \sim \Delta$. Therefore, the capture range of velocities becomes very limited for strong forces. On the other hand, a broader capture range is accompanied by weaker cooling. This leads to the necessity of continuous modification of the detuning for fast particles.

To summarize, the intracavity intensity is modulated by the presence of the particle which shifts the effective detuning depending on its position. We can exploit this by red-detuning the pump beam with respect to the cavity resonance, i.e. $\Delta = \omega_L - \omega_C < 0$. Due to the increased optical path length caused by the particle's higher refractive index compared to vacuum, the cavity will be shifted towards resonance. This allows more light to build up inside the cavity. If the particle stays completely still, a steady state will attune after a time $1/\kappa$. On the other hand, if the particle moves along the cavity axis it will run over the standing light wave and induces a periodic modulation of the intracavity intensity. For $\Delta \simeq \kappa$ and $U_0 \simeq -\kappa$ [70], the particle invokes an optical potential that is always highest when it sits in an antinode, and lowest when it is in a node. Heuristically speaking, the particle self-modulates the optical potential in a way where it always has to climb a steeper hill

than it descends. The motional energy transferred from the particle to the cavity field is then dissipated at a rate $\kappa |a(t)|^2$. Due to this analogy, the cooling method is commonly referred to as *Sisyphus cooling*, named after the eternally punished king of Ephyra in Greek mythology.
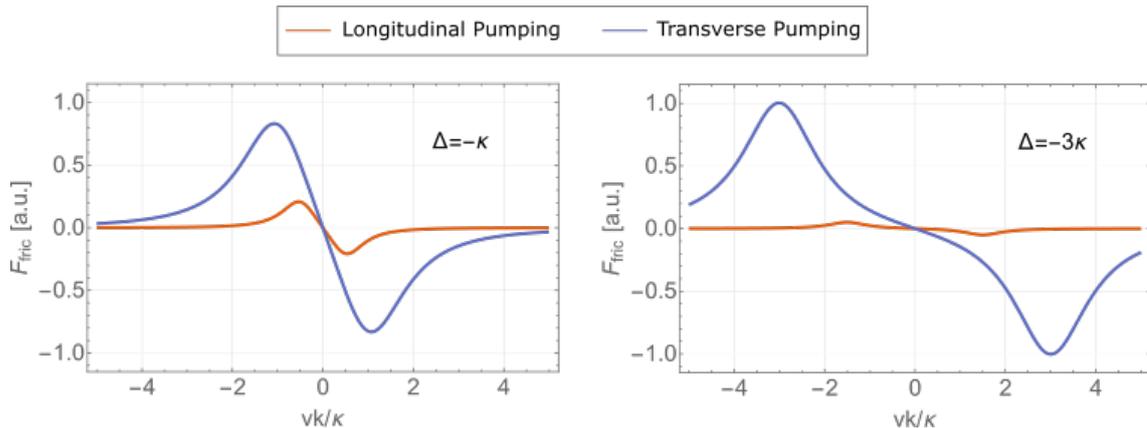
2.3.2.2   Coherent scattering cooling

We now turn to another cooling setup where the transverse pumping beam is switched on and the cavity pumping beam is switched off, i.e. $\eta = 0, \zeta \neq 0$. In this case equation 2.67 turns into

$$\dot{a}(t) = [i\Delta_{eff} - \kappa]\, a(t) + i\zeta h(x,y,z) f^*(x,y,z). \tag{2.80}$$

For simplicity reasons, we again assume a one dimensional mode function $f(z) = \cos(kz)$ and set the beam pump $h(x(t)) = 1$. The derivation then follows the steps from the previous chapter, therefore we will limit ourselves to state the friction force [69]

$$F_{\text{fric}}(v) = 4\hbar k \kappa \zeta^2 \frac{kv\Delta}{[(\Delta - kv)^2 + \kappa^2][(\Delta + kv)^2 + \kappa^2]}. \tag{2.81}$$

The particle scatters light velocity dependent into the cavity. For correctly chosen Δ the light is resonant with the cavity and can lead to a cooling force. So far, there is not much difference to before. But let us compare the two friction forces 2.78 and 2.81. For proper comparison we will choose the two pumping beams to be equally strong, i.e. $\zeta = \eta U_0 / \kappa$. This is visualized in Figure 11. Apart from obvious stronger forces, coherent scattering cooling also allows for cooling of particles with velocities $|kv| \ll \kappa$. The cooling peaks are broader, thus effectively increasing the range of particles that can be efficiently cooled. For higher detunings the maximum simply moves towards higher velocities, but the maximum force stays about the same. On the other hand, for cavity pumping the maximum friction force rapidly decreases for larger detuning.

Figure 11: Comparison of arising cooling forces between longitudinal laser pumping (orange curves) and pumping via coherent scattering from a transverse beam (blue curves) for different detunings Δ. Plotted is the force in arbitrary units vs. kv in units of κ. Coherent scattering cooling gives rise to higher forces, scales superior with Δ and has a broader effective cooling range. Reproduced from [69].

2.3.3 Cavity locking mechanisms

Since optical cavities are very frequency selective, over-time precision tuning between the laser frequency and the cavity length is necessary. This is called cavity locking. Cavities are prone to 'fall out of lock', i.e. parameters change such that the cavity is weakly populated or not driven at all. There are several contributing factors that have to be accounted for, happening on different time scales. We have to differentiate between fast fluctuations and long-term drifts. First, we have slow changes in cavity length or laser frequency due to variations in temperature or pressure. Secondly, there are the fast fluctuations, caused by e.g. acoustic disturbances.

In principle, there are two ways to stabilize a cavity. On the one hand, we can modulate the laser frequency to match the cavity resonance at any given time. Most lasers are frequency tunable and can be fed an electrical feedback signal. On the other hand, we can also alter the cavity resonance frequency, i.e. changing the cavity length, to match the laser output frequency. This is commonly done by attaching a piezoelectric element to one cavity mirror. Either way, we require a fast feedback loop with strong signal-to-noise ratio (SNR).

Side-of-fringe locking

The simplest way to implement cavity locking is to use the slope to either side of the cavity transmission signal. We assume a driving laser with frequency ω_L pumping a detuned cavity with resonance $\omega_C = \omega_L + \Delta$ and linewidth κ. The transmitted laser power depends on the detuning Δ and is modified by the cavity transfer function
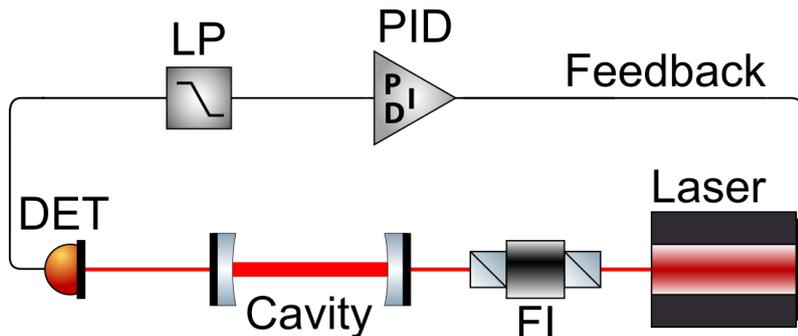
Figure 12: Basic side-of-fringe locking setup. A photodiode (DET) detects the power transmitted through the cavity. Any change in relative frequency between laser and cavity resonance results in a proportional change in transmitted power. The signal is low-pass filtered (LP) and fed back to the laser to modify its output frequency. PID is the proportional-integral-derivative (PID) controller that employs the feedback and FI is a Faraday isolator to avoid back-reflexes into the laser.

[64]

$$T(\Delta) = \frac{(\kappa/2)^2}{(\kappa/2)^2 + \Delta^2}. \tag{2.82}$$

Small changes in relative frequency between laser and cavity resonance result in a proportional change in transmitted power. Therefore, side-of-fringe locking converts frequency fluctuations $\Delta\omega$ into relative intensity fluctuations $\Delta I/I$. The error signal can then be fed back to the laser or used to drive a piezo element (Figure 12).

However, this technique can only lock off-resonance, as the signal is symmetric about resonance, thus the name *side-of-fringe*. If the locking point were exactly on resonance, the intensity would decrease to either side of the signal and there would be no telling whether to increase or decrease the frequency [71].
Another drawback to this scheme lies in the fact that it is unable to distinguish between intensity change caused by frequency fluctuations and actual intensity fluctuations of the laser itself. Moreover, the error signal strongly depends on the locking point Δ_0 (Figure 13), therefore making this scheme unfavorable if the set point changes regularly. For side-of-fringe locking, this implies re-optimization of the lock parameters. This scheme is also not very well suited for high-finesse cavities, since they have a small linewidth. Due to the steepness of the fringe the cavity falls easily out of lock.
Furthermore, since any frequency fluctuations result in intracavity power fluctuations, this technique fundamentally implies a heating source for any particle trapped in the cavity, thus setting a limit for cavity cooling.
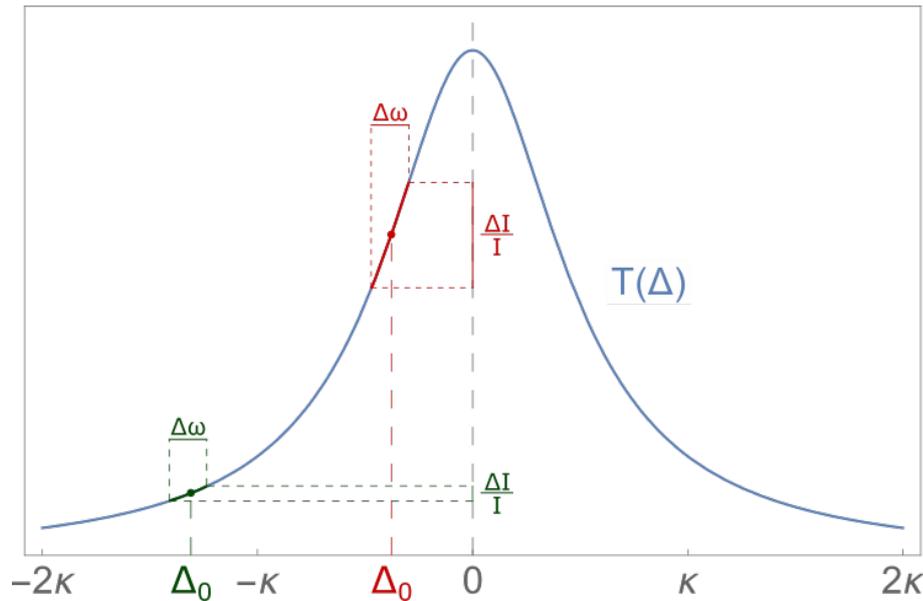
Figure 13: Side-of-fringe locking converts frequency fluctuations $\Delta\omega$ into relative intensity fluctuations $\Delta I/I$. The error signal strongly depends on the locking point Δ_0. Equal frequency variation will result in different intensity changes depending on the locking point in frequency space (red vs green). Reproduced and adapted from [64].

Pound-Drever-Hall locking

If we want to lock 'on top' of a resonance, we need the derivative of the input signal. This leads to an anti-symmetric error signal with a zero crossing at the resonance frequency. This is generally obtained by introducing a modulation to the laser frequency and multiplying the detection signal with the modulation input. For small modulations of the laser frequency, this is called *top-of-fringe locking*. A more elaborate scheme is provided by Pound-Drever-Hall (PDH) locking [72], which uses much higher modulation frequencies.

For PDH locking we drive the cavity with resonance frequency ω_C with a laser at frequency ω_L (carrier), plus two weak sidebands at frequencies $\omega_L \pm \omega_S \gg \kappa$. Since the sidebands are far detuned from any cavity resonance, they are fully reflected at the mirror surfaces and acquire a phase shift $\pm\pi/2$. The central frequency of the laser ω_L, however, is only partially reflected and acquires a phase φ_r that is proportional to the detuning $\Delta = \omega_L - \omega_C$. We can then mix this reflected signal with the reflected sidebands and thus detect any drift in Δ as a change in the relative phase between carrier and sideband frequencies $\pi/2 - \varphi_r$ [64].

Let us now take a deeper look at the error signal obtained for PDH locking. The electric field of the laser output can be written as $E_i = E_0\, e^{i\omega_L t}$, where $E_0 \in \mathbb{C}$ is the complex amplitude. Upon reflection at the cavity, the electric field takes the form
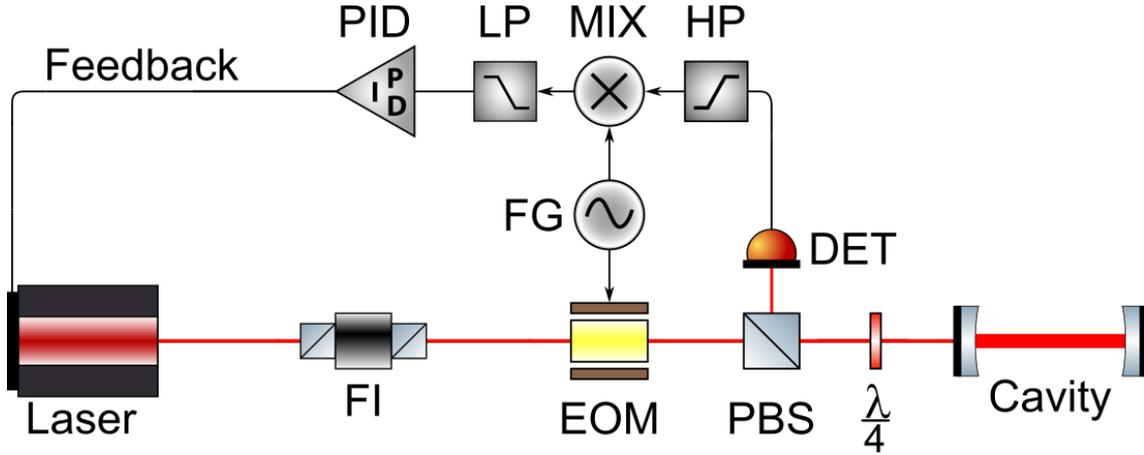
Figure 14: Basic Pound-Drever-Hall (PDH) locking setup. A frequency generator (FG) generates two synchronized drive tones. The first is used to drive an electro-optical modulator (EOM) to create two sidebands on the laser carrier. An optical isolator, consisting of a quarter-wave plate ($\lambda/4$) and a polarizing beamsplitter (PBS), picks off the reflected beam and send into a photodiode (DET). The signal is then mixed (MIX) with the second FG drive, identical in frequency, but phase-shifted, to create an error signal. A low-pass filter (LP) isolates the low frequency signal that contains the derivative of the reflected intensity. This error signal is then fed back to the laser via a PID controller to lock its frequency to the cavity resonance. HP...high-pass filter, FI...Faraday isolator. Reproduced and adapted from [64].

$E_r = F(\Delta) \cdot E_i$, where

$$F(\Delta) = \frac{r \cdot \left(e^{i\frac{\Delta}{\Delta\nu_{FSR}}} - 1 \right)}{1 - r^2 e^{i\frac{\Delta}{\Delta\nu_{FSR}}}}, \tag{2.83}$$

is the cavity reflection funciton. We have assumed a symmetric cavity of length L, with free spectral range $\Delta\nu_{FSR} = c/2L$ and equal mirror reflectivity r. Due to the limited reflectivity of the mirrors, there will always leak some light out of the cavity. Therefore, the detected 'reflected' light actually consists of two beams: the promptly reflected and the leakage beam. Near resonance these two beams have almost identical wavelength and intensity. Now, if the laser frequency coincides perfectly with the cavity resonance, i.e. $\Delta = 0$, the two beams are exactly 180° out of phase. They interfere deconstructively and the reflected beam vanishes. If $\Delta \neq 0$, they will still be out of phase but not by exactly 180°. Therefore, some light will be reflected off the mirror surface and its phase is a measure for the detuning Δ. This is where the sidebands come into play. Superimposing the sidebands with the reflected light creates a beatnote with frequency ω_S, which we can detect with a photodiode. From the phase of this pattern we can conclude the phase of the reflected light which in turn tells us to which side of the resonance frequency the carrier is detuned [71].

The sidebands are created from phase modulation of the carrier, e.g. by an electro-optic modulator (EOM) or a Pockels cell. After phase modulation, the electric field of the beam can be described by [71]

$$
\begin{aligned}
E_i &= E_0 \, e^{i(\omega_L + \beta sin(\omega_S)t)} \\
&\approx E_0 \left[J_0(\beta) + 2iJ_1(\beta)\sin(\omega_S t) \right] e^{i\omega_L t} \\
&= E_0 \left[J_0(\beta) \, e^{i\omega_L t} + J_1(\beta) \, e^{i(\omega_L+\omega_S)t} - J_1(\beta) \, e^{i(\omega_L-\omega_S)t} \right],
\end{aligned}
\tag{2.84}
$$

where β is the modulation depth and J_0 and J_1 are Bessel functions[3]. From the last line of equation 2.84 we can see that indeed there are three beams contributing to the field, the carrier with frequency ω_L and the two sidebands at $\omega_L \pm \omega_S$. The electric field of the reflected beam is then given by

$$
E_r = E_0 \left[F(\Delta)J_0(\beta) \, e^{i\omega_L t} + F(\Delta+\omega_S)J_1(\beta) \, e^{i(\omega_L+\omega_S)t} - F(\Delta-\omega_S)J_1(\beta) \, e^{i(\omega_L-\omega_S)t} \right].
\tag{2.85}
$$

If we introduce the carrier power $P_c = |E_0|^2 J_0^2(\beta)$ and the first-order sideband power $P_s = |E_0|^2 J_1^2(\beta)$, then the total power $P_r = |E_r|^2$ in the reflected beam is

$$
\begin{aligned}
P_r &= P_c|F(\Delta)|^2 + P_s \left(|F(\Delta+\omega_S)|^2 + |F(\Delta-\omega_S)|^2 \right) \\
&\quad + 2\sqrt{P_c P_s} Re \left\{ F(\Delta)F^*(\Delta+\omega_S) - F^*(\Delta)F(\Delta-\omega_S) \right\} \cos(\omega_S t) \\
&\quad - 2\sqrt{P_c P_s} Im \left\{ F(\Delta)F^*(\Delta+\omega_S) - F^*(\Delta)F(\Delta-\omega_S) \right\} \sin(\omega_S t) \\
&\quad + (2\omega_S \text{ terms}).
\end{aligned}
\tag{2.86}
$$

The first line in equation 2.86 is minimal for $\Delta = 0$, i.e. perfect resonance, and corresponds to the reflected optical power of the carrier plus the sidebands. Line two and three are terms that oscillate at at the modulation frequency ω_S. This is the beat pattern that samples the reflected phase. This signal is then modulated by a local oscillator $\propto \cos(\omega_S t + \Theta)$ which gives us our error signal [64]:

$$
\frac{\mathrm{Err}(\Delta)}{\sqrt{P_c P_s}} = -Re \left\{ \chi(\Delta,\omega_S) \right\} \cos \varphi_s - Im \left\{ \chi(\Delta,\omega_S) \right\} \sin \varphi_s
\tag{2.87}
$$

---

[3]We have ignored oscillations at the second harmonic $2\omega_S$ as their modulation depth is negligible for $\beta < 1$.
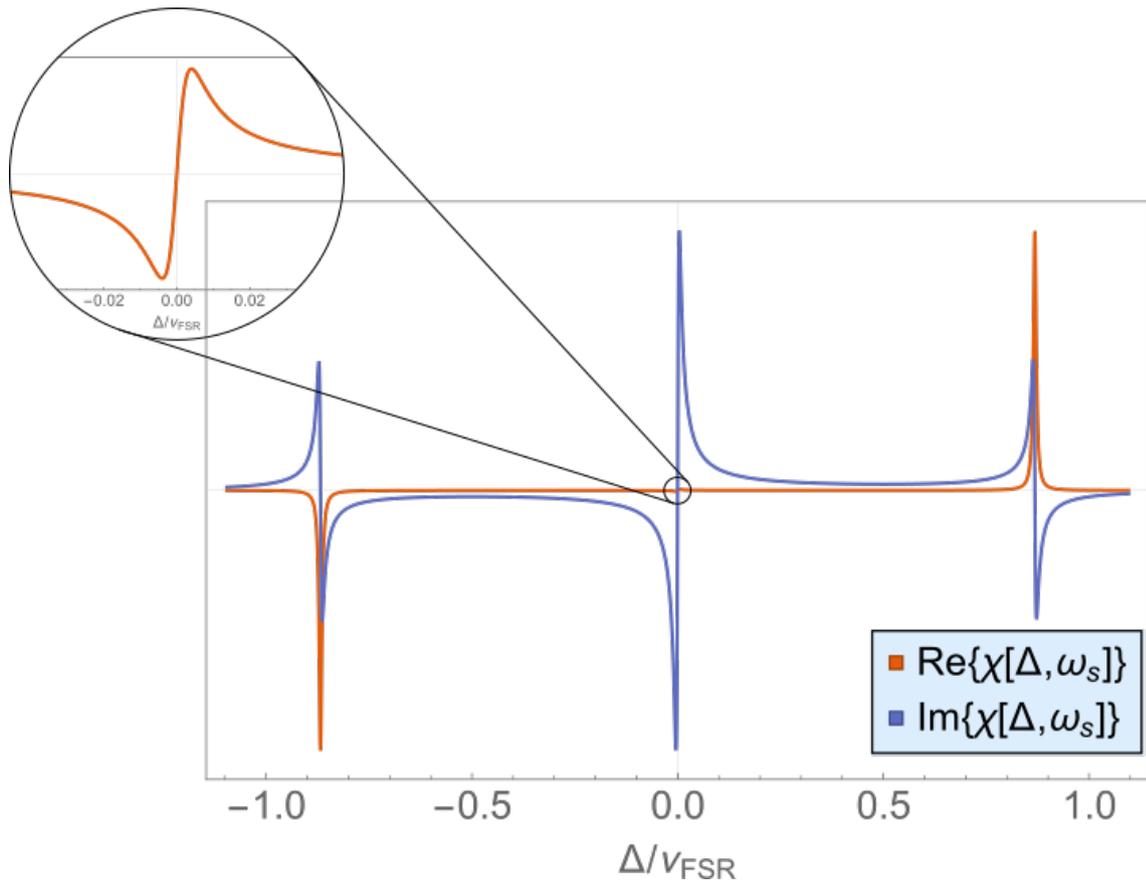
Figure 15: Pound-Drever-Hall error signals. The signal depends on the relative phase φ_s between the beatnote and the local oscillator. The strongest dependence on the the laser frequency ω_L is obtained for $\varphi_s = \pi/2$, where the response is out of phase (blue curve). The in-phase (red curve) component of the error signal is obtained for $\varphi_s = 0$. The black circle shows a detailed version of this error signal around zero crossing. However, due to the large discrepancy in signal strength, the in-phase component is generally not used for locking.

where φ_s is the relative phase between the beatnote and the demodulation signal, $\chi(\Delta, \omega_S) = F(\Delta)F^*(\Delta + \omega_S) - F^*(\Delta)F(\Delta - \omega_S)$. The in-phase ($\varphi_s = 0$) and out-of-phase ($\varphi_s = \pi/2$) components of the error signal are the real and imaginary part of $\chi(\Delta, \omega_S)$. A plot of the two components can be seen in Figure 15. From this it becomes clear, that the in-phase term is only a viable error signal for small modulations, as its zero crossing is small compared to the out-of-phase component. For locking, the imaginary part of $\chi(\Delta, \omega_S)$ poses a much better option. The set point is chosen such that $\omega_L = \omega_C$ and the error function is ultimately given by [64]:

$$\text{Err}(\Delta) = -4\sqrt{P_c P_s} \frac{\Delta}{\Delta\nu_{FSR}(1 - r^2)}, \qquad \Delta \ll \kappa. \qquad (2.88)$$
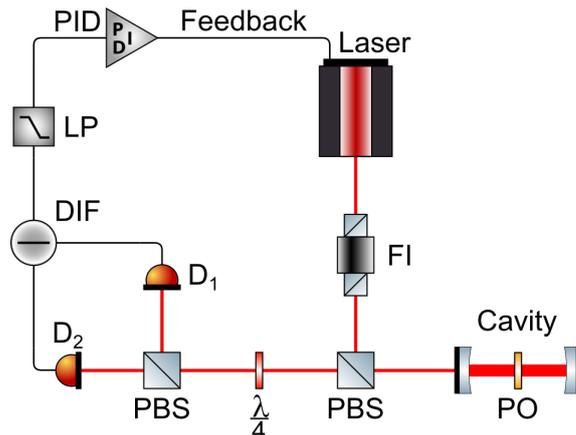
Hänsch-Couillaud locking

Finally, we will quickly discuss a method that relies on a linear polarizer inside the cavity to create an error signal, as first reported by Theodor Hänsch and Bernard Couillaud in 1980 [73]. We will follow the steps of their initial proposal to discuss this locking mechanism. An analogue to PDH locking is given as this scheme too monitors an out-of-phase component of the light reflected by the cavity. However, for Hänsch-Couillard (HC) locking, this manifests in the occurrence of elliptical polarization.

We assume linearly polarized light, emitted by a laser at frequency ω_L, impinging on a cavity with resonance frequency ω_C. Inside the cavity we place a linear polarizer such that its transmission axis forms an angle Θ with the polarization axis of the incoming beam. A schematic of an example setup can be seen in Figure 16. The incident light field can be separated into two orthogonal linearly polarized components: one where the electric field vector is parallel to the transmission axis of the linear polarizer and one where it is perpendicular. The electric field of the two components is given by

$$E^{(i)}_{\parallel} = E^{(i)} \cos\Theta, \qquad\qquad E^{(i)}_{\perp} = E^{(i)} \sin\Theta, \qquad (2.89)$$

where $E^{(i)} = E_0\, e^{i\omega_L t}$ is the complex field of the incident beam. The parallel component corresponds to to the beam used in PDH locking. Depending on the detuning $\Delta = \omega_L - \omega_C$ it partially couples into the cavity and is partially reflected at the surface. Upon reflection it acquires a phase shift proportional to Δ. We can therefore write

Figure 16: Schematic setup for Hänsch-Couillaud locking. Linearly polarized laser light impinges on a cavity that has a linear polarizer (PO) inside. The transmission axis of the polarizer forms an angle Θ with the polarization axis of the beam. The parallel component of the incoming electric field acquires a phase shift proportional to the detuning Δ. For non-zero detuning this results in elliptical polarization of the total reflected beam. A quarter-wave plate ($\lambda/4$) and a polarizing beam splitter (PBS) separate the beam in two orthogonal linearly polarized beams whose intensities are individually detected by two photodiodes D_1 and D_2. A subtractor takes the difference of the two intensities and creates an error signal that is fed back to the laser. LP...low-pass filter, PID...PID controller, FI...Faraday isolator.

$$E_{\parallel}^{(r)} = E_{\parallel}^{(i)} \cdot \left(\frac{r \cdot \left(e^{i\frac{\Delta}{\Delta\nu_{FSR}}} - 1 \right)}{1 - r^2 e^{i\frac{\Delta}{\Delta\nu_{FSR}}}} \right), \tag{2.90}$$

where again we have assumed a symmetric cavity of length L, with free spectral range $\Delta\nu_{FSR} = c/2L$ and equal mirror reflectivity r. The orthogonal part, on the other hand, is simply reflected at the cavity surface

$$E_{\perp}^{(r)} = E_{\perp}^{(i)} \cdot r. \tag{2.91}$$

and serves as the reference beam. For a non-zero detuning the parallel component acquires a phase shift with respect to the perpendicular component. Thus the reflected beam will be elliptically polarized. The handedness of the polarization is a measure for the sign of the detuning.

The detection arm of the setup consists of the following: the reflected light first goes through a quarter-wave plate ($\lambda/4$) and then impinges on a polarizing beam splitter (PBS). The $\lambda/4$ plate is rotated such that its fast axis forms an angle of 45° with the polarization axis of one of the PBS outputs. To better understand the effect of the quarter-wave plate we decompose the elliptically polarized light into two counterrotating circularly polarized components. Now the $\lambda/4$ plate transforms the circularly polarized parts into orthogonal linearly polarized beams. These are
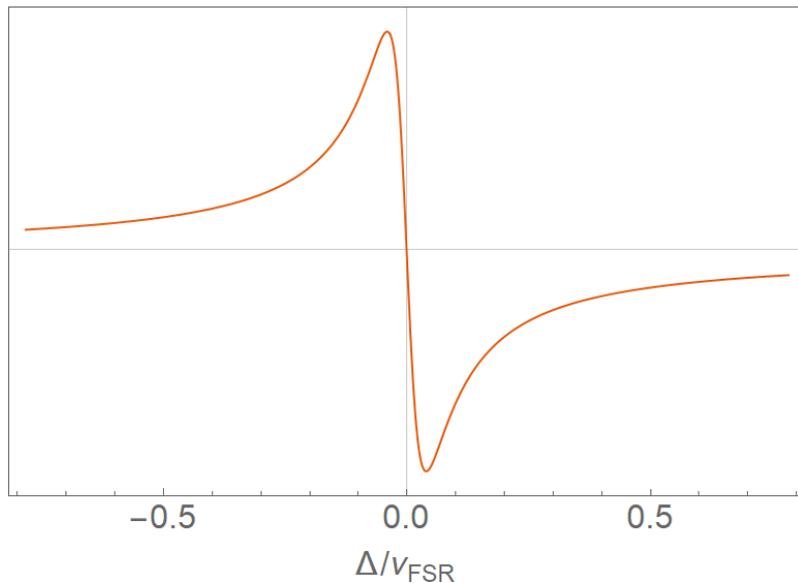
Figure 17: Error signal $I_a - I_b$ for Hänsch-Couillaud locking. The signal is maximized for $\Theta = \pi/4$. For $\Delta = 0$ the function has a zero crossing, thus providing the possibility to lock on cavity resonance.

separated by the PBS and their intensities are individually detected by two photodiodes.

The error signal is then obtained by subtraction of the two intensities. For convenient calculation of the intensities we assume rotation of the $\lambda/4$ plate such that its fast axis is parallel to the polarization axis of the intracavity polarizer. The detected intensities are of the form

$$I_{a,b} = \frac{1}{4}c\varepsilon_0 \left| \left(E_\parallel^{(r)} \pm iE_\perp^{(r)} \right) \right|^2. \tag{2.92}$$

Combining equations 2.89 and 2.92 we find our error function

$$\mathrm{Err}(\Delta) = I_a - I_b = \frac{I^{(i)}}{2(1-r^2)} \sin(2\Theta) \cot \left(\frac{\Delta}{2\nu_{FSR}} \right). \tag{2.93}$$

A plot of the error function can be seen in Figure 17. The amplitude of the signal is maximized for $\Theta = \pi/4$, and $\sin(2\Theta) = 1$. However, it can be useful to use smaller Θ to achieve a better signal-to-noise ratio (SNR) if laser fluctuations are the dominant noise source. For $\Delta = 0$ the function has a zero crossing and the signal can be used to lock at $\omega_L = \omega_C$.

41
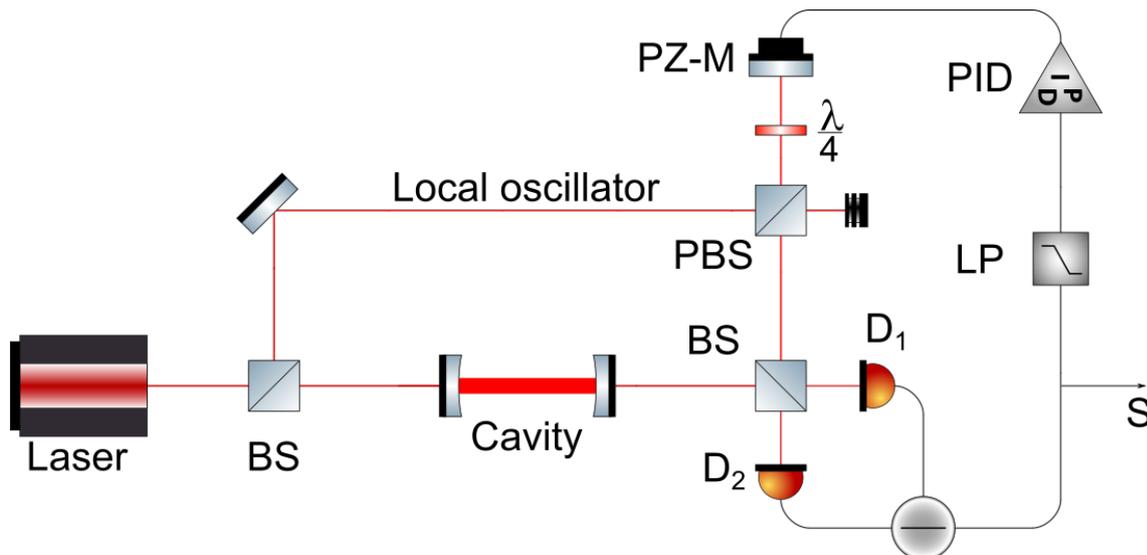
Figure 18: Example setup for homodyne detection. Part of the laser output is split off with a beam splitter (BS) and used as a local oscillator, the other part goes to the cavity. The local oscillator is phase shifted via a piezo-controlled mirror (PZ-M). A quarter-wave plate ($\lambda/4$) and a polarizing beam splitter (PBS) ensure that the beam is superimposed with the cavity transmission (other configurations use the back-reflex of the cavity). After a $50 : 50$ beam splitter two photodiodes D_1 and D_2 detect the transmitted and reflected parts of the BS. A subtractor calculates a difference signal between the two photodiodes. Part of this signal is sent back to the piezo-mirror in a feedback loop (low-pass filter LP and PID lock), the other part (S) is sent to the readout device of choice.

2.3.4   Nanoparticle Detection

Homodyne and heterodyne detection

A similar idea as in Pound-Drever-hall locking can be implemented to detect the position of a nanoparticle inside the cavity. Phase and amplitude of the cavity mode contain information about the motion of the particle, so we have to extract one or both of these quantities. Homodyne and heterodyne detection are two closely related ideas to achieve just that. The measurements are an amplified detection for the phase and amplitude quadrature. Depending on the phase difference between signal and reference beam, one or both quantities can be measured. However, measuring both amplitude and phase quadrature comes at the trade off of reduced sensitivity in both [64]. Commonly, the signal beam is either the light transmitted through or reflected off the cavity.

In both detection schemes the cavity transmission (or reflection) is superimposed with a strong local oscillator (LO). In homodyne detection the local oscillator frequency equals the laser frequency, whereas in heterodyne measurement the two frequencies differ. Example setups can for the two methods can be seen in Figures
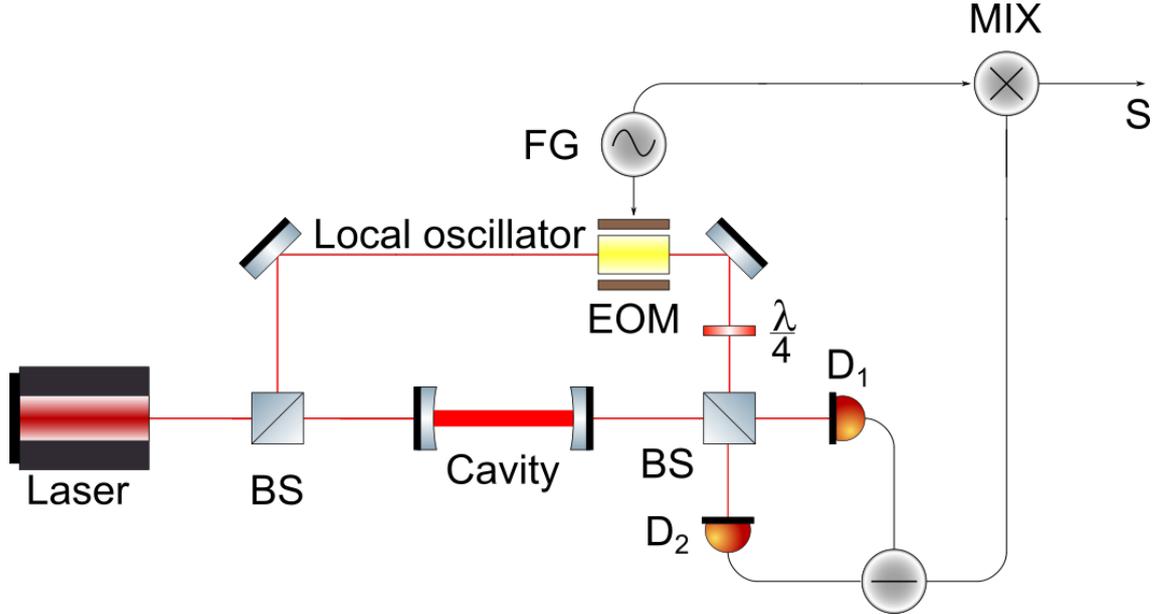
Figure 19: Example setup for heterodyne detection. Here the local oscillator beam is frequency shifted by a frequency generator (FG) driven electro-optical modulator (EOM). Similar to homodyne detection a quarter-wave plate ($\lambda/4$) and a BS superimpose the cavity transmission with the local oscillator which are subsequently detected by two photodiodes D_1 and D_2. The difference signal is then mixed (MIX) with a second drive tone of the FG and the total signal (S) kann be read out.

18 (homodyne) and 19 (heterodyne). In either way, the two beams are brought to interference and are detected. It is common practice to use a balanced photodetection method instead of a single detector in order to get rid of excess noise of the local oscillator that would otherwise affect the signal.

The electric field of a wave satisfying the wave equation can be described by two quadrature amplitudes $X1$ and $X2$ [74]:

$$E(r,t) = E_0 \left[X1(r,t) \cos\left(\omega t\right) + X2(r,t) \sin\left(\omega t\right) \right]. \tag{2.94}$$

$X1$ and $X2$ can be expressed in terms of the real and imaginary part of the complex amplitude $\alpha(r,t)$:

$$X1(r,t) = \alpha(r,t) + \alpha^*(r,t) \tag{2.95}$$

$$X2(r,t) = -i\left[\alpha(r,t) - \alpha^*(r,t)\right]. \tag{2.96}$$

Fluctuations in amplitude and phase of the wave correspond to fluctuations in the quadratures, $\delta X1$ and $\delta X2$. The time-dependent complex amplitude of the wave can then be expressed as

$$\alpha(t) = \alpha + \delta X1 + i\delta X2. \tag{2.97}$$

In the regime of small fluctuations, i.e. $\alpha \gg \delta X_{1,2}(t)$, $\delta X1$ and $\delta X2$ describe the changes in amplitude and phase and are called the amplitude and phase quadratures, respectively.

We can now use equation 2.97 to time-dependently describe the complex amplitudes α_C and α_{LO} [75]:

$$\alpha_C(t) = \alpha_C + \delta X1_C(t) + i\delta X2_C(t) \tag{2.98}$$

$$\alpha_{LO}(t) = [\alpha_{LO} + \delta X1_{LO}(t) + i\delta X2_{LO}]\, e^{i\Phi_{LO}} \tag{2.99}$$

where $e^{i\Phi_{LO}}$ accounts for the relative phase difference between the two amplitudes. This phase difference is generally obtained by changing the path length of the oscillator arm via a piezo-controlled mirror (see Figures 18 and 19). We assume $\alpha \gg \delta X1$, i.e. the waves fluctuate only little around α. Furthermore, we assume a strong local oscillator signal $\alpha_{LO}^2 \gg \alpha_C^2$. The intensities detected by the two photodiodes are described by

$$|\alpha_{D1,2}|^2 = \left|\sqrt{1/2}\,[\alpha_{LO}(t) \pm \alpha_C(t)]\right|$$

$$= 1/2\left[|\alpha_{LO}(t)|^2 \pm \alpha_{LO}(t)\alpha_C^*(t) \pm \alpha_C(t)\alpha_{LO}^*(t) + |\alpha_C(t)|^2\right]$$

$$\approx 1/2\left[|\alpha_{LO}|^2 + 2\alpha_{LO}\delta X1_{LO}(t) \pm 2\alpha_{LO}\left(\delta X1_C(t)\cos\Phi_{LO} + i\delta X2_C(t)\sin\Phi_{LO}\right)\right] \tag{2.100}$$

In the last line we have neglected cross terms $\alpha_{LO}\alpha_C^*$ and $\alpha_C\alpha_{LO}^*$ compared to $|\alpha_{LO}|^2$, $\alpha_C\delta X$ and conjugates compared to $\alpha_{LO}\delta X$ and conjugates and any terms $\mathcal{O}(\delta X^2)$. The difference of the two detector intensities is then given by

$$I_-(t) \approx 2\alpha_{LO}\left(\delta X1_C(t)\cos\Phi_{LO} + i\delta X2_C(t)\sin\Phi_{LO}\right). \tag{2.101}$$

And indeed local oscillator fluctuations are completely suppressed. However, we can detect the phase and amplitude quadratures of the cavity light field, precisely what we were looking for. Moreover, the result is amplified, as the intensity scales with the amplitude of the local oscillator. Note that depending on the choice of phase difference Φ_{LO}, either one of the quadratures can be suppressed, resulting in

higher sensitivity for the other.

Heterodyne detection follows the same principle. We simply change the local oscillator from a beam with the same frequency as the laser beam, to one with a different frequency $\omega_{LO} = \omega_L + \omega_H$. As long as ω_H is within the detection range of the photodetector, the resulting detection signal will be a beat note at frequency ω_H.

Scattered light detection

Another method to extract information about the particle's motion is by means of the the light scattered off the particle. A particle inside the cavity scatters a portion of the light into free space. The scattered light field depends on the intracavity intensity $|a(t)|^2$ as well as the coupling of the particle's motion to the light field $|u(\vec{r},t)|^2$. By additionally measuring the field transmitted through the cavity we can extract the coupling

$$|u(\vec{r},t)|^2 = \cos^2(kz(t)) \cdot \exp\left(-2\frac{x^2(t) + y^2(t)}{w_0^2}\right), \qquad (2.102)$$

where w_0 is the waist and $k = 2\pi/\lambda$. However, by just looking at the coupling, there is no knowing of where the particle is located in cavity with respect to z as this motion induces a periodic modulation of the signal. This problem can be circumvented by pumping of an additional mode. The higher order mode has a slightly different k-value which results in a z-dependent relative phase difference to the fundamental mode. Otherwise, we have to assume that the particle enters the cavity at $z = 0$. The quality of this approximation can be increased by placing the detection fiber close to the waist.

We now assume that particles are launched by some mechanism (see chapter 3) and enter the cavity field with a forward velocity along x, i.e. $|v_x| \gg |v_y|$. The normalized scattering signal in direction orthogonal to both the cavity axis as well as the polarization direction, is then given by [76]

$$S_N(t) = \cos^2(kz(t)) \cdot \exp\left(-2\frac{x^2(t)}{w_0^2}\right). \qquad (2.103)$$

First, let's assume a fast particle. i.e. the kinetic energy along x and z is much greater than the optical potential. The particle will then be hardly affected by the cavity and we can assume constant velocities v_x and v_z for the transition through the cavity field. A signal for such a case can be seen in Figure 20. From the temporal $1/e^2$ width t_x of the Gaussian envelope we can extract the forward velocity $v_x = w_0/t_x$ for a given beam waist w_0. The modulation of the Gaussian is attributed
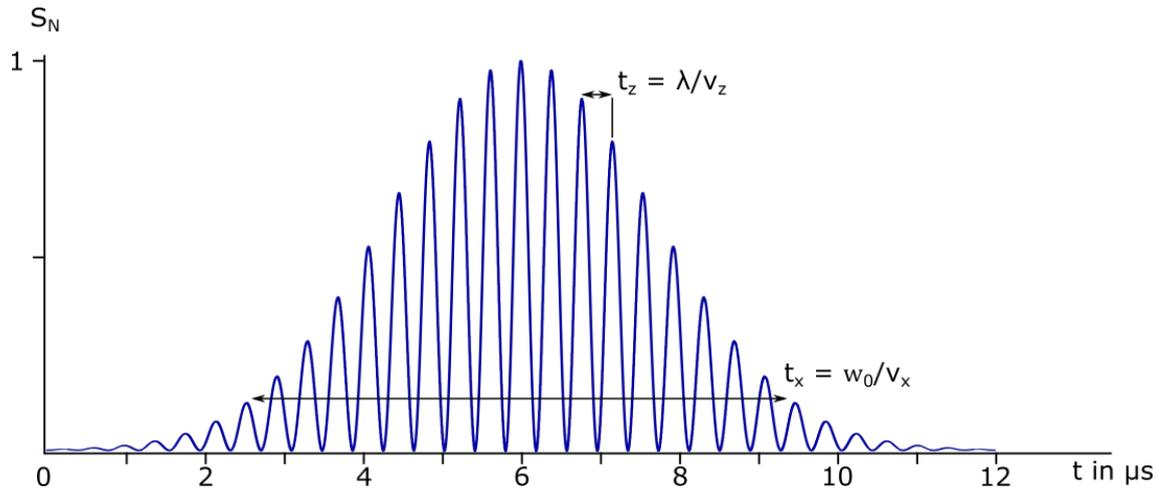
Figure 20: Simulated normalized scattering signal for a particle with high kinetic energy traversing a cavity with waist $w_0 = 60\,\mu m$ pumped by a laser with wavelength $\lambda = 1550\,\mathrm{nm}$. The $1/\mathrm{e}^2$ width t_x of the Gaussian envelope gives a forward velocity of $v_x = 25\,\mathrm{m/s}$. The modulation of the Gaussian is caused by the particle's motion along z as it runs over the standing wave. From the time it takes the particle to travel one wavelength ($2t_z$) we determine an axial velocity of $v_z = 2\,\mathrm{m/s}$.

to the transverse motion of the particle along z as it runs along the standing light wave. We can therefore obtain the velocity along z via $v_z = \lambda/2t_z$, where $2t_z$ is the time it takes the particle to travel one wavelength.

For particles with small kinetic energies the velocity changes while interacting with the cavity light field. An exemplary signal can be seen in Figure 21. Due to the slower forward velocity of $v_x = 3\,\mathrm{m/s}$ the particle has more time to interact with the cavity field. While it still freely traverses the cavity, its transversal motion is cooled. This is indicated by an asymmetric modulation of the Gaussian envelope, as it takes the particle longer to run over the standing wave at lower transversal velocity. At some point towards the cavity center, where the trap depth increases, the particle's kinetic energy is low enough to be trapped in one dimension. Oscillation around the anti-node can be seen as local non-zero minima of the sinusoidal modulation. These minima can be interpreted as the turning points of the oscillation. The extended minimum just before that corresponds to the last free transit through a node where the particle has barely enough energy to escape. Once the particle is far enough from the cavity center where the trap depth is lower than the kinetic energy, the particle can again freely run over the standing wave.

46
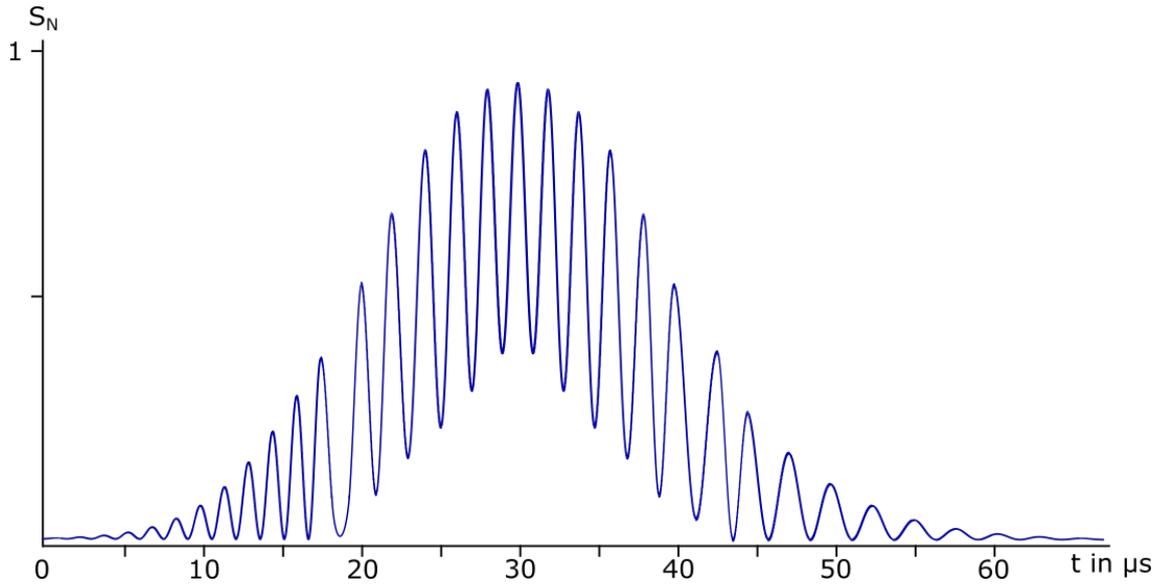
Figure 21: Simulated normalized scattering signal for a particle with low kinetic energy traversing the same cavity as before. From the Gaussian envelope we determine a forward velocity of $v_x = 3\,\mathrm{m/s}$. When entering the cavity the particle has a transverse velocity $v_z = 0.5\,\mathrm{m/s}$. Due to the longer interaction time the particle is now cooled by the cavity. This is indicated by the asymmetry of the modulation of the Gaussian envelope. We determine an exit velocity of $v_z = 0.3\,\mathrm{m/s}$, which implies a velocity reduction of ~ 1.7. Stronger cooling would result in a more distinct asymmetry. At first, the particle freely runs over the standing wave. After approximately $20\,\mu s$ the particle is trapped in one dimension and oscillates about the anti-node. In this case the scattered intensity does not drop to zero anymore. The last free transit through a node corresponds to the extended local minimum, as the particle has just enough kinetic energy to 'escape'.
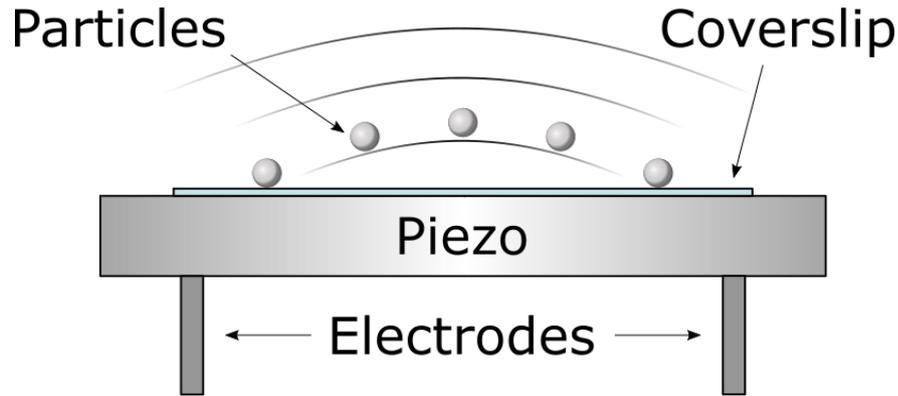
3 Loading mechanisms for levitated optomechanics

Successfully loading a particle into the trap is the first step in any levitated optomechanics experiment. And even though it is such a crucial part, almost 50 years after Arthur Ashkin's pioneering experiments [8], it is still surprisingly challenging to controllably do so.

There are several reasons as to why. For one, the trap volume is generally very small. Assuming a Gaussian beam profile, the trap depth falls off exponentially radially as well as axially. For tightly focused optical tweezers the focal volume is on the order of λ^3 (tweezers wavelength λ), a particle entering the light field at a distance larger than $\sim \lambda$ away from the trap center can therefore not be captured [56]. Optical cavities are more forgiving, here the defining factor is the mode volume $V_m = \pi w_0^2 L/4$, where w_0 is the minimal beam waist and L is the length of the cavity. While particles can be captured in anti-nodes away from the position of the waist [77], it gets exponentially harder the further off.

Properly controlling the velocity of the particles poses another difficulty. Due to the conservative nature of the dipole force, a particle will simply traverse the optical trap if no external forces are present. Furthermore, if the sum of the kinetic and potential energies of the particle is greater than the optical potential of the trap, the particle will also pass through the light field.
Both problems can be circumvented by exploiting the frictional damping of the surrounding medium to slow down the particle, both before and inside the cavity or tweezers. However, for frictional damping to be sufficient, the particles have to be adequately slow in the first place. In principle, the environment can be arbitrary. While capturing particles in more viscous mediums, e.g. water, can been done [18], optomechanical motion manipulation is limited. The next best bet would be a gaseous environment. Stokes friction in air is given by $F_{air} = 6\pi\eta_{air}Rv$, where η_{air} [78] is the viscosity of air and R and v radius and velocity of the particle respectively, is, however, about 50 times lower than in water [79]. This impacts the maximum velocity allowed in order for the particle to still be trapped, as it enters the previous equation linearly. Even so, injecting a buffer gas can assist this process, as the particles can be cooled by elastic collision with the gas molecules [37, 60].
There are other ways to circumvent the problems posed above. For one, we have already established that optical cavities can slow down and trap particles. Another

Figure 22: Piezoelectric ultrasonic transducer as a particle source for levitated optome-chanics. Ultrasonic vibrations acoustically break the van der Waals' bond between the particles and the glass surface and launch the particles.

way is to trigger the optical trapping potential only once the particle is near the trap center. If the trap depth is large enough, the particle cannot overcome the potential barrier. In either case the kinetic energy of the particle has to be sufficiently low, i.e. a soft launching mechanism is required.

Many optomechanical experiments operate in (ultra-)high vacuum (UHV). Cooling of a levitated nanoparticle to the motional quantum ground state has recently been reported at a pressure of $\sim 10^{-6}$ mbar [39]. For direct trapping in UHV a soft launching mechanism is needed, as there is no surrounding gas to slow the particles down. However, even for a strongly pumped high-finesse cavity[4] this would mean a maximum forward velocity of $v_{max} = 0.8$ m/s. Alternatively, one could use gravity to their advantage, i.e. launching the particles upwards and placing the optical trap near the turning point. Most techniques currently used, however, have significant flaws when operated in UHV. Thus, commonly, the experiment is started at ambient pressure, and, after successfully trapping a particle, subsequently evacuated.

In this chapter I will present the most prominent currently used mechanisms. I will outline their advantages and drawbacks and try to emphasize on why a new particle source would be beneficial for the whole field of levitated optomechanics.

3.1 Piezoelectric ultrasonic transducer

Arthur Ashkin in 1971 [9] used a piezoelectric ceramic cylinder to shake off a single $\sim 15 - 25 \, \mu m$ glass sphere off a glass plate. Applying voltage to certain materials re-

---

[4]Calculations done for $\lambda = 1560$ nm, 400 W intracavity power, 330 000 finesse, $w_0 = 65 \, \mu m$ waist and a silicon particle with $R = 150 \, nm$. Specs from [62]

sults in deformation of the element, a phenomenon called the converse piezoelectric effect [80]. The piezoelectric element sets up vibrations in the glass plate and acoustically breaks the van der Waals' bond between the particle and the glass surface [9]. A schematic of a simple source based on this high-power piezoelectric ultrasonic transducer can be seen in Figure 22.

The acceleration needed to overcome the van der Waals' force can be calculated via the Derjaguin-Muller-Toporov (DMT) model [81, 82] of elastic contact. The pull-off force needed to separate a spherical particle from a flat surface is given by [83, 84]

$$F_{PS} = 4\pi R\gamma, \tag{3.1}$$

where R is the radius of the particle and γ the effective adhesion surface energy. Thus the required acceleration for a spherical particle of mass m and density ρ_p reads:

$$a = \frac{F_{PS}}{m} = \frac{4\pi R\gamma}{\frac{4}{3}\pi R^3 \rho_p} \propto \frac{1}{R^2}. \tag{3.2}$$

Hence, smaller particles require larger acceleration to overcome the van der Waals' bond. In the case of Arthur Ashkin's $\sim 20\,\mu m$ glass spheres this amounts to a force of $\sim 10^4$ g [8]. For a silica sphere of radius $R = 1\,\mu m$, the acceleration is already on the order of 10^8 g [53].

Another advantage of a piezoelectric ultrasonic transducer is its reliability to launch isolated particles instead of clusters. The adhesive force between two spheres of radii R_1 and R_2 can be derived from equation 3.1, by substituting the single particle radius $R = R_1 R_2/(R_1 + R_2)$ [81]. For two identical particles of radius R_P this results in

$$F_{PP} = 2\pi R_P \gamma, \tag{3.3}$$

which is only half of the pull-off force between a particle and a flat surface. Therefore, particles will separate from each other before detaching from the glass surface. More often than not, this will result in single particle launching. However, particles cannot be launched across the whole surface of the coverslip, as due to the vibrations a standing wave forms on the glass. Consequently, there are areas with larger vibrational amplitudes that can launch particles (anti-nodes), and regions that cannot (nodes) [53]. Notably, the particles should be applied dry (or dried before launching), as moisture increases the adhesion of the particles to the surface

[85]. These phenomena were observed in the group of Mark Raizen at the University of Texas at Austin [60].

Conclusively, while ultrasonic vibrations offer an easy way to launch microparticles, the strongest limitation of this source lies in its minimal launchable particle size. Typically, this is $R_{min} \sim 1\,\mu m$ [56], therefore the piezoelectric ultrasonic transducer cannot be used for *nanoparticles*.
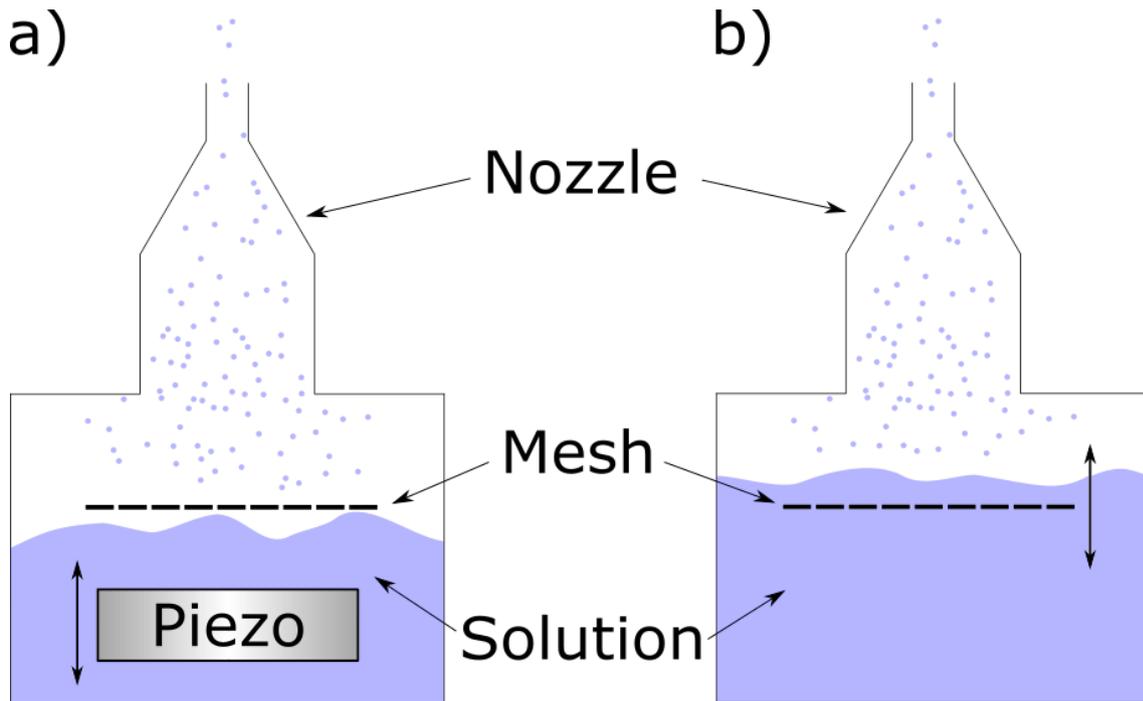
3.2 Nebulizer

Another simple, yet effective approach uses a nebulizer to evaporate highly diluted (nano-)particles [86]. This technique is easy to set up and standard medical nebulizers can be used. While there are many different commercial nebulizers, the most suitable as a nanoparticle source are the ultrasonic (Figure 23a) and the mesh nebulizer (Figure 23b). The ultrasonic one essentially consists of a piezoelectric transducer with a mesh on top. Liquid can be inserted in between the two components. The piezoelement pushes the solution through the grid and creates an aerosol with droplet sizes of several μm. The mesh nebulizer functions similarly, but here the grid itself vibrates and breaks up the liquid [87, 88].

While for medical purposes the aerosol is generally inhaled, here the purpose is to trap particles - ideally without any liquid around them. Ethanol droplets quickly evaporate under standard conditions and leave an airborne particle behind, thus serving as a potent diluter. The concentration of the solution can be opted such that on average there is one or no particle in a single droplet [56]. Attaching a nozzle to the nebulizer allows for more precise injection of the aerosol. Additionally, the design of the nozzle also impacts the number of particles in the aerosol [86].

This technique has proven effective for a number of different experiments. Particles of various sizes have been successfully trapped, ranging from 75 nm [89] to several μm [86]. The first subkelvin parametric feedback cooling of a silica sphere [57] was also reported using this launching technique.

However, this source has several drawbacks. Sputtering of the optical elements of the trap by excess particles is a problem. Additionally, this loading mechanism requires ambient pressure to function in the first place [57]. Moreover, when aiming for ultrahigh vacuum the sprayed aerosol contaminates the chamber such that it becomes difficult to pump to low pressures [90]. To circumvent this problem a

Figure 23: Working principle of two commercial medical nebulizers with a nozzle attached to them. **(a)** Ultrasonic nebulizer. A piezoelectric transducer pushes a liquid through a mesh and creates μm sized droplets. **(b)** Mesh nebulizer. Similarly, the solution is broken up by vibrations of the grid.

load-lock mechanism was developed [89]. This technique uses a mobile active feedback optical trap to transfer a particle in free space from one chamber to another. A particle initially trapped via the nebulizer under ambient pressure can thus be moved from the contaminated chamber to a high vacuum environment in another. Nonetheless, this setup has the disadvantage of a bulky setup and slow duty cycle at low pressure [90].

3.3 Hollow-core photonic crystal fiber conveyor belt

There is the possibility of using a two-step process to load an experiment. Similar to the load-lock, particles can be transferred inside a hollow-core fiber [91]. Two identical Gaussian laser beams (same power, wavelength and polarization) that are coupled in on opposite ends of a hollow-core photonic crystal fiber (HCPCF) form a standing light wave inside the HCPCF and can function as an optical conveyor belt. The eigenmode profile of such a fiber is best approximated by linear polarized modes (LP_{mn}). If perfectly aligned, only the fundamental LP_{01} mode is excited, which has a similar intensity distribution as a Gaussian beam. A detailed description of the mode structure in HCPCFs, theoretical background and experimental setup is given
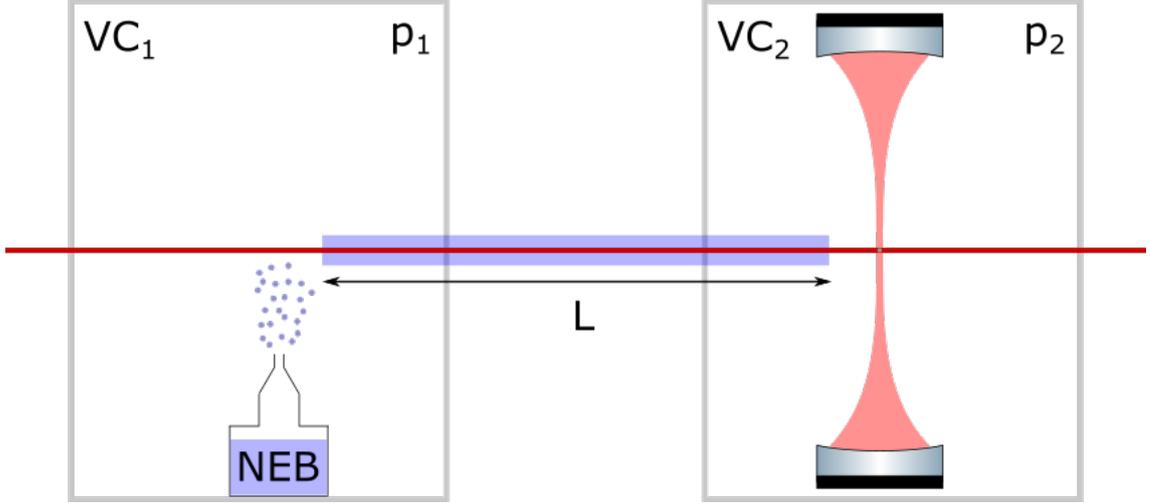
Figure 24: Schematic setup for a two-step loading mechanism including a hollow-core photonic crystal fiber (HCPCF) conveyor belt. A particle is initially trapped in the HCPCF via nebulizer in vacuum chamber one (VC$_1$) at ambient pressure p_1. The particle can then be transferred from the first to the second vacuum chamber VC$_2$ by means of the HCPCF over a length L. The secondary chamber is evacuated to a pressure p_2 and contains the desired experiment to load. Reproduced and adapted from [40]

in [40].

Once a particle is trapped, it can be moved along the fiber axis by introducing a frequency detuning Δ between the two lasers. This causes a movement of the standing light wave that drags the particle along. The velocity of the trapped particle is approximately $v \approx \Delta \lambda / 2$, and the direction of the movement is given by the sign of the detuning [91]. Previous free space conveyor belts were limited to distances on the order of the Rayleigh length [92], whereas this approach is limited by the fiber length, which can be several meters [40].

A schematic of a possible setup with an HCPCF loading mechanism can be seen in Figure 24 [40]. The experiment consists of two chambers, connected by the fiber. First, the particle is trapped in the primary chamber at ambient pressure p_1. While any method can be used for initial trapping, the nebulizer technique is the easiest and contamination of the vacuum chamber is irrelevant. Once trapped, the particle can be transferred from the first chamber to the second via the HCPCF conveyor belt. The secondary chamber contains the optomechanical experiment and is evacuated. The minimal achievable pressure p_2 in the second chamber depends on the core diameter d_c and length of the fiber L, as the difference in pressure between the two chambers Δp scales like $\Delta p \propto p_2 \cdot L / d_c^3$. Chosen correctly, an ultra-high vacuum level of 10^{-10} mbar has been achieved [40].

A hollow-core photonic crystal fiber conveyor belt offers a new potential possibility to load nanoparticles into ultra-high vacuum. It is capable of loading an experiment with a single particle on demand, thus preventing any contamination of chamber and optical equipment. Transport of particle has been shown for particles of various sizes, ranging from 71.5 nm [40] to 960 nm [91]. Furthermore, it has the advantage over a load-lock mechanism of being more flexible and having better throughput. However, until now, stable trapping of particles in the HCPCF, as well as outside of it, has not been successful below ~ 0.1 mbar [40]. This is a phenomenon observable in many a levitation experiment [37, 54, 93, 94] and can be stabilized by 3D-feedback cooling.

3.4 Laser-induced desorption

A laser-induced desorption (LID) based approach provides an alternative to the piezoelectric transducer in order to overcome the van der Waals' bond between particles and substrate. A nanosecond pulsed laser is focused[5] on the backside of a substrate and launches particles on the front close to the focal spot (Figure 25).
The sample can be bulk material [38], particles coated on an opaque thin metal foil [76] or tailor-made nanoparticles etched into a wafer [70]. Launching from a plain wafer is a sort of brute force way, as the material has to be cracked at the surface and there is hardly any control of particle size or shape. Coating of nanoparticles or nanofabricated structures offer a more elegant solution.

The physics behind the launching process is up for debate. One explanation is called laser-induced acoustic desorption, a technique well-known in biophysics [95, 96]. Here, the irradiation causes acoustic shock-waves in the material that are strong enough to overcome the van der Waals' potential and lift the particles up. Another theory is based on laser-induced thermomechanical stress (LITHMOS). Laser-induced stress causes deformation of the substrate and for large enough energies microscopic cracks can be seen on the top side of the sample. These cracks serve as launching sites for particles of arbitrary shapes and sizes [38].

The velocity distribution of particles launched via laser-induced desorption can be influenced by substrate material or thickness. Typical values of forward velocities range from $5 - 30$ m/s [70]. Significant change is observed when the free-flight particles are exposed to an electric field. This is because particles launched via laser-

---

[5]Typical values are: spot size $\sim 100\,\mu m$, wavelength 532 nm, pulse energies $1 - 3$ mJ and pulse duration 6 ns [62].
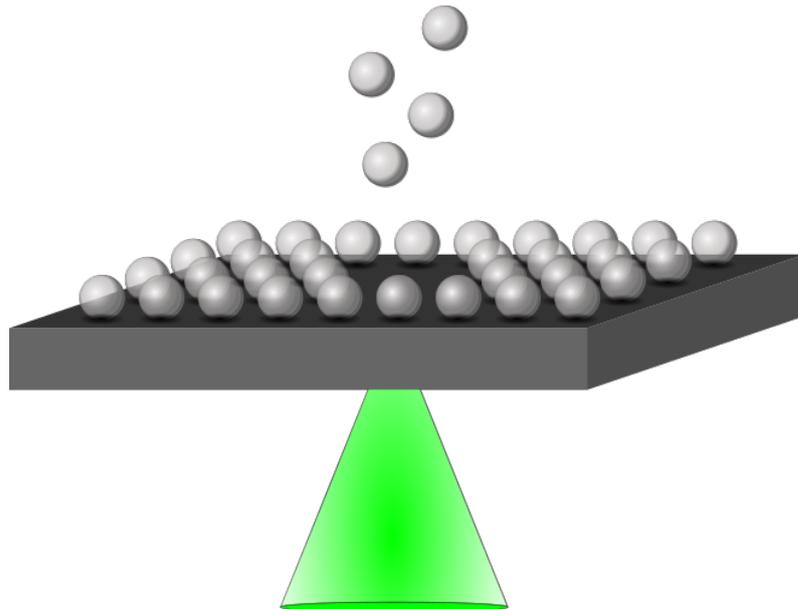
Figure 25: Schematic illustration of the working principle of laser-induced desorption (LID). Illuminating the back side of a sample with a pulsed laser launches particles from the front side.

induced desorption are generally charged [97]. This raises another problem when loading an optical cavity. Clusters of particles have been observed to contaminate the mirrors, as they are attracted by the charged mirror surfaces. Again, an electric field can counter this problem, although at the detriment of the slowest particle forward velocity[6]. Ultimately, particles launched by LID are again too fast to be directly trapped below modest vacuum pressure.

For other experiments, however, charged particles can be very useful. Indeed, loading of a Paul trap directly in high vacuum has recently been reported [90]. The method combined laser-induced desorption with temporal control of the trap potential and allowed for particle trapping at pressures around $\sim 10^{-7}$ mbar. Even so, for experiments relying on gradient forces for trapping, or if neutral particles are required, the search of an UHV compatible source continues.

---

[6]A detailed analysis of forward velocities and the impact of substrate material, thickness as well as potential difference is given in Appendix B of [70].

4 Laser printing of nanoparticles

4.1 Motivation

Nanotechnology has come a long way since Richard Feynman's famous 1959 lecture *"There's Plenty of Room at the Bottom"* [98]. A Google search of the word "nanoparticles" now yields almost 38 Million results. In medicine, nanoparticles can act as drug delivery systems [99] or imaging contrast agents [100]. In physics and biology, nanoparticles make an interesting candidate for sensing applications. Noble metal nanoparticles can support collective electron oscillations after excitation with light, an optical phenomenon called localized surface plasmons. The resonance frequency of these plasmon oscillations strongly depends on size and geometry of the nanoparticle, thus making them attractive for real-time sensor technologies [101–103]. Levitated silica nanoparticles can be used for zeptonewton force sensing [42] and silicon nanorods have been proposed as torque sensors with an estimated sensitivity down to 10^{-22} Nm [43].

These are only a few entries in a long list of possible applications of nanoparticles. Therefore, a fabrication method with precise control over sizes, shapes and positions is of utmost importance. This is why the quantumoptics group of Boris Chichkov in Hanover has worked on a new nanoparticle creation process. It is based on a laser-printing method that is long used in bioengineering. By irradiation with short laser pulses proteins [104, 105], living cells [106, 107] or tissue [108, 109] can be printed in arbitrary patterns. They adapted this technique to create spherical nanoparticles of various materials, including silicon [110, 111], gold [112], titanium [113] and germanium [114].

As established in chapter 3, a good and suitable nanoparticle source for levitated optomechanics is characterized by various parameters, including reliability, reproducibility, possible particle size or vacuum-compatibility. The sources presented before are state-of-the-art, yet none of them tick all the boxes - each one of them has their advantages and drawbacks. Laser printing of nanoparticles has the ability to create single particles in-situ and precisely deposit them. Paired with the fact that this technique is highly reliable and the results are reproducible, it is an intriguing prospect as a source for levitated optomechanics. Left to question is, whether or not such a source would be operable in (ultra-)high vacuum.

4.2 Working principle
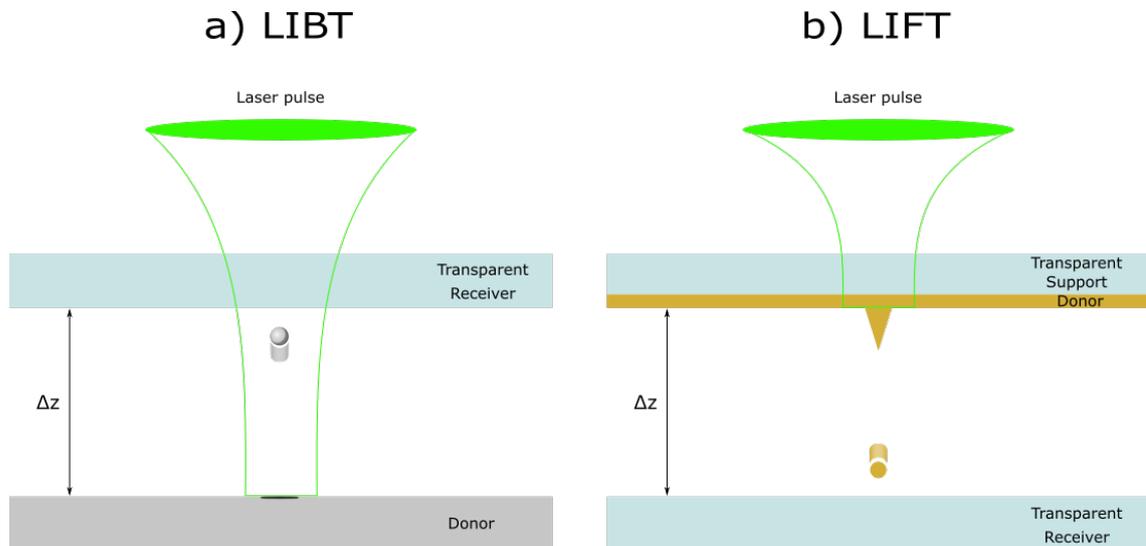
Figure 26: Schematic working principle for laser-induced transfer. A femtosecond laser is focused on a donor substrate and induces a melting process. Particles thus created are ejected away from the surface and collected by a receiver, affixed at a distance Δz away from the donor material:. **(a)** Laser-induced backward transfer (LIBT). Irradiation of the donor happens through a transparent receiver substrate. **(b)** Laser-induced forward transfer (LIFT). Irradiation of a thin metal layer through the transparent donor substrate. Reproduced and adapted from [112].

The nanoparticle printing process described in this chapter uses sharply focused femtosecond laser pulses. Depending on laser focus, pulse energy or donor material, the particle generation process can be very different - ranging from single specimen to countless small particles. It has been shown, that nanoparticles of various materials can be precisely deposited on an arbitrary receiver substrate, and that their radii can be freely adjusted between 100 and 800 nm [110–112]. For silicon it has been demonstrated that by exposure to further femtosecond pulses, the initially amorphous particles can be controllably crystallized [110, 115].

The basic working principle of this technique relies on the transfer of particles from a donor substrate to a receiver substrate, separated by a distance Δz. Typically, the donor is either a bulk sample of the material or a thin film coated on a glass surface. A femtosecond laser is focused on the substrate and induces a melting process. Particles thus created are ejected away from the surface and collected by the receiver, in most cases another glass surface. There are two variants of this process, distinguished by the direction of the ejection of the particles with respect to the direction of the laser beam. The process where the particles are transferred in the same direction as the laser beam is called laser-induced *forward* transfer (LIFT).
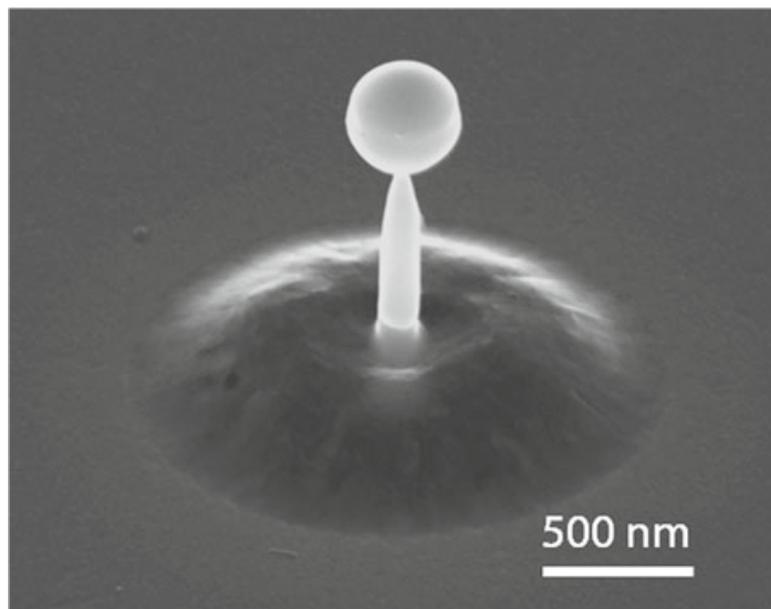
Figure 27: SEM image of a 60 nm gold film subsequent to fs-laser pulse irradiation. The metal melts locally and a microbubble and a nanojet form. An almost perfectly spherical particle on the tip of the back-jet forms when increasing the pulse energy. Taken from [103].

If the particles are ejected in the opposite direction of the laser we talk about laser-induced *backward* transfer (LIBT). Schematics of the two processes can be seen in Figure 26.

Upon irradiation by an ultrashort laser pulse, electrons in the material absorb the energy and are excited. For fs-pulses, the predominant mechanism for exciting valence electrons into the conduction band is single photon absorption, as the photon energy is generally larger than the bandgap. This carrier excitation is faster than the thermalization that follows. Absorption of photons happens in the fs-regime, while carrier-phonon scattering or thermal diffusion takes place on the pico- to nanosecond timescale. [116].

Consequently, the laser induces melting of the donor material inside the beam spot but not around it. This allows for a very controllable particle creation process. The liquid-solid phase transition, and the density and volume changes that come with it, cause strong temperature and pressure gradients in the material [103, 117]. These gradients, as well as the surface tension of the molten material, lead to the deformation of the substrate and creation of structures. The exact process differs from material to material. Generally, one has to distinguish between donors whose density decreases during the phase transition solid-liquid, i.e. they expand while melting, and materials whose density increases during this process. Noble metals such as gold or silver belong to the first group, while semiconductors such as silicon
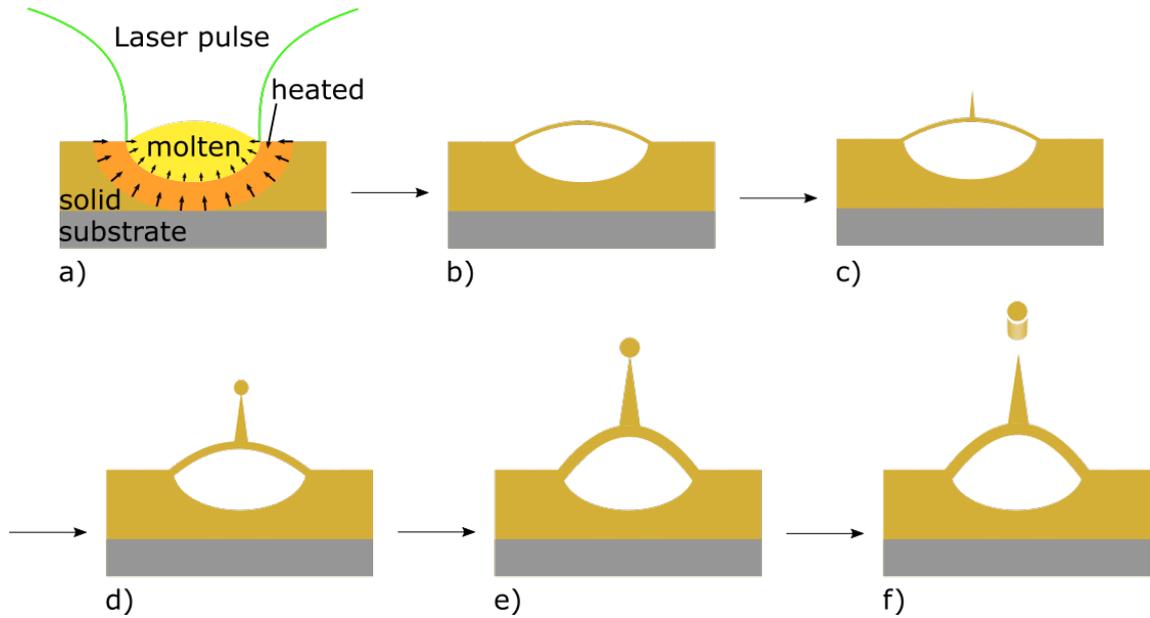
Figure 28: **(a)** Representation of fluid dynamics. Due to ultrafast heating the gold film only melts locally. Gradient forces perpendicular to the solid-liquid interface push the molten material away from the solid. **(b) - (f)** Schematic illustration of the melting process for gold after fs-laser irradiation. Power is gradually increased with each picture. First, hollow microbubbles form, then nanojets appear on top of the bump. Increase in pulse energy leads to the formation of almost perfectly spherical particles on top of the jet-like protrusion. These structures scale with the laser power. At a certain threshold the spherical particle is ejected perpendicular to the gold surface. Idea from [118].

or germanium are representatives of the second group [103].

A particle generation process for gold can be seen in Figure 27 [103]. This scanning electron microscope (SEM) image of a 60 nm thin gold film after irradiation with a single 30 fs laser pulse, was taken by the group of Boris Chichkov from the Leibniz university in Hanover. The fs-laser pulse locally melts the metal and leads to the formation of a microbubble and a nanojet (Fig 28).

The gradient forces mentioned earlier are perpendicular to the solid-liquid interface and push the molten material away from the solid (Fig. 28 a). Due to the surface tension of the liquid gold the hollow bumps form (Fig. 28 b). With increasing molten material nanojets form on top of the microbubbles (Fig. 28 c) [117, 118]. With further increase of the laser power, the surface tension induces the shaping of almost perfectly spherical particles on the tip of the nanojets (Fig. 28 d). The fluid dynamics in this system seem to be very similar to those of a droplet hitting a liquid surface. The sizes of the protrusions scale with laser power, as the amount of molten material increases (Fig. 28 e). The particle can be separated from the jet and ejected perpendicular to the metal surface by surpassing a certain energy
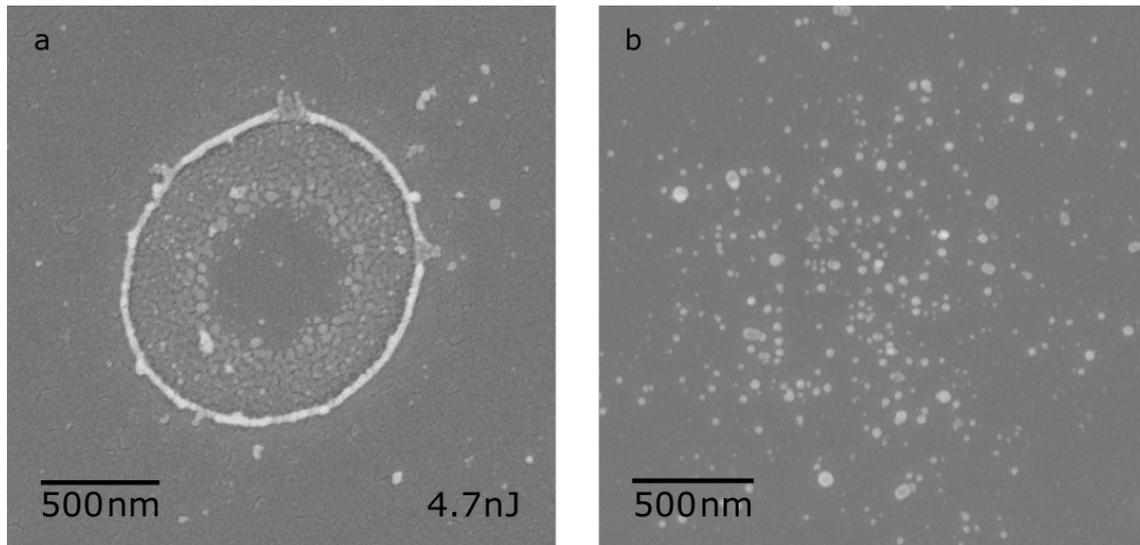
Figure 29: **(a)** SEM image of 40 nm silicon sputtered on glass after irradiation by a single 257 fs laser pulse ($\lambda = 515$ nm). The liquefied silicon forms a toroidal ring around a material depression. **(b)** At higher pulse energies the ring breaks up and countless very small particles are launched towards the receiver substrate.

threshold (Fig. 28 f) [103, 119].

The result is a reliable and reproducible particle source that can print with extraordinary spacial accuracy. Additionally, the particle size can be precisely controlled via the pulse energy, laser focus and donor layer thickness [103, 112].

This process, however, changes when using a donor material whose density increases while melting, for example silicon. The reduction of volume of the molten material leads to a depression on the surface of the material. Contrary to gold, the liquid silicon does not form a nanojet in the center, but a toroidal ring around the depression, given a Gaussian beam profile. This happens because liquid silicon moves to regions with lower intensity in the focus area. Towards the center of the focal spot, i.e. regions with higher intensity, the silicon is heated up more strongly compared to the outer parts. Therefore, the material in the middle has lower surface tension [120, 121] and molten silicon thus moves towards colder regions [103, 119]. The resulting ring can be seen in Figure 29 a. Depicted is a SEM image of 40 nm silicon sputtered on glass after irradiation by a single 257 fs laser pulse ($\lambda = 515$ nm). With increasing pulse energy the toroid breaks up in countless very small particles that are ejected towards the receiver substrate (Figure 29 b) [111].

Moser et. al [122] classify three different regimes to describe this process, depending on the laser intensity (their work was done at $\lambda = 1040$ nm, pulse length of 380 fs). They distinguish between the *Low Fluence Regime, Middle Fluence Regime* and *Hydrodynamic Motion*. The low fluence regime ($I < 2$ J/cm^2) is characterized
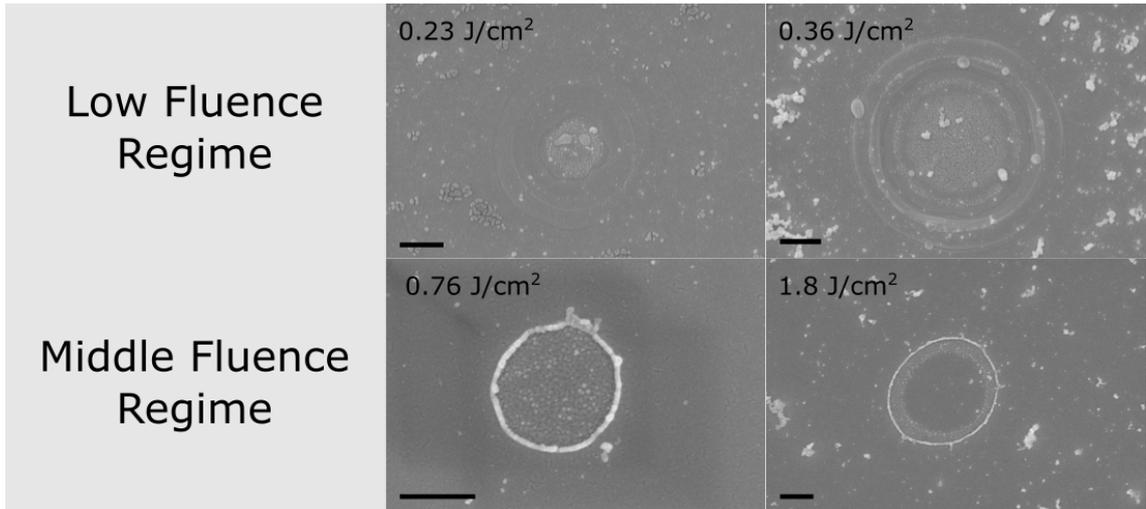
Figure 30: Ablation regimes for silicon after single pulse irradiation (pulse duration 257 fs, upper row: $\lambda = 1030\,\text{nm}$, lower row: $\lambda = 515\,\text{nm}$,). **Upper Row:** In the low fluence regime little to no ablation occurs. However, surface modification is clearly visible. **Lower Row:** In the middle fluence regime we observe notable material ablation and the formation of a toroidal ring. With increasing intensity the ablation depth increases and more material is ejected. All scale bars are 500 nm.

by a central melt region, followed by a re-solidification zone. While material deformation is clearly visible, close to no ablation is observed. When entering the middle fluence regime $(2 - 4\,\text{J/cm}^2)$ the ablation depth increases and notable material ablation occurs. In this regime. At even greater intensities $(I > 4\,\text{J/cm}^2)$ significant hydrodynamic motion arises and the material ablation further increases. In our experiments we did not encounter hydrodynamic motion as described by Moser et. al. We attribute this to the fact that the ablation depth of $> 150\,\text{nm}$ [122] exceeds the thickness of our samples. SEM images of the observed ablation morphology stages can be seen in Figure 30. The upper row shows images of a 50 nm silicon-on-insulator wafer after irradiation by a single 257, $\lambda = 1030\,\text{nm}$ laser pulse (left: $0.23\,\text{J/cm}^2$, right: $0.36\,\text{J/cm}^2$). The similar experimental conditions as in [122] allow for easy classification in the low fluence regime. For larger intensities we switched to a 40 nm silicon sputtered on glass sample to avoid side effects at the Si-SiO$_2$ junction. Already at $0.76\,\text{J/cm}^2$ (bottom left) we observe the formation of a toroidal ring similar to Figure 29 a, however with little to no visible ablation at the center. We conclude that this image was taken near the transition from low to middle fluence regime. At $1.8\,\text{J/cm}^2$ (bottom right) we observe significant ablation at the center, clearly placing this process in the middle fluence regime. The bottom row images were taken after irradiation by a single $\lambda = 515\,\text{nm}$ pulse (still 257 fs pulse duration), which could explain the discrepancy in threshold intensity when compared to Moser et. al.
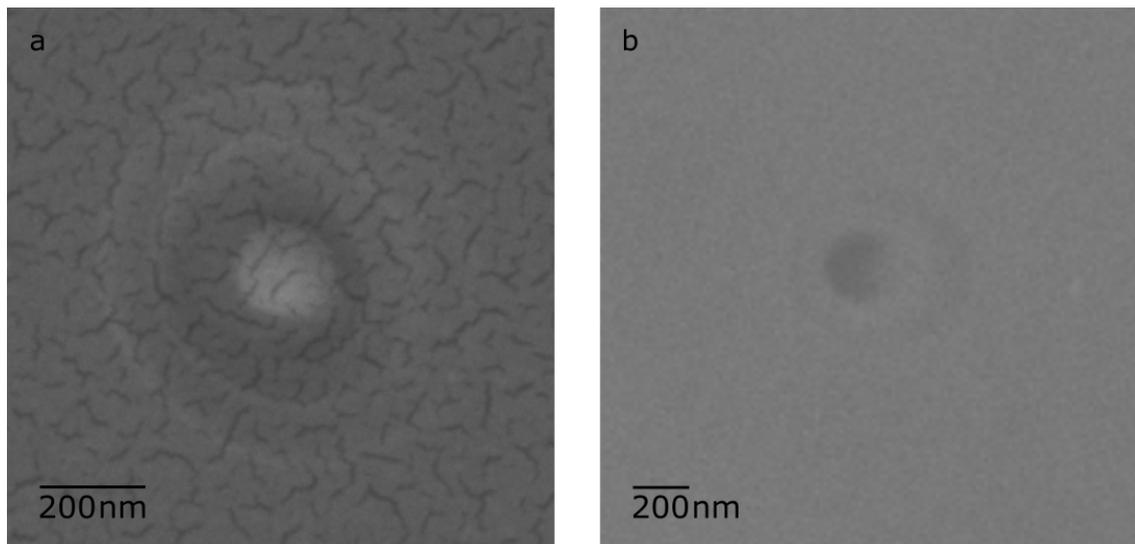
Figure 31: Impact sites on a 50 nm SOI wafer for different pulse energies ($\lambda = 515$ nm, pulse length 257 fs). **(a)** For lower pulse energies the particle produced sticks to the donor surface. Here, the melting area is measured to be $\sim 1\,\mu m$. The cracks in the surface are an artifact of the SEM measurement, as the sample is gold metallised. **(b)** At higher pulse energies the particle is ejected away from the surface. The crater left behind is clearly visible.
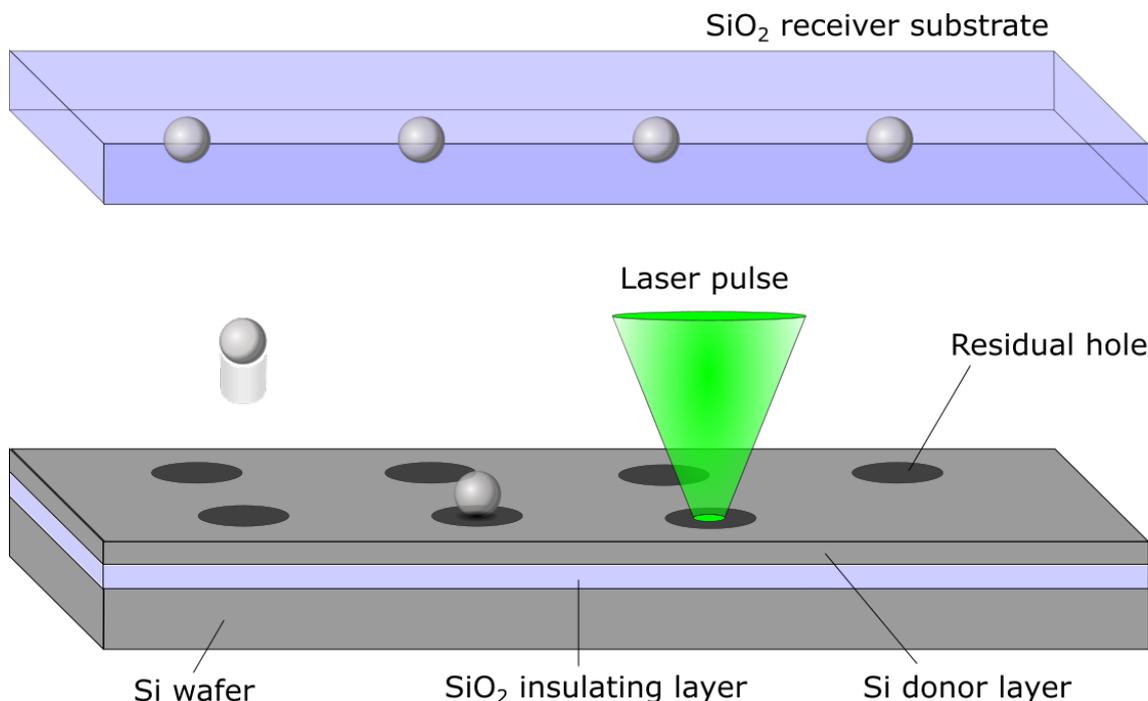
Figure 32: Schematic printing process of silicon particles. In this case the base material is silicon-on-insulator (SOI). A thin layer of silicon dioxide (SiO_2) separates the bulk silicon from a thin silicon donor layer and thus limits the melting depth. The generated particles are launched upwards and collected by a receiver substrate. Reproduced and adapted from [110].

For any pulse energy, the statistical distribution of sizes of particles created by the process described before is very broad. Therefore, there is no reliability in, or

control of, particle diameters. Furthermore, shapes and numbers are uncontrollable and spacial precision is only available for the whole speck of particles. While this method allows for printing of even smaller particles, the lack of control makes this method less appealing.

There are methods to circumvent these problems. In order to create single particles the liquid silicon has to aggregate at the center of the focal spot. One way to do this, is to use a ring-shaped intensity distribution. While some of the liquid silicon still migrates to the outer edge of the focal spot, more will garner at the center [111].

A more elegant solution is provided by silicon-on-insulator (SOI) as donor material (Figure 32). Here, a thin layer of silicon dioxide (SiO_2) separates the bulk silicon from a thin silicon donor layer. The SiO_2 melts at much higher temperatures and is unaffected during the melting process of the bulk silicon. It thus provides a cold surface where the silicon can migrate to. This leads to accumulation of liquid silicon at the center of the beam instead of a toroid at the outer edge. The molten silicon then contracts to a single spherical droplet due to surface tension. Similar to the particle generation process of noble metals, the nanoparticle has a momentum pointing away from the surface and for high enough pulse energies the particle is ejected (Figure 31 b). For lower energies the silicon first forms a nanobump (contrary to gold this bump is not hollow), later the spherical particle is formed, yet sticks to the donor surface (see Figure 31 a) [110].

4.3   Experimental results

We use the second harmonic output (515 nm) of a *Light Conversion PHAROS-PH1-10W* laser with a pulse length of 257 fs for our printing process. Our go-to laser specifications are set to 10 W and 100 kHz maximum repetition rate. We used three different substrates to test our setup: commercial silicon-on-insulator (SOI) wafers with donor layers of 50 and 200 nm and 40 nm sputter coated silicon on silicon-dioxide (Sp-Si). For the SOI samples we only attempted laser-induced backward transfer (LIBT), whereas for Sp-Si we experimented with both LIBT and LIFT (laser-induced forward transfer).
The basic optical setup for our experiment can be seen in Figure 33. Not depicted is our in-situ interferometric scattering microscopy (iSCAT) detection setup which will be described in chapter 5. At 100% emission a single laser pulse has an energy of 100 μJ, whereas for single particle generation pulse energies below ~ 10 nJ are required. Therefore, we weaken the beam via a set of neutral density (ND) filters.
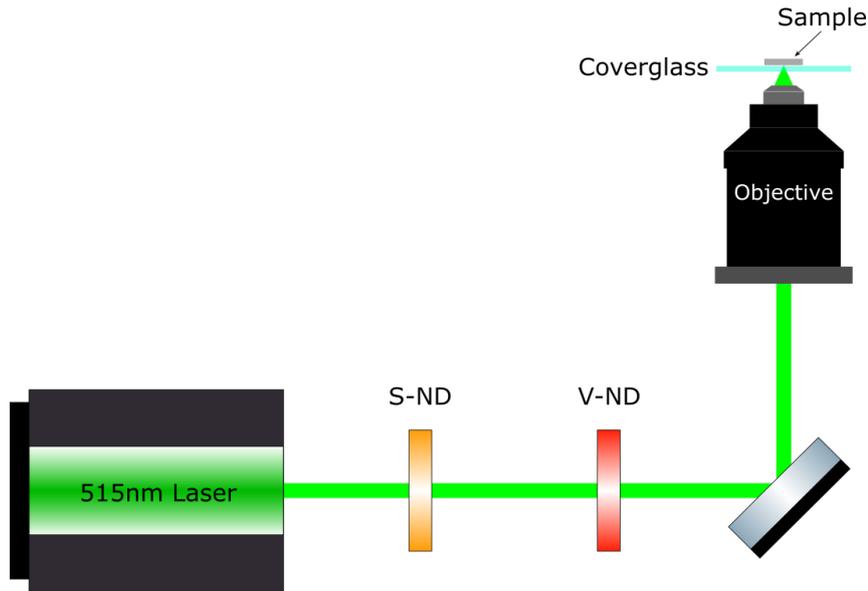
Figure 33: Simple schematic of a basic printing setup. We use a commercial femtosecond laser with a center wavelength of 515 nm and a pulse length of 257 fs. A reflective variable neutral density filter (V-ND) with a continuous optical density between 0 and 2 mitigates the initial power by a factor of up to 100. Further attenuation by a factor of 100 is provided by a set of fixed-value ND filters (S-ND). The total system thus alters the laser pulses by a factor of $9.5 \cdot 10^{-5}$, thus achieving the desired pulse energies below 10 nJ. The laser beam is subsequently focused onto the sample by a high-NA microscope objective. The printed particles are collected on a coverslip for further evaluation.

The first is a reflective set-value neutral density filter[7] (S-ND) that provides a mitigation factor of ~ 100. The second ND-filter[8] (V-ND) is again of reflective nature, but has a variable, continuous optical density (OD) with a maximum value of 2 (reduction by another factor ~ 100). The total system thus alters the laser pulses by the desired factor of $9.5 \cdot 10^{-5}$. The filters are tilted as to avoid back-reflection in to the laser. Continuing from there, we only adjust the power of the laser itself. A characterization of the single pulse energies depending on the attenuation factor of the laser is given in Figure 34.

Subsequent to energy mitigation the laser is focused onto the substrate. Here we tested three different microscope objectives. The first[9] has a numerical aperture (NA) of 0.4, a magnification of 20 magnification and coverslip correction. Furthermore, we used one with 0.9 NA, 40x magnification and also aberration correction[10] and one with 0.95 NA, 63x magnification but without aberration correction[11]. Compared to the 0.9 NA objective, the missing coverslip correction of the last objective
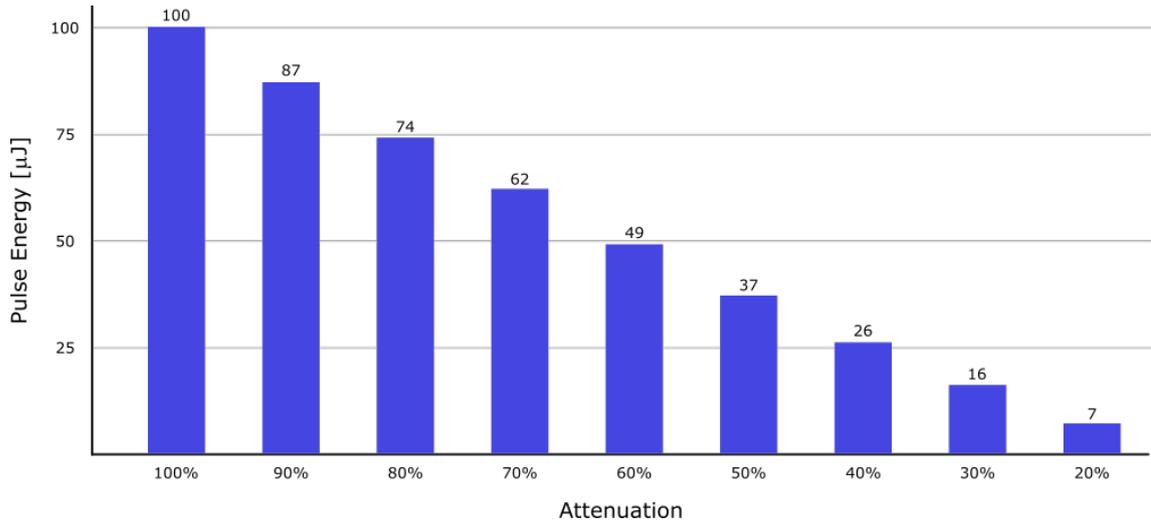
---

[7]Assembly of $1.0 + 0.6 + 0.4$ optical density (OD) filters out of Thorlabs NDK01
[8]Thorlabs NDC-100C-2
[9]Zeiss LD Plan-Neofluar 20x/0,4 Korr Ph2 M27
[10]Zeiss EC "Plan-Neofluar" 40x/0,9 Pol M27
[11]Zeiss "Achroplan" 63x/0,95 D=0 M27

Figure 34: Single pulse energy depending on internal laser power attenuation factor. Measurements were performed without any additional filters.

resulted in roughly 2.5 times higher pulse energies needed to create particles of relatable size, thus making it effectively very similar to the one with only $0.4\,\mathrm{NA}$.

At standard pressure, we found that a distance of $5-10\,\mu m$ between the coverslip and the sample is ideal. Below $5\,\mu m$, or for large pulse energies, the silicon is still too squashy and will blob when hitting the glass surface. On the other hand, for distances larger than $10\,\mu m$, chances that the particle will ricochet off the surface or shatter on impact, drastically increases. Surprisingly, in our setup the most reliable way to achieve this, is also the easiest - by simply putting the wafer on top of the glass results in an average distance between $10-15\,\mu m$. However, it is important to use sturdy coverslips as more bendy ones will arc due to the weight of the wafer. This will increase the average distance between sample and glass and makes patterning much more tedious as the focus has to be constantly adjusted.

Typical printing patterns can be seen in Figure 35. On the left we can see the impact pattern on a $40\,\mathrm{nm}$ Sp-Si sample. For reference and easier detection at the scanning electron microscope (SEM) we first write a high-power horizontal line in the wafer (distinct line bottom left). Then we typically shoot ten same-energy single pulses vertically, switch column and decrease the energy. The resulting rectangular pattern is easy to analyze and provides a variety of different particles. The printed particles are collected on the coverslip and can be analyzed at the SEM. On the right we see a typical nanoparticle pattern created by a $50\,\mathrm{nm}$ SOI wafer. The energy is gradually increased from left to right. For higher pulse energies we regularly observe a dual particle creation process. For lower energies on the other hand, we record a success rate of 100% single particle printing. Furthermore, at a distance of $\sim 10\,\mu m$ the deposition is precise and arbitrary patterns can be created.
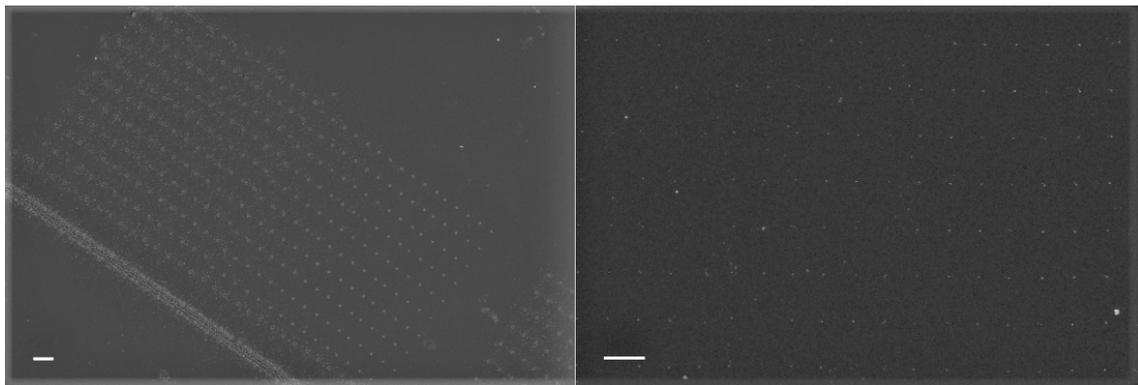
Figure 35: Left: Pattern of impact craters on a 40 nm Sp-Si sample. Distinct line at the bottom serves as a reference and for easier detection at the scanning electron microscope. Pulse energy is gradually decreased from left to right. At larger pulse energies material is distributed around the crater. Towards lower energies we enter the regime where single particles can be created. **Right:** Printed pattern of single or dual particles. Energy is increased from left to right. For higher pulse energies occasionally two particles emerge in the process, whereas for lower energies a success rate of 100% single particles is recorded. Scale bars are 10 μm.

Close up scanning electron microscopy (SEM) images of particles printed by single shots are given in Figure 36. The upper row depicts particles that were created by the 0.95 NA objective, the particles on the lower row were printed with the 0.9 NA objective. For the former we were able to print 180 nm and 257 nm particles at 1.9 and 3.5 nJ respectively. Shots with the other objective needed roughly 2.5 times higher energies (5.3 and 8.3 nJ) to create particles of comparable size (180 nm and 280 nm respectively). We attribute the large discrepancy in pulse energies to the aforementioned absence of aberration correction of the 0.95 NA objective. Unfortunately, vibrations at the SEM caused by construction work around the university often limited the resolution and resulted in blurry pictures.

The focus is set by a gradual approaching method and by continuous observation of the sample via interferometric scattering microscopy (see chapter 5 for a theoretical description and the optical setup). First, coarse adjustment is done by focusing on imperfections or dust particles on the sample. A single pulse test shot then tells us how to proceed. On the one hand, if we observe an impact crater we can go on to fine tuning the focus. On the other hand, if no crater is visible the focus is far-off and we have to adjust the coarse focus by several μm until an impact site is observed.

We then switch to an open-loop piezo system for fine tuning. We take steps of $\sim 1\,\mu$m to either side of the focus and pick the piezo position of the most prominent crater as the new set point. We repeat this procedure for the new set point but take
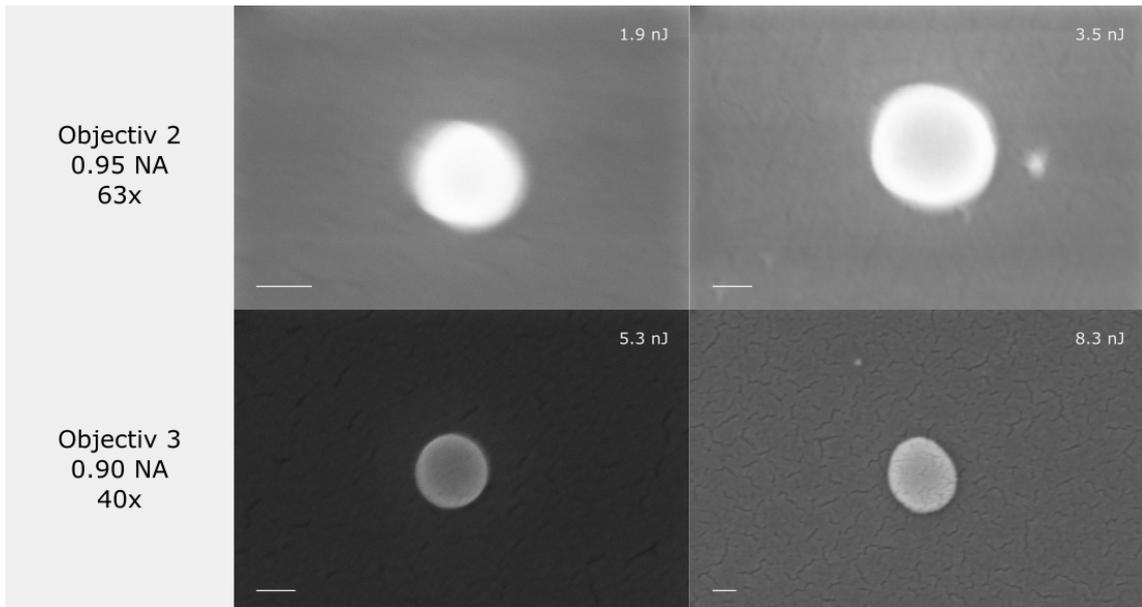
Figure 36: Particles created with two different objectives. **Upper:** A 180 nm and a 257 nm particle printed with 1.9 and 3.5 nJ respectively. **Lower** Particles with similar sizes (left: 180 nm, right: 280 nm) are created at much higher energies (5.3 and 8.3 nJ respectively). We attribute this large difference mainly to the fact that objective 1 has aberration compensation and objective 2 does not. All scale bars are 100 nm.

smaller steps. We repeat this iterative process until we observe no difference between two neighbouring craters. We estimate the precision to be on the order of ~ 100 nm.

Tests with 40 nm sputtered silicon did not yield any useful results, neither for LIBT nor for LIFT. SOI samples were only tested in a LIBT setup. For 200 nm SOI we were not able to create single particles, independent of pulse energy. Instead we observed a multitude of small particles, a process attributed to pure silicon wafers as discussed in chapter 4.2. For 50 nm SOI we were able to print nanoparticles of various sizes. Already small differences in pulse energy result in a measurable size discrepancy of the printed particles. This also includes drifts in focus, thus making vibrations isolation and consistent focus finding of utmost importance.

5 Interferometric scattering microscopy (iSCAT)

5.1 Motivation

In biology, label-imaging, especially fluorescence microscopy, provides a useful method to study live cells and observe single molecules. These methods have enabled many valuable studies [123–125] and have become routine in laboratories. However, optical detection of fluorescent dyes is limited by photobleaching, an effect that describes the permanent loss of fluorescence due to the continued exposure to light [126]. Semiconducting tags are subject to so-called "blinking" effects, where their luminescence is randomly turned "on" and "off" under continuous excitation and thus run into similar problems as fluorescent labels [127]. In 2002 Boyer et al. proposed nanometer-sized metal particles as an alternative to fluorescent or semiconducting tags [128]. Metallic particles do not suffer from any of the aforementioned effects, they are, however, more difficult to detect. One reason is that the elastically scattered light of a nanoparticle is hard to distinguish from the background.

Worries, whether or not tags alter the behaviour of the specimen, pose another, more general, problem to label imaging. This prompted a systematic search for a label-free detection method of nano-objects and single molecules in the early 2000s. Several techniques were developed over the years, Boyer et al. explored photothermal imaging [128], others include dark-field microscopy [129] or total internal reflection imaging [130].

However, all of these methods rely on a strong scattered light signal, which scales with the particle radius R as R^6. For very small particles this signal is rapidly drowned by the background. Therefore, detection of specimen in this regime comes down to the ability to detect a weak signal and to distinguish this signal from the background [131]. A solution to this problem is provided by interferometric laser microscopy, developed as early as 1989 by Batchelder and Taubenblatt [132]. Already in 1991 Amos and Amos reported the visualization of individual microtubules by confocal microscopy [133]. Further progress then was reported by Lindfors et al. in 2003, who were able to detect particles down to a nominal diameter of $D = 5\,\mathrm{nm}$ [134]. In 2009 background suppression was improved, and the name *Interferometric scattering microscopy* (iSCAT) first popped up [135].

Since then iSCAT has served as an easy and label-free in-situ detection method for various important works across multiple scientific fields, among others pathogen identification of viruses [136], evaluation of cancer cells [137], single microtubule imaging [138], single exosome imaging [139] and imaging of material functionality [140]. Although an abundance of acronyms are used for each new experiment, the underlying physics stay the same [141].

We can now also use this method for our femtosecond laser-desorption experiment. It is capable of resolving both the impact craters of the fs-laser at the donor material, as well as single particles created by the method, collected on a glass cover slip. It provides a qualitative measure whether a test was successful or not and can aid in focus fine-tuning.

5.2   Theoretical description

In principle the interferometric scattering microscopy (iSCAT) relies on the inter-ference between the light scattered off the object in question and a reference beam. While there are many possible configurations to realize such an experiment, they all rely on the fact that monochromatic, coherent light can interfere with itself. If the particle sits on, or close to, a partially reflective surface, for example a glass cover slip, this enables the back-reflected light to act as the reference beam. An illustration of this concept can be seen in Figure 37.

Consider the complex electric field $\bar{E}_s = E_s e^{i\phi_s}$ scattered from the object and the reference field $\bar{E}_r = E_r e^{i\phi_r}$. A detector then reads the signal [141]:

$$I_{det} = |\bar{E}_r + \bar{E}_s|^2 = |E_r|^2 + |E_s|^2 + 2E_r E_s \phi. \tag{5.1}$$

The three components of the detection signal can be identified as the reference intensity $I_r = |\bar{E}_r|^2$, the pure scattering signal $I_s = |\bar{E}_s|^2$ and the interference cross-term $2E_r E_s cos\phi$, where $\phi = \phi_r - \phi_s$.

Now, the reference beam is simply the part of the incident light field $\bar{E}_i$ that is reflected at the glass surface of the cover slip. We can then write $\bar{E}_r = r\bar{E}_i e^{i\phi_r}$, where r is a real value denoting the reflectivity of the glass. Upon reflection at a medium with a lower refractive index no phase shift is accumulated [142], however the Gaussian beam is still subject to a Gouy phase shift of $-\pi/2$ with respect to the incident beam $\bar{E}_i$ [134, 143], i.e. $\bar{E}_r = r\bar{E}_i \cdot e^{-i\pi/2}$.

Similarly, we can express $\bar{E}_s$ in terms of $\bar{E}_i$. Consider a spherical particle of diameter

69
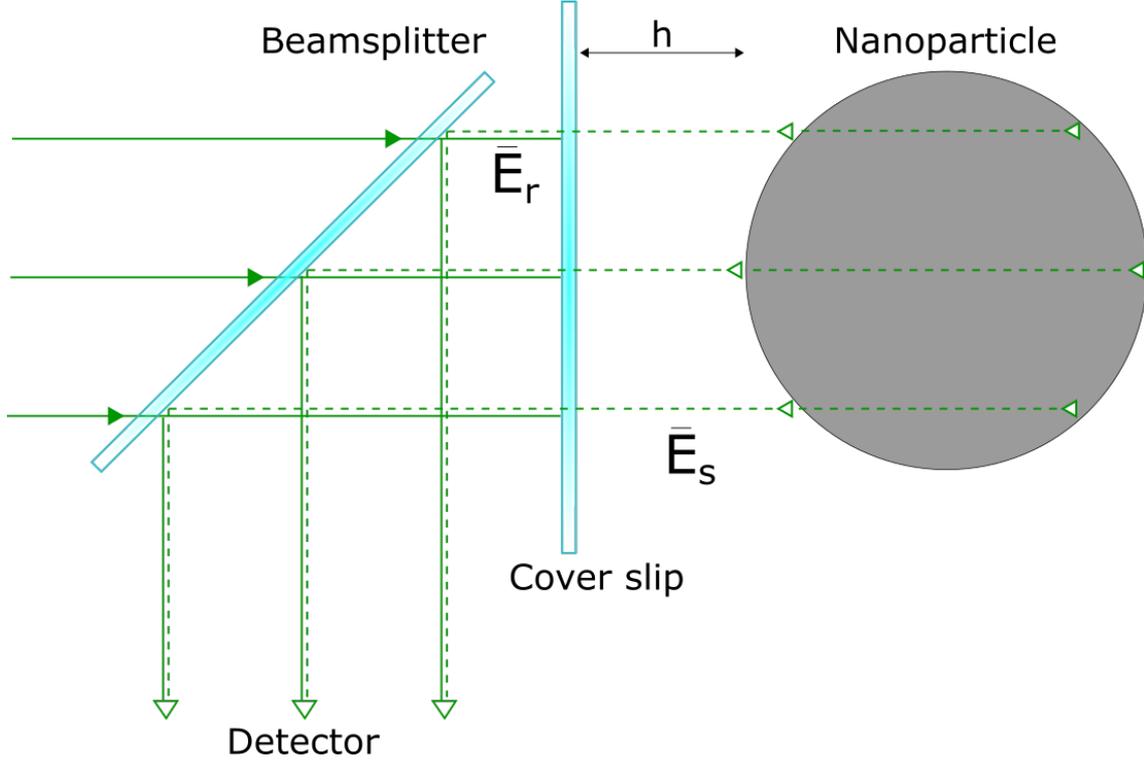
Figure 37: Interferometric detection scheme with back-reflection as the reference beam. The incoming light is partially reflected at the cover slip and partially scattered at the nanoparticle. The back-scattered signal $\bar{E}_s$ (dashed green) is then superimposed with the back-reflected light $\bar{E}_r$ (solid green). Reproduced and adapted from [141].

$D = 2R \ll \lambda$. In this case, the predominant scattering process is Rayleigh scattering, which scales with the polarizability α of the particle. We can then write $\bar{E}_s = s\bar{E}_i$, where $s = |s|e^{i\phi_s}$ is proportional to α [134]:

$$|s|(\lambda) \propto \alpha(\lambda) = 4\pi\varepsilon_0 R^3 \left(\frac{\varepsilon(\lambda) - 1}{\varepsilon(\lambda) + 2} \right), \tag{5.2}$$

where ε_0 is the vacuum permittivity and ε dielectric constant of the spherical particle. The measured intensity at the detector I_{det} can then be expressed as:

$$I_{det} = I_r + I_s + 2E_r E_s cos\phi = I_i \cdot \left(r^2 + |s|^2 + 2r|s|cos\phi \right) \tag{5.3}$$

where $I_i = |\bar{E}_i|^2$ denotes the intensity of the incident light field. The pure scattering term proportional to $|s|^2$ scales with α^2 and therefore drops with R^6. Compared to the interference cross-term, which behaves like R^3, the scattering signal can be neglected, assuming $I_s \ll I_r$:

$$I_{det} \approx I_i \cdot \left(r^2 + 2r|s|cos\phi \right) \tag{5.4}$$

When subtracting the background intensity I_r one can seclude the interferometric cross-term, the most interesting part of the detection signal:

$$I_{det} - I_r \approx 2I_i r |s| cos\phi \tag{5.5}$$

The contrast c between an image with nanoparticles compared to one without then reads [141]:

$$c = \frac{I_{det} - I_r}{I_r} = \frac{2E_s E_r cos\phi}{I_r} = 2\frac{E_s}{E_r} cos\phi. \tag{5.6}$$

Or, written in terms of the incident electric field $\bar{E}_i$:

$$c = \frac{2I_i r |s| cos\phi}{r^2 I_i} = 2\frac{|s|}{r} cos\phi. \tag{5.7}$$

Equations 5.6 and 5.7 suggest that the contrast, or sensitivity, can be increased tweaking several parameters. Firstly, one could minimize the denominator, E_r or r. While this is true, it comes with a trade-off. Reducing the signal reflected from the glass surface also implies reducing the overall strength of the signal, directly impacting the signal-to-noise ratio (SNR) in shot noise limited detection [141].
On the other hand, one can increase the numerator E_s or $|s|$, i.e. the polarizability of the particle in question. In experiments like ours, where one does not rely on a specific material, it is a very real option to increase the sensitivity of the setup. As an example, let's compare bulk silicon (Si) and fused silica (SiO$_2$) nanoparticles illuminated by a laser with wavelength $\lambda = 515$ nm. The permittivity of a particle is the square of it's complex refractive index [144] $\varepsilon = \underline{n}^2 = (n + ik)^2$, where n is the "normal" refractive index k is called the *extinction coefficient*. For silicon $n = 4.22$ and $k = 0.06$ [145] and for SiO$_2$ $n = 1.16$ [146]. This results in a ratio of polarizability:

$$\frac{\alpha_{Si}}{\alpha_{SiO_2}} \approx 13.2 \tag{5.8}$$

This means, when looking at silicon nanoparticles one obtains an over 13 times better contrast compared to silica particles of the same size.
However, free choice of particle material is not always available. iSCAT microscopy is commonly used to detect proteins [147, 148], viruses [135, 149] or lipids [150, 151], where the choice of parameters is very limited.

The image obtained by iSCAT microscopy is not a true and accurate depiction of the sample. For larger particles the basic detection principle in (fluorescence-free) microscopy is to look at the optical shadow cast by the object in question. The shape and size of the shadow resemble the object but scaled, and the darkness of the shadow depends on the objects' transparency. However, for sub-wavelength particles this changes as the shadow collapses to the point-spread function (PSF)

of the microscope [141]. The PSF of an optical system is the three-dimensional image of a point source. Light emitted from this point source, e.g. a sub-wavelength particle, is collected by a lens or objective. The optical element focuses part of the light to a point in the image plane. Different light waves converge and interfere at the focal point, as the lens or objective cannot focus the light infinitesimally small. The resulting diffraction pattern consists of a bright disk in the center, surrounded by concentric rings. The area of the so-called *Airy disk* is defined by the Numerical Aperture (NA) of the optical element. Conversely, one can determine the resolution by measuring the size of the disk. As can be seen in Figure 38, high NA results in clear pictures as the resolution of the image is increased, whereas low NA leads to worse imaging. Next to the images the intensity is plotted against spacial positioning. The bright Airy disk, as well as the concentric rings around it, correspond to peaks in the intensity distribution. Lower NA, i.e. a larger Airy disk, naturally leads to an intensity distribution with a higher full-width at half maximum (FWHM). Additionally, the size of the PSF scales with the wavelength of the light, i.e. the shorter the wavelength, the smaller the PSF and therefore the better is the resolution [152].
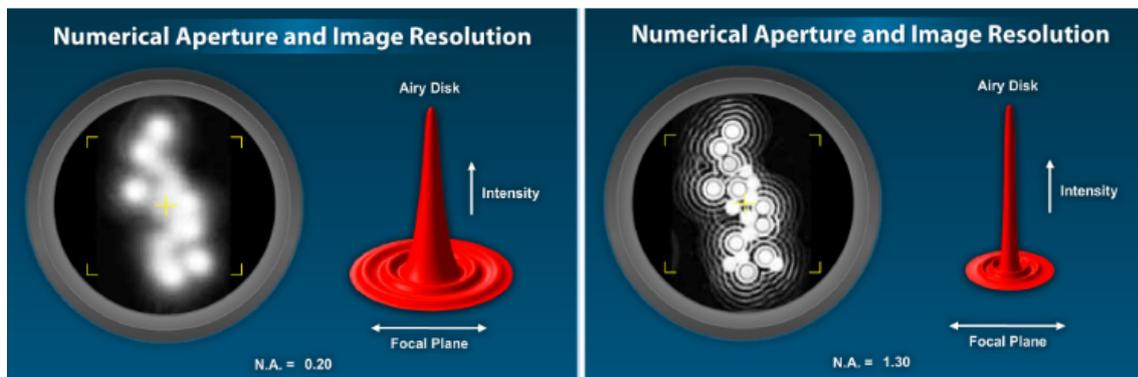
Figure 38: The Numerical Aperture of the optical system determines the resolution power and the size of the Airy disk. **Left image**: Low NA results in a large PSF, i.e. worse resolution and a blurry picture. **Right Image**: Higher NA reduces the size of the Airy disk and thus increases the resolution of the image. Created at [153].
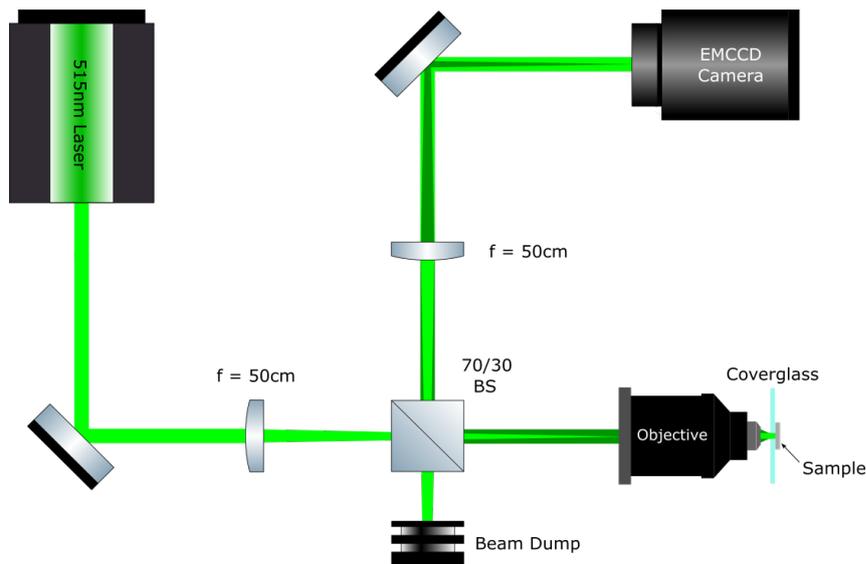
Figure 39: Schematic setup for a basic iSCAT microscope. A 515 nm continuous-wave laser is focused on the back focal plane of a microscope objective. Part of the beam is reflected at the coverglass surface (light green) or scattered off the sample (dark green). The light is recollected by the objective and sent back to an *Andor iXon* EMCCD camera. A second lens collimates the reflected beam and focuses the scattered light onto the camera. A beam splitter with 70 % reflectance is inserted into the setup to separate the imaging arm from the incident one. A beam dump collects the light that is reflected away from the setup by the beam splitter.

5.3 Optical setup

The schematic setup for basic iSCAT microscopy can be seen in Figure 39. According to Abbe's diffraction limit formula

$$d = \frac{\lambda}{2\text{NA}},$$ (5.9)

where NA denotes the Numerical Aperture of the system, the choice of laser wavelength and objective dictates the minimal distance resolvable by the built microscope and is therefore crucial when planning the setup. Furthermore, the choice of wavelength influences the polarizability of the nanoparticles, as the index of refraction is wavelength dependent. Another factor one has to account for, is the thickness of the coverglass and the spherical aberration that comes with it. Luckily, there are microscope objectives with built-in aberration correction.

In this experiment a 515 nm continuous-wave laser and the same three different microscope objectives as in chapter 4 are used: A 20x/0.4 NA[12] and a 40x/0.9 NA[13]

---

[12]Zeiss LD Plan-Neofluar 20x/0,4 Korr Ph2 M27
[13]Zeiss EC "Plan-Neofluar" 40x/0,9 Pol M27

both with coverslip correction and a 63x/0.95 NA[14] without aberration correction. Their working distances are 7.9 mm, 0.41 mm and 0.17 mm respectively. Even the smallest of the working distances is large enough to allow us to look at both, the bulk silicon sample and the cover slip that collects the nanoparticles produced by fs-laser desorption. Additionally, due to the absence of an immersion medium, the coverglass does not have to be cleaned if one wants to do electron microscopy, thus minimizing the risk of loosing the particles.

As can be seen in Figure 39, the laser is focused on the back focal plane of the microscope objective, such that a collimated beam hits the cover slip. Part of the light is scattered by the particles on the cover slip or at the silicon sample (dark green), and another part is reflected at the coverglass (light green). The second lens focuses the scattered light on to the CCD-camera and collimates the reflected light. The beam splitter between the lenses should have high reflectance and low transmittance and be placed such that the light coming from the laser is reflected into the beam block. While this means that only a fraction of the incident laser power illuminates the sample, it ensures that minimal signal is lost on the way back as most of the light is reflected towards the second lens. Furthermore, the beam splitter should be anti-reflection (AR) coated and/or wedged to reduce fringe and ghosting effects. Ghost images are copies of the original image shifted in position but interfere with the primary image. These ghost replicas arise due to reflection at the back-side of the beam splitter. For a wedged beam splitter however, the reflections of the front and back surfaces are anti–parallel and no interference artifacts arise [154].

In order to image both the bulk-silicon sample and specimen on the cover slip, as well as to form nanoparticle patterns, the coverglass is mounted on a 3D-translation stage. For fine-tuning, all axes can be driven by a piezoelectric motor. For focus finding this is especially important. For one, to obtain useful iSCAT data is crucial to find the correct focal point and, moreover, maintain a stable position over time. Any libration of the sample will result in a broadened point-spread function and thus to a worse data.
On the other hand, we can also use iSCAT microscopy to optimize the focus for fs-laser desorption of silicon (see chapter 4). In this configuration, the spot of the focused beam of the 515 nm fs-laser in perfect focus is roughly 650 nm in diameter. Any deviation from the focal point will result in a significant increase in spot size, thus directly impacting the nanoparticle creation process. Ramifications can range from altering the particle size to deformation or not producing particles at all.

---

[14]Zeiss "Achroplan" 63x/0,95 D=0 M27

Again, a stable setup is crucial. While for iSCAT microscopy maintaining position over a long time is more important, for fs-laser desorption reproducibility is key, thus necessitating spacial stability. This makes vibration isolation essential. However, the impact on the system can be minimized by optimizing the focus to begin with.

For our initial tests we used a 3D translation stage[15] with 4 mm travel range and $5\,\mu m$ step size to move the coverslip and sample around. For precise focus control we additionally use the included piezoelectric actuator with a travel range of $20\,\mu m$ and theoretical step size of 5 nm in z-direction.

Figures 40 and 41 show typical iSCAT images pre- and post-processing, respectively. Figure 40 is an image of a 50 nm silicon-on-insulator waver after irradiation by the fs-desorption laser, taken with the 40x/0.9 NA objective. The craters are approximately $1\,\mu$m in diameter and were produced by single laser pulses which were shot equally spaced $10\,\mu$m apart.
While the impact zones on the wafer are easily resolvable with the simple signal, the collected particles are harder to detect due to their smaller size. However, we can enhance the interference term by subtracting the background signal, which is acquired before deposition of the particles. Such a background corrected image can be seen in Figure 41. This picture was taken with the 20x/0.4 NA objective.
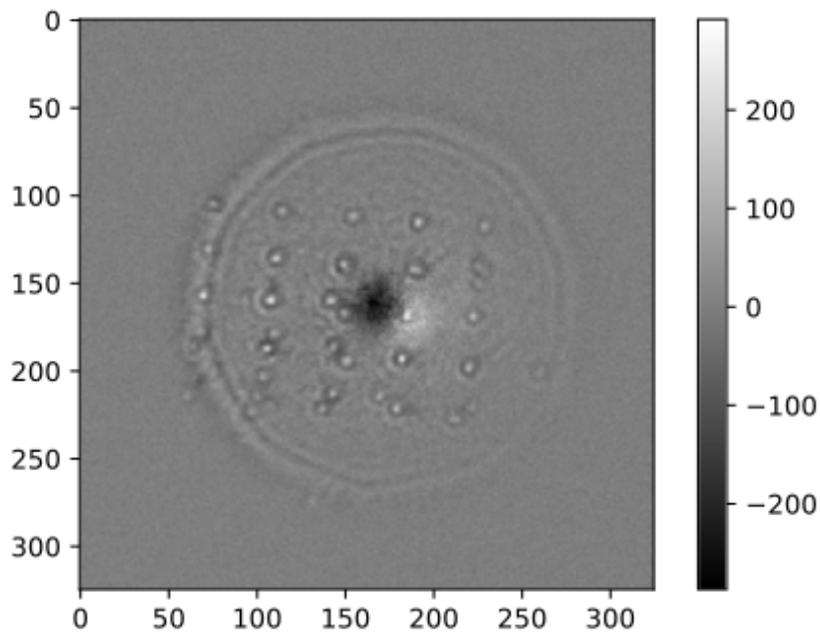
---

[15]Thorlabs Max 381/M
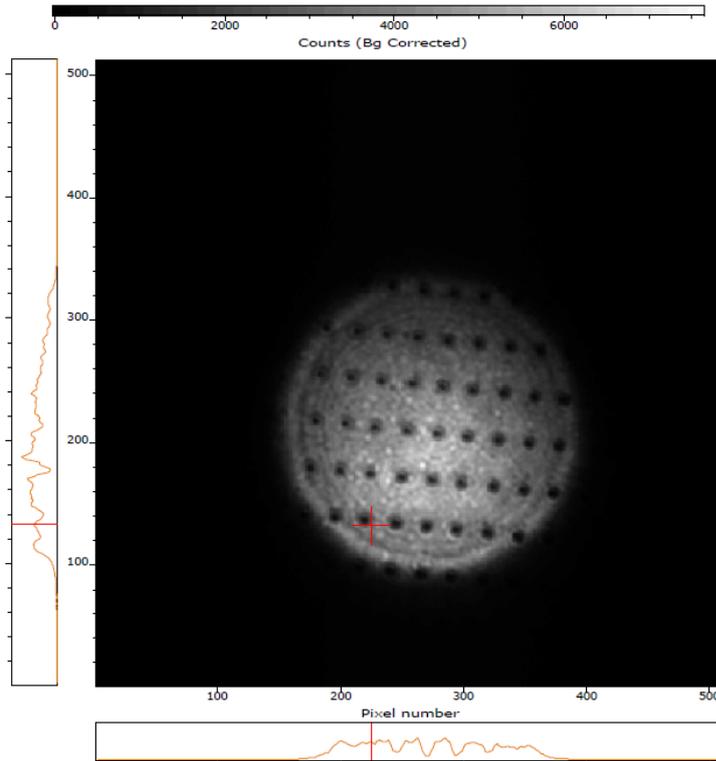
Figure 40: Real-time iSCAT image of the impact zone on a 50 nm silicon-on-insulator (SOI) wafer after irradiation with a 515 nm, 257 fs laser. Every crater corresponds to a single laser shot.

Figure 41: Background-corrected iSCAT image of nanoparticles created by fs-laser desorption.

6 Outlook: Laser printing of silicon nanoparticles as a source for cavity optomechanics

In this chapter we present a setup to test the viability of laser printing of nanoparticles as a novel source for levitated optomechanics. We combine the techniques presented in chapters 4 and 5 with a high-finesse optical cavity in a UHV-compatible configuration.

We have already established that laser printing of silicon nanoparticles allows for precise control over particle size and that they can be accurately deposited in arbitrary patterns - at least up to a distance of $\sim 15\,\mu$m. There are two main questions we want to answer in this preliminary setup. Firstly, we want to characterize the velocity distribution of the particles produced by fs-laser desorption. Secondly, we are interested in what the maximum possible distance between sample and optical trap can be, in order to still be able to capture the particle, i.e. how large the angular spread of the particles is.

Vacuum compatibility

To start we want to test the principal at ambient pressure and then, if successful, gradually go to ultra-high vacuum. Since all previous tests were done outside a vacuum chamber, we had to make some key adjustments in order to be able to transfer the setup into the chamber. The main challenge was to implement a cavity block into our previous setup, while simultaneously making the whole configuration more compact and vacuum compatible.

In a first step we exchanged the microscope objective for an aspheric lens. The main problem with our previously used objectives is their vacuum non-compatibility, since they strongly 'gas out', instantly compromising the vacuum. On the other hand, the limited working distances of high-NA aspheric lenses poses another constraint on the configuration. To accommodate the limited WD, we directly implement the lens into the cavity block. However, this comes at the detriment of being able to change the distance between cavity waist and particle donor sample. Ultimately we decided on a 0.5 NA, 4.9 mm working distance lens[16].

---

[16]LightPath 353252, precision molded aspheric lens, 6,33 mm diameter

The second big upgrade was to switch from the bulky *NanoMax* 3D translation stage to a compact vacuum compatible one (SmarAct XYZ DLS-5252). Every linear stage combines a stick-slip drive with a piezo scanner in a single device, allowing for precise position of the sample in a large area. This state-of-the-art assembly combines the best of two technologies: it uses the large travel range of the stick-slip drive (21 mm) and compensates its limited resolution with a smooth piezo stack (down to 0.5 nm in a closed loop configuration), which on the other hand would be limited in their travel range if used on their own. In reality we are limited by position readout which we estimate to be ∼ 1 nm in every direction.

Cavity design

The cavity design is based on plano-concave mirrors with radii of curvature of $R_C = 10$ cm, diameter of 12.7 mm and thickness of 4 mm. On the concave side they are coated with a highly reflective layer based on Bragg reflection with a target transmission of 5 ppm at 1560 nm. Additionally, the mirrors are anti-reflection coated on the planar side. These mirrors were used in previous cavity cooling experiments [62] and are measured to provide cavities with a finesse up to 300000.
To start, we want a cavity with deliberately larger beam waist to increase the chance to detect a particle. With given mirror radii of curvature R_c (and center wavelength λ, defined by the mirror coating), the waist of a symmetrical cavity only depends on the length of the cavity L:

$$w_0 = \sqrt{\frac{\lambda}{2\pi}\sqrt{L\left(2R_c - L\right)}}. \tag{6.1}$$

We recall from the stability criterion from chapter 2.3.1 as $0 \leq L \leq 2R_c$. The largest waist is achieved for a *confocal* cavity, i.e. $L \approx R_c$, and quickly declines towards $L = 0, 2R_c$. While a confocal cavity would imply the highest chance of detecting a particle, a larger beam waist also implies weaker interaction with light field. In the end, we decided on a cavity length $L = 15$ mm. This forms a beam with minimum waist $w_0 \approx 114 \, \mu$m.

Optical setup

To test the viability of laser printing of nanoparticles as a source for cavity optomechanics we designed and built a new setup. It incorporates the laser desorption, iSCAT microscopy as well as cavity system. The optical setup is split in two levels which can be seen in Figure 42. On the bottom level we arranged the fs-laser and iSCAT laser optics. Similar to the setup described in chapter 4, the fs-laser

is attenuated by a set of variable and fixed-value neutral density filter (V-ND and S-ND) and then simply directed at the sample via a 45° degree mirror (V-M). The iSCAT optics are also similar to what is described in chapter 5, but we swapped the lenses for ones with focal length of $f = 1\,\mathrm{m}$ to account for the bulkier setup. The paths of the two lasers are superimposed by a polarizing beam splitter (PBS) right before the 45° degree mirror. We use an AR-coated window at the bottom of the vacuum chamber to minimize unwanted reflection and signal loss. Additionally, it is slightly tilted such that any residual reflection off the window is directed away from the EMCCD camera as it would otherwise whitewash the scattering signal.

On the top level we arranged the cavity optics. We use a 1550 nm center frequency laser[17] that is directly coupled into a single-mode fiber. At the start we split off half of the beam (BS1) for heterodyne detection (detector D_3). The frequency of this part is altered by an acousto-optical modulator (AOM) which is driven by a frequency generator (FG) at 200 MHz and serves as the local oscillator. The other part of the beam is coupled out of the fiber (FC1)[18] to a beam with diameter 2.15 mm, focused by a lens with a focal length of $f = 25\,\mathrm{cm}$ and sent towards the cavity. We use the back-reflected light off the cavity for side-of-fringe locking (detector D_1). A circulator (C) assures that no light is reflected back towards the laser. The light transmitted through the cavity is collimated by a second lens, coupled back into the fiber (FC2) and superimposed (BS2) with the local oscillator beam. Furthermore, we detect the light scattered off a particle inside the cavity (detector D_2) as described in chapter 2.3.4.

Vacuum setup

A 3D rendered image of the vacuum setup can be seen in Figure 43a. The configuration is mounted on a support structure consisting of an aluminium breadboard which in turn sits on three aluminium pillars that are screwed into the base plate of the vacuum chamber. In principle, the setup can be split into two mechanical parts: the sample and the cavity setup.

Firstly, the sample holder (SH) is mounted on the 3D vacuum compatible translation stage. The sample holder is made of stainless steel and consists of a fixed supporting structure and a movable fork where the sample can be clamped in between (Figure 43b).

The stainless steel cavity block (CB) is responsible for securing the cavity mirrors

---

[17]Toptica CTL 1550
[18]Thorlabs F220 SMA-1550
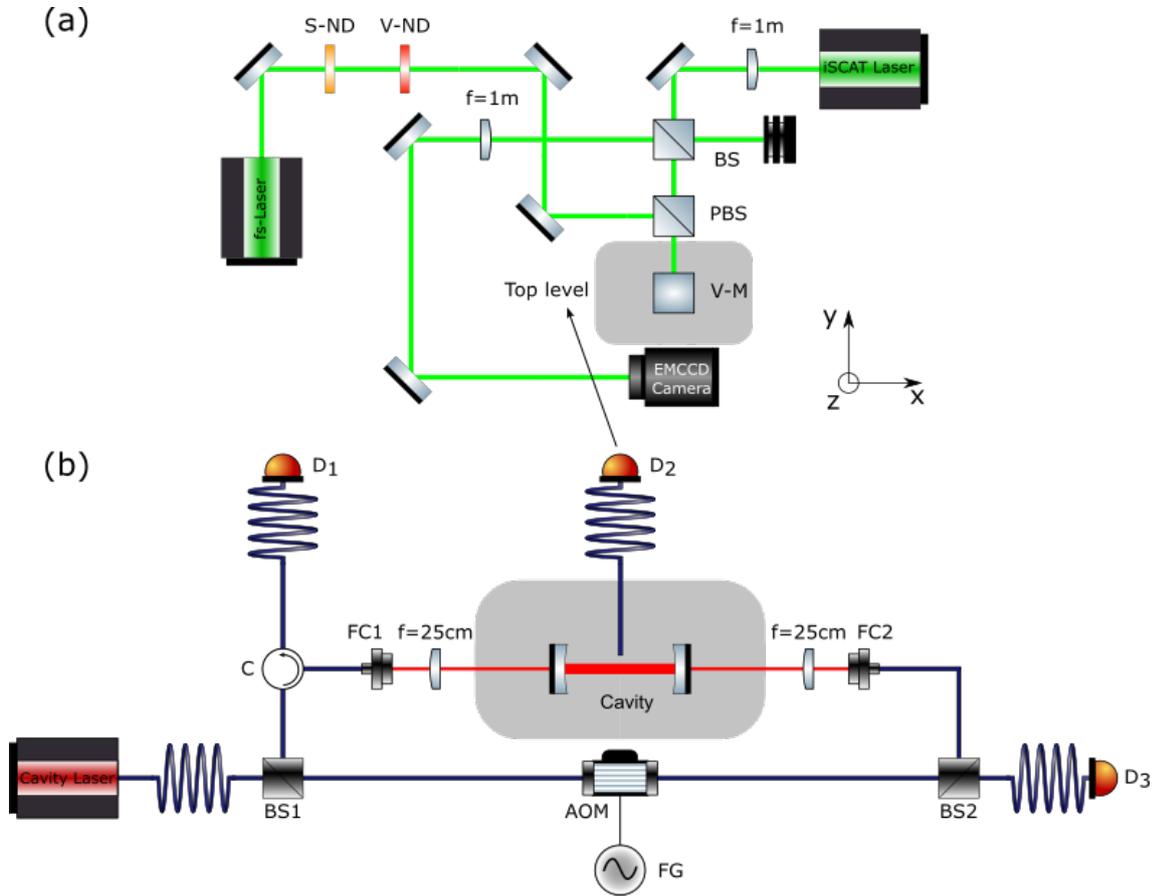
Figure 42: The optical setup consists of two level, bottom and top layer. **(a)** Bottom level: The fs-laser is attenuated by a set of variable and fixed-value neutral density filter (V-ND and S-ND) and guided towards a 45° degree mirror (V-M) that directs the beam upwards. The iSCAT laser is superimposed with the fs-laser at a polarizing beam splitter (PBS) and also directed upwards via V-M. The beam splitter BS (70/30 reflection/transmission) redirects part of the scattered signal towards an EMCCD camera. Two lenses with focal length $f = 1\,\mathrm{m}$ are used to focus and collimate the beam. **(b)** Top level: Arrangement of the cavity optics. The 1550 nm cavity laser is directly coupled into a single-mode fiber. Part of the beam is split off at a fiber beam splitter (BS1) and used for heterodyne detection. This local oscillator is frequency modulated by an acousto-optical modulator (AOM), which is driven by a frequency generator (FG) at 200 MHz. The other part is coupled out of the fiber (FC1), focused by a lens with a focal length of $f = 25\,\mathrm{cm}$ and sent towards the cavity. A circulator (C) assures that no light is reflected back towards the laser. The light transmitted through the cavity is collimated by a second lens, coupled back into the fiber (FC2) and superimposed (BS2) with the local oscillator beam. Detector D_1 is used for side-of-fringe locking, detector D_2 for scattered light detection and detector D_3 for heterodyne detection.

(M) in fixed positions as well as holding the focusing lens for the fs-laser. The block is placed on a viton sheet (V) for vibration isolation. A detailed cross-section of the cavity block can be seen in Figure 43c. The mirrors are fixated by bars which are screwed directly into the cavity block at fixed positions. Steps on either side of the block give additional support to the mirror and make for easier adjustment. The aspheric lens is directly implemented and can be screwed tight from the side.

Secondly, the cavity laser (red) and fs-laser (green) are portrayed disproportional for illustration purposes. The fs-laser is focused by an aspheric lens which is placed inside of the cavity block. It is screwed tight from the side and we only move the sample during the experiment. The recess in the cavity block is placed such that the center of the fs-laser beam coarsely coincides with the cavity beam waist. Fine tuning of the alignment is done with the mirrors outside the vacuum chamber. Good alignment is critical, as we want the particles to enter the cavity light field as close to the waist as possible to achieve maximum cooling forces.

We use a multi-mode fiber for scattered light detection. It is glued into a stainless steel tube (FT), which can be moved in three dimensions by an assembly of translation stages outside the vacuum chamber. We move the tip of the fiber as close to the cavity beam waist as possible to have achieve maximum detection efficiency. The other end of the fiber is connected to a photodiode.

Velocity estimation

We can approximate the velocity of the generated particles by first estimating their initial temperature. This can be easily done via

$$\Delta T = \frac{\Delta E}{m \cdot c}, \tag{6.2}$$

where ΔT is the temperature increase induced by the energy deposit ΔE, and m and c are the mass and specific heat capacity of the particle, respectively. Let us do the estimation for the 180 nm diameter particle created by a pulse with 1.9 nJ (see chapter 4). Taking the density and specific heat capacity of silicon from [155], we end up with a temperature increase of $\Delta T = 380000$ K. Clearly, this number is heavily inflated (the boiling point of silicon is $T_b = 3538$ K [155]), as not the entire energy will be deposited on the will-be particle material. For one, the polished silicon surface reflects $\sim 40\%$ of the incoming light [156]. Additionally, some energy will be absorbed by the silicon dioxide insulating layer. Furthermore, we observe melting areas with a diameter around $1\,\mu$m. For our 50 nm SOI wafer this corresponds to a ten times higher volume than that of the resulting particle.

Moser et al. [122] estimate the material temperature depending on the intensity.
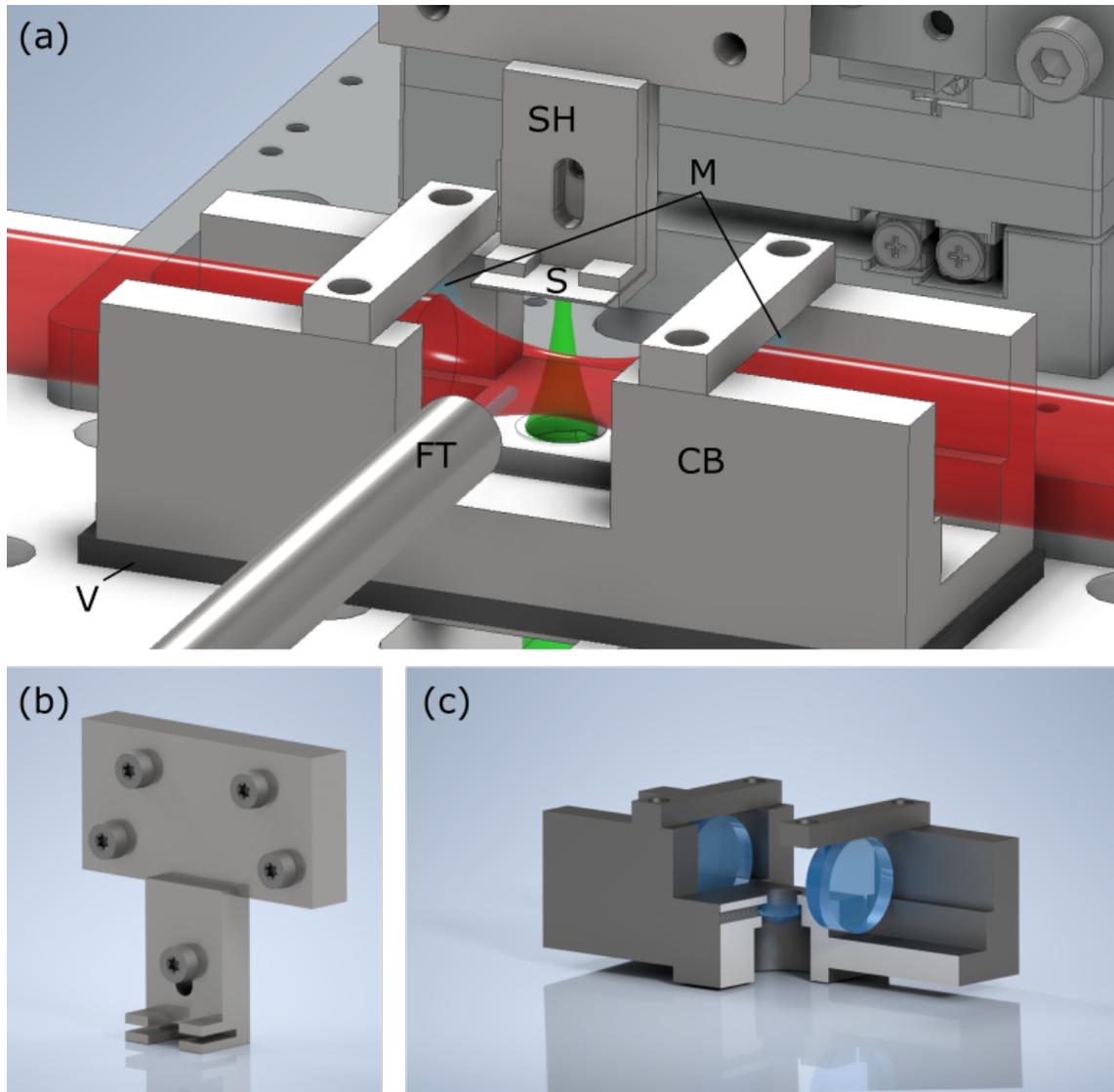
Figure 43: 3D images of the vacuum setup. **(a)** A sample holder (SH) is mounted on a 3D vacuum compatible translation stage and allows for samples (S) of different sizes to be mounted. The stainless steel cavity block (CB) is responsible for securing the cavity mirrors (M) in fixed positions as well as holding the focusing lens for the fs-laser. The block is placed on a viton sheet (V) for vibration isolation. The cavity laser (red) and fs-laser (green) are portrayed disproportional for illustration purposes. **(b)** Detailed image of the sample holder. It consists of a fixed supporting structure and a movable fork where the sample can be clamped in between. **(c)** Cross section of the cavity block. The mirrors are fixated by two bars that can be screwed into the main block. Steps on either side of the block give additional support to the mirror and make for easier adjustment. The aspheric lens is directly implemented and can be screwed tight from the side.

The particle was created with the 0.95 NA microscope objective, so if we assume a diffraction limited focal spot, we end up with $\sim 3\,\mathrm{J/cm^2}$. As expected, this puts us right into the middle fluence regime. The maximum temperature of the material can then be approximated to $3800 - 4500\,\mathrm{K}$. This indicates that the top of the sample evaporates and that the colder material below forms the particle. Therefore, less than $\sim 1/100$ of the laser energy is transferred to the actual particle in the end.

We assume the main energy loss in free flight to be attributed to black-body radiation:

$$P = A\sigma \left(T_1^4 - T_0^4 \right), \tag{6.3}$$

where P is the net radiated power, A is the surface area of the particle, σ is the Stefan-Boltzmann-constant and T_1 and T_0 are the temperatures of the particle and the environment, respectively. From experience, we estimate that the particle regains a solid state after $\sim 7\,\mu\mathrm{m}$ (melting temperature of silicon is $T_m = 1683\,\mathrm{K}$ [155]). Using equation 6.2 to calculate the minimum energy the particle has to radiate off to cool to T_m, and equation 6.3 to calculate the time it takes the particle to do so, we estimate a mean particle forward velocity between $v = 0.3\,\mathrm{m/s}$ and $v = 0.5\,\mathrm{m/s}$.

In chapter 3 we estimated a maximum velocity of $v_{\mathrm{max}} = 0.8$ in order to be able to trap a $150\,\mathrm{nm}$ silicon particle in a cavity with similar finesse but with a waist of $w_0 = 65\,\mu\mathrm{m}$. Considering that such a configuration would indeed be more suitable for proper cooling experiments, the comparison is reasonable.

Conclusion

We can conclude, that laser printing of nanoparticles is an intriguing prospect as a source for levitated optomechanics. We were able to confirm that printing of nanoparticle is a precise and reliable method to create nanoparticles. The in-situ creation of single particles comes with an inherit heraldity and the ability to print various materials stands out when compared to conventional methods. Silicon nanoparticles are of especial interest due to their stronger interaction with light with respect to commonly used silica particles. Furthermore, the ability to quickly and precisely manipulate the particle size is novel to levitated optomechanics sources.

An estimation of the forward velocity of the particles indicates that this method would be operable directly in ultra-high vacuum. However, we still need experimental confirmation of that, as well as whether or not particles can be precisely deposited over a larger distance. We presented a detailed setup with the ability of providing answers to these questions and can be easily adapted to a configuration

capable of advanced cavity cooling experiments.

References

[1]   Johannes Kepler. *De Cometis libelli tres... Autore Iohanne Keplero... (Carmen J. Tanckii)*. Typis Andreae Apergeri, 1619.

[2]   James Clerk Maxwell. *A Treatise on Electricity and Magnetism*. Oxford, Clarendon Press, 1873.

[3]   Peter Lebedew. "Untersuchungen über die Druckkräfte des Lichtes". In: *Annalen der Physik* 311.11 (1901), pp. 433–458. DOI: 10.1002/andp.19013111102.

[4]   E. F. Nichols and G. F. Hull. "A Preliminary Communication on the Pressure of Heat and Light Radiation". In: *Phys. Rev. (Series I)* 13 (5 Nov. 1901), pp. 307–320. DOI: 10.1103/PhysRevSeriesI.13.307.

[5]   Max Planck. "Ueber das Gesetz der Energieverteilung im Normalspectrum". In: *Annalen der Physik* 309.3 (1901), pp. 553–563. DOI: 10.1002/andp.19013090310.

[6]   A. Einstein. "Über einen die Erzeugung und Verwandlung des Lichtes betreffenden heuristischen Gesichtspunkt". In: *Annalen der Physik* 322.6 (1905), pp. 132–148. DOI: 10.1002/andp.19053220607.

[7]   Albert Einstein. "Entwicklung unserer Anschauungen über das Wesen und die Konstitution der Strahlung". In: *Physikalische Zeitschrift* 10 (1909), pp. 817–825. DOI: 10.1002/phbl.19690250902.

[8]   A. Ashkin. "Acceleration and Trapping of Particles by Radiation Pressure". In: *Phys. Rev. Lett.* 24 (4 Jan. 1970), pp. 156–159. DOI: 10.1103/PhysRevLett.24.156.

[9]   A. Ashkin and J. M. Dziedzic. "Optical Levitation by Radiation Pressure". In: *Applied Physics Letters* 19.8 (1971), pp. 283–285. DOI: 10.1063/1.1653919.

[10] A. Ashkin and J. M. Dziedzic. "Optical levitation in high vacuum". In: *Applied Physics Letters* 28.6 (1976), pp. 333–335. DOI: 10.1063/1.88748.

[11] T.W. Hänsch and A.L. Schawlow. "Cooling of gases by laser radiation". In: *Optics Communications* 13.1 (1975), pp. 68–69. ISSN: 0030-4018. DOI: https://doi.org/10.1016/0030-4018(75)90159-5.

[12] A. Ashkin. "Trapping of Atoms by Resonance Radiation Pressure". In: *Phys. Rev. Lett.* 40 (12 Mar. 1978), pp. 729–732. DOI: 10.1103/PhysRevLett.40.729.

[13] D. J. Wineland, R. E. Drullinger, and F. L. Walls. "Radiation-Pressure Cooling of Bound Resonant Absorbers". In: *Phys. Rev. Lett.* 40 (25 June 1978), pp. 1639–1642. DOI: 10.1103/PhysRevLett.40.1639.

[14] Markus Aspelmeyer, Tobias J. Kippenberg, and Florian Marquardt. "Cavity optomechanics". In: *Rev. Mod. Phys.* 86 (4 Dec. 2014), pp. 1391–1452. DOI: 10.1103/RevModPhys.86.1391.

[15] A. Ashkin and J. Gordon. "Stability of radiation-pressure particle traps: an optical Earnshaw theorem". In: *Opt. Lett.* 8 (1983), pp. 511–513.

[16] P. Zemánek et al. "Optical trapping of Rayleigh particles using a Gaussian standing wave". In: *Optics Communications* 151.4 (1998), pp. 273–285. ISSN: 0030-4018. DOI: https://doi.org/10.1016/S0030-4018(98)00093-5.

[17] P. Zemánek et al. "Optical trapping of nanoparticles and microparticles by a Gaussian standing wave". In: *Opt. Lett.* 24 (1999), pp. 1448–1450.

[18] A. Ashkin et al. "Observation of a single-beam gradient force optical trap for dielectric particles". In: *Opt. Lett.* 11 (1986), pp. 288–290.

[19] A Ashkin and JM Dziedzic. "Optical trapping and manipulation of viruses and bacteria". In: *Science* 235.4795 (1987), pp. 1517–1520. ISSN: 0036-8075. DOI: 10.1126/science.3547653.

[20] Steven M. Block, David F. Blair, and Howard C. Berg. "Compliance of bacterial flagella measured with optical tweezers". In: *Nature* 338.6215 (Apr. 1989), pp. 514–518. ISSN: 1476-4687. DOI: 10.1038/338514a0.

[21] Steven M. Block, Lawrence S. B. Goldstein, and Bruce J. Schnapp. "Bead movement by single kinesin molecules studied with optical tweezers". In: *Nature* 348.6299 (Nov. 1990), pp. 348–352. ISSN: 1476-4687. DOI: 10.1038/348348a0.

[22] A. Ashkin, J. M. Dziedzic, and T. Yamane. "Optical trapping and manipulation of single cells using infrared laser beams". In: *Nature* 330.6150 (Dec. 1987), pp. 769–771. ISSN: 1476-4687. DOI: 10.1038/330769a0.

[23] A. Ashkin. "History of optical trapping and manipulation of small-neutral particle, atoms, and molecules". In: *IEEE Journal of Selected Topics in Quantum Electronics* 6.6 (Nov. 2000), pp. 841–856. ISSN: 1558-4542. DOI: 10.1109/2944.902132.

[24] A. Perot and Charles Fabry. "On the Application of Interference Phenomena to the Solution of Various Problems of Spectroscopy and Metrology". In: *Astrophysical Journal* 9 (1899), p. 87. DOI: 10.1086/140557.

[25] Orazio Svelto. *Principle of Lasers*. Springer US, 2010.

[26]   A. Araya et al. "Optical mode cleaner with suspended mirrors". In: *Appl. Opt.* 36 (1997), pp. 1446–1453.

[27]   J. Hahn et al. "Cavity ringdown spectroscopy with a continuous-wave laser: calculation of coupling efficiency and a new spectrometer design". In: *Appl. Opt.* 38 (1999), pp. 1859–1866.

[28]   B P Abbott et al. "LIGO: the Laser Interferometer Gravitational-Wave Observatory". In: *Reports on Progress in Physics* 72.7 (June 2009), p. 076901. DOI: 10.1088/0034-4885/72/7/076901.

[29]   Asimina Arvanitaki and Andrew A. Geraci. "Detecting High-Frequency Gravitational Waves with Optically Levitated Sensors". In: *Phys. Rev. Lett.* 110 (7 Feb. 2013), p. 071105. DOI: 10.1103/PhysRevLett.110.071105.

[30]   T Akutsu et al. "Construction of KAGRA: an underground gravitational-wave observatory". In: *Progress of Theoretical and Experimental Physics* 2018.1 (Jan. 2018). 013F01. ISSN: 2050-3911. DOI: 10.1093/ptep/ptx180.

[31]   Peter Horak et al. "Cavity-Induced Atom Cooling in the Strong Coupling Regime". In: *Physical Review Letters* 79 (25 Dec. 1997), pp. 4974–4977. DOI: 10.1103/PhysRevLett.79.4974.

[32]   Vladan Vuletić and Steven Chu. "Laser Cooling of Atoms, Ions, or Molecules by Coherent Scattering". In: *Phys. Rev. Lett.* 84 (17 Apr. 2000), pp. 3787–3790. DOI: 10.1103/PhysRevLett.84.3787.

[33]   D. E. Chang et al. "Cavity opto-mechanics using an optically levitated nanosphere". In: *Proceedings of the National Academy of Sciences* 107.3 (2010), pp. 1005–1010. ISSN: 0027-8424. DOI: 10.1073/pnas.0912969107.

[34]   P. F. Barker and M. N. Shneider. "Cavity cooling of an optically trapped nanoparticle". In: *Phys. Rev. A* 81 (2 Feb. 2010), p. 023826. DOI: 10.1103/PhysRevA.81.023826.

[35]   Oriol Romero-Isart et al. "Toward quantum superposition of living organisms". In: *New Journal of Physics* 12.3 (Mar. 2010), p. 033015. DOI: 10.1088/1367-2630/12/3/033015.

[36]   James Millen et al. "Optomechanics with levitated particles". In: *Reports on Progress in Physics* 83.2 (Jan. 2020), p. 026401. DOI: 10.1088/1361-6633/ab6100.

[37]   Nikolai Kiesel et al. "Cavity cooling of an optically levitated submicron particle". In: *Proceedings of the National Academy of Sciences* 110.35 (2013), pp. 14180–14185. ISSN: 0027-8424. DOI: 10.1073/pnas.1309167110.

[38] Peter Asenbaum et al. "Cavity cooling of free silicon nanoparticles in high vacuum". In: *Nature Communications* 4 (Nov. 2013), p. 2743.

[39] Uroš Delić et al. "Cooling of a levitated nanoparticle to the motional quantum ground state". In: *Science* 367.6480 (Feb. 2020), p. 892. DOI: 10.1126/science.aba3993.

[40] David Grass. "Levitated optomechanics in vacuum using hollow core photonic crystal fibers and optical cavities". PhD thesis. University of Vienna, 2018.

[41] Jan Gieseler, Lukas Novotny, and Romain Quidant. "Thermal nonlinearities in a nanomechanical oscillator". In: *Nature Physics* 9.12 (Dec. 2013), pp. 806–810. ISSN: 1745-2481. DOI: 10.1038/nphys2798.

[42] Gambhir Ranjit et al. "Zeptonewton force sensing with nanospheres in an optical lattice". In: *Phys. Rev. A* 93 (5 May 2016), p. 053801. DOI: 10.1103/PhysRevA.93.053801.

[43] Stefan Kuhn et al. "Optically driven ultra-stable nanomechanical rotor". In: *Nature Communications* 8.1 (Nov. 2017), p. 1670. ISSN: 2041-1723.

[44] Jonghoon Ahn et al. "Optically Levitated Nanodumbbell Torsion Balance and GHz Nanomechanical Rotor". In: *Physical Review Letters* 121 (3 July 2018), p. 033603. DOI: 10.1103/PhysRevLett.121.033603.

[45] Joseph T. Verdeyen. *Laser Electronics*. 3rd edition. Prentice Hall, 1995.

[46] Bahaa E. A. Saleh and Malvin Carl Teich. "Beam Optics". In: *Fundamentals of Photonics*. John Wiley & Sons, Ltd, 2001. Chap. 3, pp. 80–107. ISBN: 9780471213741. DOI: 10.1002/0471213748.ch3.

[47] Nikolai Kiesel. "Quantum Optics I - An introduction to basic concepts, methods and milestone experiments". 2018.

[48] P. A. Maia Neto and H. M Nussenzveig. "Theory of optical tweezers". In: *Europhysics Letters (EPL)* 50.5 (June 2000), pp. 702–708. DOI: 10.1209/epl/i2000-00327-4.

[49] Alexander Rohrbach and Ernst H. K. Stelzer. "Trapping forces, force constants, and potential depths for dielectric spheres in the presence of spherical aberrations". In: *Appl. Opt.* 41 (2002), pp. 2494–2507.

[50] A. Ashkin. "Forces of a single-beam gradient laser trap on a dielectric sphere in the ray optics regime". In: *Biophysical Journal* 61.2 (1992), pp. 569–582. ISSN: 0006-3495. DOI: https://doi.org/10.1016/S0006-3495(92)81860-X.

[51] *Optical tweezers*. Wikipedia, The Free Encyclopedia. [Online; accessed 27-June-2020].

[52] W. H. Wright, G. J. Sonek, and M. W. Berns. "Parametric study of the forces on microspheres held by optical tweezers". In: *Appl. Opt.* 33 (1994), pp. 1735–1748.

[53] Tongcang Li. "Fundamental tests of physics with optically trapped microspheres". PhD thesis. University of Texas at Austin, 2011.

[54] Stefan Kuhn et al. "Full rotational control of levitated silicon nanorods". In: *Optica* 4.3 (Mar. 2017), pp. 356–360. DOI: 10.1364/OPTICA.4.000356.

[55] Yasuhiro Harada and Toshimitsu Asakura. "Radiation forces on a dielectric sphere in the Rayleigh scattering regime". In: *Optics Communications* 124.5 (1996), pp. 529–541. ISSN: 0030-4018. DOI: https://doi.org/10.1016/0030-4018(95)00753-9.

[56] Jan Gieseler. "Dynamics of optically levitated nanoparticles in high vacuum". PhD thesis. ICFO, 2014.

[57] Jan Gieseler et al. "Subkelvin Parametric Feedback Cooling of a Laser-Trapped Nanoparticle". In: *Phys. Rev. Lett.* 109 (10 Sept. 2012), p. 103603. DOI: 10.1103/PhysRevLett.109.103603.

[58] Jan Gieseler et al. "Subkelvin Parametric Feedback Cooling of a Laser-Trapped Nanoparticle - Supplementary Information". In: *Phys. Rev. Lett.* 109 (10 Sept. 2012), p. 103603. DOI: 10.1103/PhysRevLett.109.103603.

[59] Felix Tebbenjohanns et al. "Cold Damping of an Optically Levitated Nanoparticle to Microkelvin Temperatures". In: *Phys. Rev. Lett.* 122 (22 June 2019), p. 223601. DOI: 10.1103/PhysRevLett.122.223601.

[60] Tongcang Li, Simon Kheifets, and Mark G. Raizen. "Millikelvin cooling of an optically trapped microsphere in vacuum". In: *Nature Physics* 7.7 (July 2011), pp. 527–530. ISSN: 1745-2481. DOI: 10.1038/nphys1952.

[61] J. Millen et al. "Cavity Cooling a Single Charged Levitated Nanosphere". In: *Phys. Rev. Lett.* 114 (12 Mar. 2015), p. 123602. DOI: 10.1103/PhysRevLett.114.123602.

[62] Stefan Kuhn et al. "Cavity-Assisted Manipulation of Freely Rotating Silicon Nanorods in High Vacuum". In: *Nano Letters* 15.8 (2015). PMID: 26167662, pp. 5604–5608. DOI: 10.1021/acs.nanolett.5b02302.

[63] Uroš Delić et al. "Cavity Cooling of a Levitated Nanosphere by Coherent Scattering". In: *Phys. Rev. Lett.* 122 (12 Mar. 2019), p. 123602. DOI: 10.1103/PhysRevLett.122.123602.

[64] Uroš Delić. "Cavity cooling by coherent scattering of a levitated nanosphere in vacuum". PhD thesis. University of Vienna, 2019.

[65] Thomas Kessler et al. "A sub-40 mHz laser based on a silicon single-crystal optical cavity". In: *Precision Electromagnetic Measurements (CPEM), 2012 Conference on*. IEEE. 2012, pp. 272–273.

[66] Bahaa E. A. Saleh and Malvin Carl Teich. "Resonator Optics". In: *Fundamentals of Photonics*. John Wiley & Sons, Ltd, 2001. Chap. 9, pp. 310–341. ISBN: 9780471213741. DOI: 10.1002/0471213748.ch9.

[67] Thomas Salzburger and Helmut Ritsch. "Collective transverse cavity cooling of a dense molecular beam". In: *New Journal of Physics* 11.5 (May 2009), p. 055025. DOI: 10.1088/1367-2630/11/5/055025.

[68] Franz Ferdinand Wieser. "Towards optical cooling of silicon nanoparticles in a microcavity". MA thesis. University of Vienna, 2017.

[69] Peter Asenbaum. "Towards Cavity Cooling of a Molecular Beam". MA thesis. University of Vienna, 2009.

[70] Stefan Kuhn. "Cooling and manipulating the ro-translational motion of dielectric particles in high vacuum". PhD thesis. University of Vienna, 2017.

[71] Eric D. Black. "An introduction to Pound-Drever-Hall laser frequency stabilization". In: *American Journal of Physics* 69 (Jan. 2001), pp. 79–87. DOI: 10.1119/1.1286663.

[72] R. W. P. Drever et al. "Laser phase and frequency stabilization using an optical resonator". In: *Applied Physics B* 31.2 (June 1983), pp. 97–105. ISSN: 1432-0649. DOI: 10.1007/BF00702605.

[73] T.W. Hänsch and B. Couillaud. "Laser frequency stabilization by polarization spectroscopy of a reflecting reference cavity". In: *Optics Communications* 35.3 (1980), pp. 441–444. ISSN: 0030-4018. DOI: https://doi.org/10.1016/0030-4018(80)90069-3.

[74] Hans-A. Bachor and Timothy C. Ralph. "Classical Models of Light". In: *A Guide to Experiments in Quantum Optics*. John Wiley & Sons, Ltd, 2019. Chap. 2, pp. 19–64. ISBN: 9783527695805. DOI: 10.1002/9783527695805.ch2.

[75] Hans-A. Bachor and Timothy C. Ralph. "Quantum Noise: Basic Measurements and Techniques". In: *A Guide to Experiments in Quantum Optics*. John Wiley & Sons, Ltd, 2019. Chap. 8, pp. 269–301. ISBN: 9783527695805. DOI: 10.1002/9783527695805.ch8.

[76] Peter Asenbaum. "Cavity cooling of silicon nanoparticles in high-vacuum". PhD thesis. University of Vienna, 2014.

[77]   Pietro Vahramian. "Towards rotational levitated optomechanics in high vac-
        uum". MA thesis. University of Vienna, 2019.

[78]   Lukas Novotny and Bert Hecht. "Forces in confined fields". In: *Principles of
        Nano-Optics*. Cambridge University Press, 2006. Chap. 13, pp. 419–445. DOI:
        [10.1017/CBO9780511813535.014](10.1017/CBO9780511813535.014).

[79]   *Viskosität*. Lexikon der Physik. Spektrum Akademischer Verlag. [Online; ac-
        cessed 19-June-2020].

[80]   *piezoelektrischer Effekt*. Lexikon der Physik. Spektrum Akademischer Verlag.
        [Online; accessed 20-June-2020].

[81]   B.V Derjaguin, V.M Muller, and Yu.P Toporov. "Effect of contact defor-
        mations on the adhesion of particles". In: *Journal of Colloid and Interface
        Science* 53.2 (1975), pp. 314–326. ISSN: 0021-9797. DOI: [https://doi.org/
        10.1016/0021-9797(75)90018-1](https://doi.org/10.1016/0021-9797(75)90018-1).

[82]   V.M. Muller, B.V. Derjaguin, and Yu.P. Toporov. "On two methods of cal-
        culation of the force of sticking of an elastic sphere to a rigid plane". In:
        Colloids and Surfaces 7.3 (1983), pp. 251–259. ISSN: 0166-6622. DOI: [https:
        //doi.org/10.1016/0166-6622(83)80051-1](https://doi.org/10.1016/0166-6622(83)80051-1).

[83]   Lars-Oliver Heim et al. "Adhesion and Friction Forces between Spherical
        Micrometer-Sized Particles". In: *Phys. Rev. Lett.* 83 (16 Oct. 1999), pp. 3328–
        3331. DOI: 10.1103/PhysRevLett.83.3328.

[84]   Guido Violano, Giuseppe Pompeo Demelio, and Luciano Afferrante. "On the
        DMT adhesion theory: from the first studies to the modern applications in
        rough contacts". In: *Procedia Structural Integrity* 12 (2018). AIAS 2018 in-
        ternational conference on stress analysis, pp. 58–70. ISSN: 2452-3216. DOI:
        https://doi.org/10.1016/j.prostr.2018.11.106.

[85]   Matti Paajanen et al. "Experimental humidity dependency of small particle
        adhesion on silica and titania". In: *Journal of Colloid and Interface Science*
        304.2 (2006), pp. 518–523. ISSN: 0021-9797. DOI: [https://doi.org/10.
        1016/j.jcis.2006.09.017](https://doi.org/10.1016/j.jcis.2006.09.017).

[86]   M. D. Summers, D. R. Burnham, and D. McGloin. "Trapping solid aerosols
        with optical tweezers: A comparison between gas and liquid phase optical
        traps". In: *Opt. Express* 16.11 (May 2008), pp. 7739–7747. DOI: [10.1364/OE.
        16.007739](10.1364/OE.16.007739).

[87]   Arzu Ari. "Jet, Ultrasonic, and Mesh Nebulizers: An Evaluation of Nebulizers
        for Better Clinical Outcomes". In: *Euras J Pulm* 16 (May 2014), pp. 1–7. DOI:
        [10.5152/ejp.2014.00087](10.5152/ejp.2014.00087).

[88] Leslie Yeo et al. "Ultrasonic nebulization platforms for pulmonary drug delivery". In: *Expert opinion on drug delivery* 7 (June 2010), pp. 663–79. DOI: 10.1517/17425247.2010.485608.

[89] Pau Mestres et al. "Cooling and manipulation of a levitated nanoparticle with an optical fiber trap". In: *Applied Physics Letters* 107.15 (2015), p. 151102. DOI: 10.1063/1.4933180.

[90] Dmitry S. Bykov et al. "Direct loading of nanoparticles under high vacuum into a Paul trap for levitodynamical experiments". In: *Applied Physics Letters* 115.3 (2019), p. 034101. DOI: 10.1063/1.5109645.

[91] David Grass et al. "Optical trapping and control of nanoparticles inside evacuated hollow core photonic crystal fibers". In: *Applied Physics Letters* 108.22 (2016), p. 221103. DOI: 10.1063/1.4953025.

[92] Tomáš Čižmár et al. "Optical conveyor belt for delivery of submicron objects". In: *Applied Physics Letters* 86.17 (2005), p. 174101. DOI: 10.1063/1.1915543.

[93] T S Monteiro et al. "Dynamics of levitated nanospheres: towards the strong coupling regime". In: *New Journal of Physics* 15.1 (Jan. 2013), p. 015001. DOI: 10.1088/1367-2630/15/1/015001.

[94] J. Millen et al. "Nanoscale temperature measurements using non-equilibrium Brownian dynamics of a levitated nanosphere". In: *Nature Nanotechnology* 9.6 (June 2014), pp. 425–429. ISSN: 1748-3395. DOI: 10.1038/nnano.2014.82.

[95] V.V. Golovlev et al. "Laser-induced acoustic desorption". In: *International Journal of Mass Spectrometry and Ion Processes* 169-170 (1997). Matrix-Assisted Laser Desorption Ionization Mass Spectrometry, pp. 69–78. ISSN: 0168-1176. DOI: https://doi.org/10.1016/S0168-1176(97)00209-7.

[96] Uğur Sezer et al. "Laser-Induced Acoustic Desorption of Natural and Functionalized Biochromophores". In: *Analytical Chemistry* 87.11 (June 2015), pp. 5614–5619. ISSN: 0003-2700. DOI: 10.1021/acs.analchem.5b00601.

[97] Wen-Ping Peng et al. "Laser-Induced Acoustic Desorption Mass Spectrometry of Single Bioparticles". In: *Angewandte Chemie International Edition* 45.9 (2006), pp. 1423–1426. DOI: 10.1002/anie.200503271.

[98] Richard P. Feynman. *There's Plenty of Room at the Bottom*. Lecture at the annual American Physical Society meeting. Dec. 1959.

[99] Agnieszka Z. Wilczewska et al. "Nanoparticles as drug delivery systems". In: *Pharmacological Reports* 64.5 (2012), pp. 1020–1037. ISSN: 1734-1140. DOI: https://doi.org/10.1016/S1734-1140(12)70901-5.

[100]   David P. Cormode, Pratap C. Naha, and Zahi A. Fayad. "Nanoparticle contrast agents for computed tomography: a focus on micelles". In: *Contrast Media & Molecular Imaging* 9.1 (2014), pp. 37–52. DOI: 10.1002/cmmi.1551.

[101]   Eleonora Petryayeva and Ulrich J. Krull. "Localized surface plasmon resonance: Nanostructures, bioassays and biosensing—A review". In: *Analytica Chimica Acta* 706.1 (2011), pp. 8–24. ISSN: 0003-2670. DOI: https://doi.org/10.1016/j.aca.2011.08.020.

[102]   Kathryn M. Mayer and Jason H. Hafner. "Localized Surface Plasmon Resonance Sensors". In: *Chemical Reviews* 111.6 (June 2011), pp. 3828–3857. ISSN: 0009-2665. DOI: 10.1021/cr100313v.

[103]   A. Barchanski et al. "Laser Generation and Printing of Nanoparticles". In: *Fundamentals of Laser-Assisted Micro- and Nanotechnologies*. Ed. by Vadim P. Veiko and Vitaly I. Konov. Cham: Springer International Publishing, 2014. Chap. 5, pp. 103–123. ISBN: 978-3-319-05987-7. DOI: 10.1007/978-3-319-05987-7_5.

[104]   J.M. Fernández-Pradas et al. "Laser-induced forward transfer of biomolecules". In: *Thin Solid Films* 453-454 (2004). Proceedings of Symposium H on Photonic Processing of Surfaces, Thin Films and Devices, of the E-MRS 2003 Spring Conference, pp. 27–30. ISSN: 0040-6090. DOI: https://doi.org/10.1016/j.tsf.2003.11.154.

[105]   V. Dinca et al. "Patterning parameters for biomolecules microarrays constructed with nanosecond and femtosecond UV lasers". In: *Thin Solid Films* 516 (July 2008), pp. 6504–6511. DOI: 10.1016/j.tsf.2008.02.043.

[106]   Savas Tasoglu and Utkan Demirci. "Bioprinting for stem cell research". In: *Trends in Biotechnology* 31.1 (2013), pp. 10–19. ISSN: 0167-7799. DOI: https://doi.org/10.1016/j.tibtech.2012.10.005.

[107]   Jia Min Lee and Wai Yee Yeong. "Design and Printing Strategies in 3D Bioprinting of Cell-Hydrogels: A Review". In: *Advanced Healthcare Materials* 5.22 (2016), pp. 2856–2865. DOI: 10.1002/adhm.201600435.

[108]   Cyrille Norotte et al. "Scaffold-free vascular tissue engineering using bioprinting". In: *Biomaterials* 30.30 (2009), pp. 5910–5917. ISSN: 0142-9612. DOI: https://doi.org/10.1016/j.biomaterials.2009.06.034.

[109]   Lothar Koch et al. "Skin tissue generation by laser cell printing". In: *Biotechnology and Bioengineering* 109.7 (2012), pp. 1855–1863. DOI: 10.1002/bit.24455.

[110] Urs Zywietz et al. "Laser printing of silicon nanoparticles with resonant optical electric and magnetic responses". In: *Nature Communications* 5.1 (Mar. 2014), p. 3402. ISSN: 2041-1723. DOI: 10.1038/ncomms4402.

[111] Urs Zywietz et al. "Generation and patterning of Si nanoparticles by femtosecond laser pulses". In: *Applied Physics A* 114.1 (Jan. 2014), pp. 45–50. ISSN: 1432-0630. DOI: 10.1007/s00339-013-8007-6.

[112] A.I. Kuznetsov, J. Koch, and B.N. Chichkov. "Laser-induced backward transfer of gold nanodroplets". In: *Opt. Express* 17.21 (Oct. 2009), pp. 18820–18825. DOI: 10.1364/OE.17.018820.

[113] S. Barcikowski et al. "Properties of nanoparticles generated during femtosecond laser machining in air and water". In: *Applied Physics A* 87.1 (Apr. 2007), pp. 47–55. ISSN: 1432-0630. DOI: 10.1007/s00339-006-3852-1.

[114] Denis M. Zhigunov et al. "Femtosecond Laser Printing of Single Ge and SiGe Nanoparticles with Electric and Magnetic Optical Resonances". In: *ACS Photonics* 5.3 (2018), pp. 977–983. DOI: 10.1021/acsphotonics.7b01275.

[115] Sergey Makarov et al. "Resonant silicon nanoparticles with controllable crystalline states and nonlinear optical responses". In: *Nanoscale* 10 (24 2018), pp. 11403–11409. DOI: 10.1039/C8NR02057D.

[116] S. K. Sundaram and E. Mazur. "Inducing and probing non-thermal transitions in semiconductors using femtosecond laser pulses". In: *Nature Materials* 1.4 (Dec. 2002), pp. 217–224. ISSN: 1476-4660. DOI: 10.1038/nmat767.

[117] F. Korte, J. Koch, and B. N. Chichkov. "Formation of microbumps and nanojets on gold targets by femtosecond laser pulses". In: *Applied Physics A* 79.4 (Sept. 2004), pp. 879–881. ISSN: 1432-0630. DOI: 10.1007/s00339-004-2590-5.

[118] A. I. Kuznetsov, J. Koch, and B. N. Chichkov. "Nanostructuring of thin gold films by femtosecond lasers". In: *Applied Physics A* 94.2 (Feb. 2009), pp. 221–230. ISSN: 1432-0630. DOI: 10.1007/s00339-008-4859-6.

[119] Urs Zywietz et al. "Laser Printing of Nanoparticles". In: *Laser Printing of Functional Materials*. John Wiley & Sons, Ltd, 2018. Chap. 11, pp. 251–268. ISBN: 9783527805105. DOI: 10.1002/9783527805105.ch11.

[120] S.C. Hardy. "The surface tension of liquid silicon". In: *Journal of Crystal Growth* 69.2 (1984), pp. 456–460. ISSN: 0022-0248. DOI: https://doi.org/10.1016/0022-0248(84)90355-5.

[121] A. V. Shishkin and A. S. Basin. "Surface tension of liquid silicon". In: *Theoretical Foundations of Chemical Engineering* 38.6 (Nov. 2004), pp. 660–668. ISSN: 1608-3431. DOI: 10.1007/s11236-005-0043-2.

[122] Regina Moser et al. "Single pulse femtosecond laser ablation of silicon – a comparison between experimental and simulated two-dimensional ablation profiles". English. In: *Advanced Optical Technologies* 7.4 (2018), pp. 255–264.

[123] Yasushi Sako, Shigeru Minoghchi, and Toshio Yanagida. "Single-molecule imaging of EGFR signalling on the surface of living cells". In: *Nature Cell Biology* 2.3 (Mar. 2000), pp. 168–172. ISSN: 1476-4679. DOI: 10.1038/35004044.

[124] Ahmet Yildiz et al. "Myosin V Walks Hand-Over-Hand: Single Fluorophore Imaging with 1.5-nm Localization". In: *Science* 300.5628 (2003), pp. 2061–2065. ISSN: 0036-8075. DOI: 10.1126/science.1084398.

[125] Adam D. Douglass and Ronald D. Vale. "Single-Molecule Microscopy Reveals Plasma Membrane Microdomains Created by Protein-Protein Networks that Exclude or Trap Signaling Molecules in T Cells". In: *Cell* 121.6 (2005), pp. 937–950. ISSN: 0092-8674. DOI: https://doi.org/10.1016/j.cell.2005.04.009.

[126] Chia-Lung Hsieh. "Label-free, ultrasensitive, ultrahigh-speed scattering-based interferometric imaging". In: *Optics Communications* 422 (2018). Trends in Label-Free Imaging, pp. 69–74. ISSN: 0030-4018. DOI: https://doi.org/10.1016/j.optcom.2018.02.058.

[127] Xiaoyong Wang et al. "Non-blinking semiconductor nanocrystals". In: *Nature* 459.7247 (2009), pp. 686–689. ISSN: 1476-4687. DOI: 10.1038/nature08072.

[128] David Boyer et al. "Photothermal Imaging of Nanometer-Sized Metal Particles Among Scatterers". In: *Science* 297.5584 (2002), pp. 1160–1163. ISSN: 0036-8075. DOI: 10.1126/science.1073765.

[129] Sheldon Schultz et al. "Single-target molecule detection with nonbleaching multicolor optical immunolabels". In: *Proceedings of the National Academy of Sciences* 97.3 (2000), pp. 996–1001. ISSN: 0027-8424. DOI: 10.1073/pnas.97.3.996.

[130] C. Sönnichsen et al. "Spectroscopy of single metallic nanoparticles using total internal reflection microscopy". In: *Applied Physics Letters* 77.19 (2000), pp. 2949–2951. DOI: 10.1063/1.1323553.

[131] Gavin Young and Philipp Kukura. "Interferometric Scattering Microscopy". In: *Annual Review of Physical Chemistry* 70.1 (2019). PMID: 30978297, pp. 301–322. DOI: 10.1146/annurev-physchem-050317-021247.

[132] J. S. Batchelder and M. A. Taubenblatt. "Interferometric detection of forward scattered light from small particles". In: *Applied Physics Letters* 55.3 (1989), pp. 215–217. DOI: 10.1063/1.102268.

[133] L.A. Amos and W.B. Amos. "The bending of sliding microtubules imaged by confocal light microscopy and negative stain electron microscopy". In: *Journal of Cell Science* 1991.Supplement 14 (1991), pp. 95–101. ISSN: 0021-9533. DOI: 10.1242/jcs.1991.Supplement_14.20.

[134] K. Lindfors et al. "Detection and Spectroscopy of Gold Nanoparticles Using Supercontinuum White Light Confocal Microscopy". In: *Phys. Rev. Lett.* 93 (3 July 2004), p. 037401. DOI: 10.1103/PhysRevLett.93.037401.

[135] Philipp Kukura et al. "High-speed nanoscopic tracking of the position and orientation of a single virus". In: *Nature Methods* 6.12 (Dec. 2009), pp. 923–927. ISSN: 1548-7105. DOI: 10.1038/nmeth.1395.

[136] G. G. Daaboul et al. "High-Throughput Detection and Sizing of Individual Low-Index Nanoparticles and Viruses for Pathogen Identification". In: *Nano Letters* 10.11 (2010). PMID: 20964282, pp. 4727–4731. DOI: 10.1021/nl103210p.

[137] Takahisa Matsuzaki et al. "Quantitative Evaluation of Cancer Cell Adhesion to Self-Assembled Monolayer-Patterned Substrates by Reflection Interference Contrast Microscopy". In: *The Journal of Physical Chemistry B* 120.7 (2016). PMID: 26845066, pp. 1221–1227. DOI: 10.1021/acs.jpcb.5b11870.

[138] Mohammed Mahamdeh et al. "Label-free high-speed wide-field imaging of single microtubules using interference reflection microscopy". In: *Journal of Microscopy* 272.1 (2018), pp. 60–66. DOI: 10.1111/jmi.12744.

[139] Yuting Yang et al. "Interferometric plasmonic imaging and detection of single exosomes". In: *Proceedings of the National Academy of Sciences* 115.41 (2018), pp. 10275–10280. ISSN: 0027-8424. DOI: 10.1073/pnas.1804548115.

[140] Milan Delor et al. "Imaging material functionality through three-dimensional nanoscale tracking of energy flow". In: *Nature Materials* 19.1 (Jan. 2020), pp. 56–62. ISSN: 1476-4660. DOI: 10.1038/s41563-019-0498-x.

[141] Richard W. Taylor and Vahid Sandoghdar. "Interferometric Scattering (iS-CAT) Microscopy and Related Techniques". In: *Label-Free Super-Resolution Microscopy*. Ed. by Vasily Astratov. Cham: Springer International Publishing, 2019, pp. 25–65. ISBN: 978-3-030-21722-8. DOI: 10.1007/978-3-030-21722-8_2.

[142] C.R. Nave. *Reflection phase change*. Hyperphysics. Georgia State University. [Online; accessed 1-April-2020].

[143]   Bahaa E. A Saleh and Malvin Carl Teich. *Fundamentals of Photonics*. Wiley, 2007.

[144]   James Bateman et al. "Near-field interferometry of a free-falling nanoparticle from a point-like source". In: *Nature Communications* 5 (Sept. 2014), p. 4788.

[145]   D. E. Aspnes and A. A. Studna. "Dielectric functions and optical parameters of Si, Ge, GaP, GaAs, GaSb, InP, InAs, and InSb from 1.5 to 6.0 eV". In: *Phys. Rev. B* 27 (2 Jan. 1983), pp. 985–1009. DOI: 10.1103/PhysRevB.27.985.

[146]   I. H. Malitson. "Interspecimen Comparison of the Refractive Index of Fused Silica∗,†". In: *J. Opt. Soc. Am.* 55.10 (Oct. 1965), pp. 1205–1209. DOI: 10.1364/JOSA.55.001205.

[147]   J. Ortega Arroyo et al. "Label-Free, All-Optical Detection, Imaging, and Tracking of a Single Protein". In: *Nano Letters* 14.4 (2014). PMID: 24597479, pp. 2065–2070. DOI: 10.1021/nl500234t.

[148]   Marek Piliarik and Vahid Sandoghdar. "Direct optical sensing of single unlabelled proteins and super-resolution imaging of their binding sites". In: *Nature Communications* 5.1 (July 2014), p. 4495. ISSN: 2041-1723. DOI: 10.1038/ncomms5495.

[149]   Helge Ewers et al. "Label-Free Optical Detection and Tracking of Single Virions Bound to Their Receptors in Supported Membrane Bilayers". In: *Nano Letters* 7.8 (2007). PMID: 17637017, pp. 2263–2266. DOI: 10.1021/nl070766y.

[150]   Joanna Andrecka et al. "Direct Observation and Control of Supported Lipid Bilayer Formation with Interferometric Scattering Microscopy". In: *ACS Nano* 7.12 (2013). PMID: 24251388, pp. 10662–10670. DOI: 10.1021/nn403367c.

[151]   Gabrielle de Wit et al. "Dynamic label-free imaging of lipid nanodomains". In: *Proceedings of the National Academy of Sciences* 112.40 (2015), pp. 12299–12303. ISSN: 0027-8424. DOI: 10.1073/pnas.1508483112.

[152]   Michael W. Davidson Rudi Rottenfusser Erin E. Wilson. *The Point Spread Function*. Zeiss Online Campus. [Online; accessed 27-April-2020].

[153]   Michael W. Davidson Rudi Rottenfusser Sunita Martini. *Numerical Aperture and Image Resolution*. Zeiss Online Campus. [Online; accessed 27-April-2020].

[154]   André AU - Gemeinhardt et al. "Label-Free Imaging of Single Proteins Secreted from Living Cells via iSCAT Microscopy". In: *JoVE* 141 (2018), e58486. ISSN: 1940-087X. DOI: 10.3791/58486.

[155]   *Silicium*. 1997-2020 LUMITOS AG. [Online; accessed 07-August-2020].

[156] Martin A. Green. "Self-consistent optical parameters of intrinsic silicon at 300K including temperature coefficients". In: *Solar Energy Materials and Solar Cells* 92.11 (2008), pp. 1305–1310. ISSN: 0927-0248. DOI: https://doi.org/10.1016/j.solmat.2008.06.009.